Politecnico di Torino

Corso di Laurea Magistrale in Automotive Engineering

Tesi di Laurea Magistrale

Parameterization Of The Exhaust-Fascia Interface Using Surrogate Modelling

Relatore

prof. Renzo Arina

prof. Davide Paolino

Candidate

Tyler Doyle

Ottobre 2018

Author's Declaration of Originality

I hereby certify that I am the sole author of this thesis and that no part of this thesis has been published or submitted for publication.

I certify that, to the best of my knowledge, my thesis does not infringe upon anyone's copyright nor violate any proprietary rights and that any ideas, techniques, quotations, or any other material from the work of other people included in my thesis, published or otherwise, are fully acknowledged in accordance with the standard referencing practices. Furthermore, to the extent that I have included copyrighted material that surpasses the bounds of fair dealing within the meaning of the Canada Copyright Act, I certify that I have obtained a written permission from the copyright owner(s) to include such material(s) in my thesis and have included copies of such copyright clearances to my appendix. I declare that this is a true copy of my thesis, including any final revisions, as approved by my thesis committee and the Graduate Studies office.

Abstract

Currently, full vehicle computational fluid dynamics (CFD) simulations are used to predict rear fascia temperatures. As these simulations are expensive and time consuming, only what is intended to be a worst case scenario analysis is completed. Certain variables can be overlooked and the case selected may not be the worst case scenario. The objective of this thesis is to create a surrogate model that can rapidly predict maximum fascia temperature for a variety of vehicle operating conditions and exhaust positions, while exploring the physical mechanisms responsible for the heat transfer between the exhaust gas, exhaust components, and rear fascia.

Using full vehicle CFD simulations, an investigation of the maximum fascia temperature as a function of vehicle operating conditions and exhaust positioning is completed by identifying non-dimensional parameters governing maximum fascia temperature, consisting of both geometric and non-geometric parameters based on vehicle speed and exhaust inlet velocity (Reynolds number), their ratio (velocity ratio), and exhaust temperature (exhaust temperature ratio). The exhaust positioning within the rear fascia is simplified into four non-dimensional parameters to explore the modifications in geometry.

A design of experiments (DOE) was completed with full vehicle CFD simulations using optimal Latin hypercube sampling of the input variables. Using data from the DOE, a surrogate model is generated. The individual impact of each parameter on the maximum fascia temperature is identified and the surrogate model suggests a vehicle operating condition consisting of low vehicle speed and high load (high exhaust velocity and exhaust gas temperature) results in highest fascia temperatures. For this condition, at a baseline exhaust position, the maximum fascia temperature exceeds the maximum allowable value by 200 K. For the same operating condition, the exhaust positioning predicted by the surrogate model to result in lowest maximum fascia temperature exceeds the maximum allowable value by only 70 K.

Contents

List of Figures

List of Tables

Nomenclature

Symbols

β_+ beta - exhaust rotation

D diameter

d distance

ETR Exhaust temperature ratio

f polynomial function

H vehicle height

J index

$k - \epsilon$ K-epsilon

λ design

L vehicle length

Φ_p optimality criterion

φ basis function

R Reynolds ratio

Re Reynolds number

S covariance matrix

SM surrogate model

T temperature

θ non-dimensional temperature

U velocity

υ kinematic viscosity

W vehicle width

ω weighting function

x sample point

x_c basis function centre

y unknown function of interest

X_+, Y_+, Z_+ Exhaust translation directions

X, Y, Z cartesian coordinates

Subscripts

1, 2 surrogate model 1 and 2

F fascia

FM fascia maximum

i, j, k, m indices

∞ free stream

J jet

s number of distinct distance values in maximin criterion

V vehicle

Superscripts

p positive integer

Abbreviations

CFD Computational Fluid Dynamics

CRF Centro Richerche Fiat

C-SUV Compact Sports Utility Vehicle

CTC Chrysler Technical Center

DOE Design of Experiments

DOM Discrete Ordinate Method

EBF Elliptical Basis Function

FCA Fiat Chrysler Automobiles

HPC High Performance Computing

LHS Latin Hypercube Sampling

NVH Noise Vibration Harshness

OLHS Optimal Latin Hypercube Sampling

RANS Reynolds-Averaged Navier-Stokes

RBF Radial Basis Function

RTE Radiative Transfer Equation

S2S Surface to Surface

SST Shear Stress Transport

WOT Wide Open Throttle

Chapter 1

Introduction

Automakers have, since the early 2000's, begun packaging the exhaust components within the rear bumper, also known as the rear fascia. These packing configurations, primarily motivated by aesthetics, also place the exhaust system closer to the under-body, reducing interaction with the under-body flow. Since it is not a structural component, the rear fascia is typically a plastic part to reduce weight. There are multiple packaging techniques used throughout the industry, but regardless of the technique, the hot exhaust components and exhaust gas are in close vicinity to the plastic fascia. An example of traditional and modern exhaust packaging is illustrated in Figure 1-1.

The fascia can be close enough to the exhaust to be adversely affected by the high temperatures of the exhaust components and exhaust jets. It must be ensured that the plastic fascia is not subject to damage under all vehicle operating conditions. So, it is important that the maximum fascia temperature under all conditions can be predicted at the design stage. Fascia temperatures can be predicted using full vehicle computational fluid dynamics (CFD) simulations. In a fast paced design environment, automakers are only able to simulate a small number of operating conditions to try to capture the maximum fascia temperature. Since there are many variables that govern

the heat transfer between the exhaust and fascia, the case that yields the highest fascia temperatures may be overlooked by such a selective approach, resulting in a maximum fascia temperature that is in excess of the maximum allowable value.

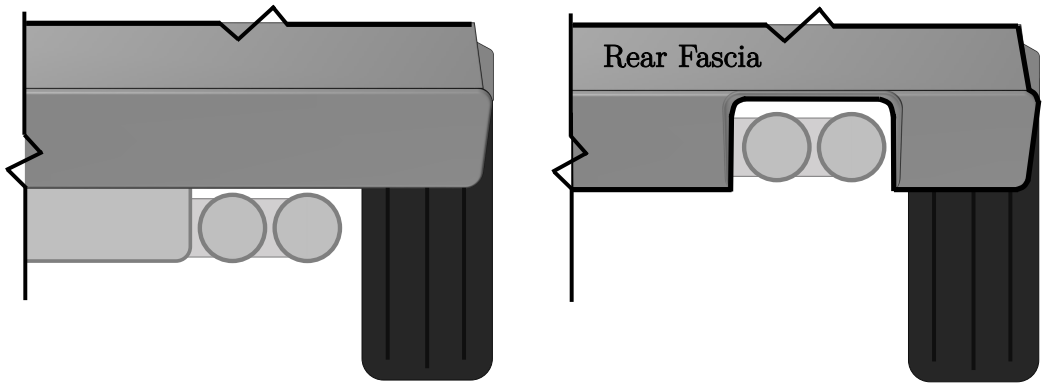

Figure 1-1: Comparison of traditional and modern exhaust packaging. Left: traditional; right: modern.

While the simulations' accuracy is not always known, even measuring these temperatures experimentally is non-trivial. Typically measurements are completed with thermocouples; however, peak temperatures can be missed due to improper placement, as thermocouples essentially provide a point measurement. Effective use of both CFD and experiments together is important as, computations can more easily reveal trends and the expected locations of the maximum fascia temperature, while experimental tests yield reliable temperature values at the operating condition and location that is identified as the worst case.

When an output of interest cannot be easily measured, or it is time consuming to do so, predictive models, also known as surrogate models are constructed. Surrogate models are generated from a set of well-designed experiments and are capable of predicting the output. When experiments take days to complete, having a model that can predict the output (in this case the maximum fascia temperature) enables both time and money to be saved. Industry timelines don't allow for complete experimental and CFD analyses to be carried out for every vehicle design. So, instead

of running multiple CFD simulations for a specific design, a model generated from CFD simulations for a generic configuration will be able to quickly predict the maximum fascia temperature for any load condition. Using experimental data to validate the model will ensure the predictions are reliable and can be used instead of lengthy design studies.

Thus, an approach that combines CFD, experiments to assess data, and surrogate modelling is likely required to successfully predict maximum fascia temperatures during the design stage. When a design does have unacceptably high temperatures, insight into what governs the maximum fascia temperature can be used to generate a suitable alternative design.

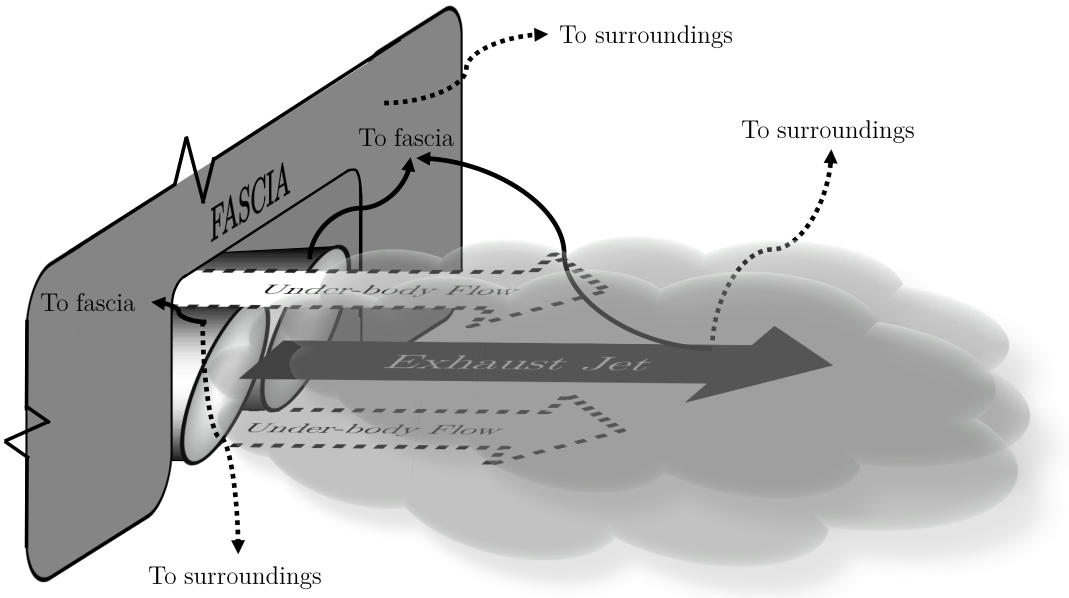

Figure 1-2: Convection and radiation govern the heat transfer to and from the fascia.

There are many variables affecting the maximum temperature of the fascia. These are vehicle speed, exhaust gas velocity, exhaust gas temperature as well as the exhaust part temperatures, along with the fascia and exhaust positioning. There are two mechanisms that govern the heat transfer to and from the fascia: radiation and convection, as schematically illustrated in Figure 1-2. To the fascia, there is radiation

heat transfer from the exhaust tips and convection from the exhaust jets. From the fascia, there is radiation heat transfer to the surroundings and convection to the under-body flow.

1.1 Objectives

The two main objectives of this thesis are to:

1. identify key parameters that characterize the fluid-thermal interaction of the exhaust-fascia system and their various sensitivities and importance, and

2. use design of experiments (DOE) to develop a model that can predict maximum fascia temperatures for a variety of exhaust positions.

1.2 Key Outcomes

The key outcomes of this thesis are:

1. Two heat transfer mechanisms; radiation and convection govern the behavior of the heat transfer between the exhaust parts, exhaust gas, and rear fascia. Changing an operating condition or the positioning of the exhaust within the fascia will change the net amounts of radiative and convective heat transfer to the fascia. This will determine both the location and temperature of the hot-spot on the fascia.

2. The highest maximum fascia temperatures occur at a vehicle speed of zero. Increasing vehicle speed lowers the maximum fascia temperature until a minimum is reached and then it increases again as vehicle speed increases.

3. The final surrogate model indicates an operating condition consisting of maximum exhaust temperature, maximum exhaust velocity, and a minimum vehicle

speed will result in the highest fascia temperatures. This corresponds to wide open throttle (WOT) conditions while driving slowly. This could be during heavy towing conditions at very low speed. With a baseline geometry, the case predicted by the final surrogate model to produce the highest fascia temperature exceeds the maximum allowable value by 200 K.

4. The final surrogate model suggests that keeping the exhaust components as far away from the fascia as possible, decreasing its surface area, while aiming the exhaust downwards from the fascia will result in the lowest fascia temperatures. This decreases the two governing mechanisms: radiation and convection, and thus the total heat transfer to the fascia. In comparison to the baseline geometry, for the load condition resulting in the highest maximum fascia temperature, the optimal geometry is reduces the maximum fascia temperature so that it exceeds the allowable value by only 70 K.

5. The exhaust velocity's influence on maximum fascia temperature is directly related to the vehicle speed and thus the ratio of the vehicle speed to the exhaust velocity. At a value of 0.24, the ratio was found to yield highest maximum fascia temperatures due to the exhaust jets' ability to remain coherent, while being directed towards the fascia by the under-body flow.

These outcomes yield insight useful for design and the influence of vehicle operating conditions on the maximum fascia temperature. A single simulation of the worst load case can be used to find the absolute maximum temperature of the fascia and the impact of the exhaust's position can be used to guide design changes if the initial design yields unacceptably high fascia temperature. Also, a design team changing the position of the exhaust can check if the design poses any thermal risk.

1.3 High Level Outline

The remainder of this thesis is organized as follows: Chapter 2 provides a summary of relevant literature and identifies the gap that is filled by this thesis. Chapter 3 details the approach taken with respect to the CFD simulations and surrogate model construction. Chapter 4 describes the analysis of the physical mechanisms at play and the assessment of the surrogate model. Finally, in Chapter 5, the main findings are summarized and recommendations are made for future work.

Chapter 2

Literature Review

Little research in the open literature can be found related to heat transfer mechanisms governing temperatures for the exhaust jet and the surrounding area. Much of the existing work has focused on noise, vibration, and harshness (NVH) instead.

Research completed by Srinivasan et al. [1] and Eller et al. [2] has been done to ensure that high temperature components do not damage the parts around them. However, this was done for under-hood or under-body components and not the rear fascia area of the vehicle. For thermal protection of under-hood and under-body components, there is no exhaust jet; however, exhaust parts are modelled. Srinivasan et al. applied an isothermal boundary condition to model exhaust components, whereas Xiao et al. [3] applied a constant heat flux to the exhaust components. To best model the exhaust components in this thesis, these methodologies are reviewed in Section 2.1. Research of the heat transfer from high temperature jets to surrounding surfaces, such as that by Spring et al. [4] is used to better understand parameters involved in the heat transfer from the exhaust jet to the rear fascia. Furthermore, modelling techniques from these studies can be used to study the heat transfer between the exhaust and rear fascia, which is the focus of this thesis.

Surrogate modelling is well-described in the literature. This methodology has

been proven to be effective and has been applied to many areas of research such as high speed civil transport, airfoil shape optimization, diffuser shape optimization, and injectors [5].

2.1 Heat Transfer Modelling and CFD Best Practices

CFD simulations should be able to accurately capture the relevant physical mechanisms for both the flow and heat transfer. The main challenge in this is related to correctly predicting the Nusselt number. This is because it depends on the details of the turbulent momentum transport and so it is affected by the choice and accuracy of the turbulence model in Reynolds-averaged Navier-Stokes (RANS) computations.

This is noted by Spring et al. [4] who investigated CFD-based prediction of heat transfer from a jet in a cross-flow. The authors note that the standard $k-\varepsilon$ model is known to overestimate the spreading of a round jet and underestimate the heat transfer rates. The shear stress transport (SST) turbulence model was found to deliver the most accurate results for the heat transfer rates of a single impinging jet. In their study, they prescribed a uniform velocity inlet, as the length of the jet pipe was long enough such that the velocity profile of the jet became fully developed. Their main findings were that at the stagnation point (where the jet impinges on the wall), lower heat transfer rates were found the further the jet outlet was away from the wall. This was due to higher levels of turbulence from the mixing of the cross-flow velocity with the jet velocity. Downstream, it was found that higher cross-flow velocities produced larger heat transfer coefficients due to increased convective transport. This insight can be transferred to the high temperature exhaust jets exiting the exhaust tips. The closer the exhaust jet exit is to the fascia, the higher the heat transfer will be to the fascia. Away from the stagnation point (impingement location of the

exhaust jet on the fascia), increasing the external flow velocity will produce higher heat transfer coefficients and Nusselt numbers. This corresponds to increased vehicle speeds increasing the convective transport of the exhaust jet.

To non-dimensionally analyze a jet and external flow velocity, Spring et al. defined the Reynolds number of both the jet and external flow. They defined the jet Reynolds number with respect to the diameter of the jet inlet. In other research investigating jets in external flows, such as the work done by Jendoubi et al. [6], Michalke et al. [7], and Chan et al. [8], the authors defined a velocity ratio of $\frac{U_\infty}{U_J - U_\infty}$, $\frac{U_J - U_\infty}{U_J + U_\infty}$, and $\frac{U_J}{U_\infty}$, respectively, where U_J and U_∞ are the jet velocity and external flow velocity, respectively. For this thesis, the vehicle Reynolds number (Re_V) is easily defined with respect to the vehicle speed (external flow velocity) and the vehicle length. The exhaust jet Reynolds number (Re_J), as defined by Spring et al., can be calculated with respect to the jet inlet diameter. The velocity ratio, R, can be defined as the ratio between the vehicle and exhaust jet velocity, $R = \frac{U_V}{U_J}$, avoiding division by zero at a vehicle speed of zero.

Srinivasan et al. [1] outline a procedure for vehicle thermal protection development that uses three-dimensional CFD to determine high temperature regions on the vehicle under-body. The procedure used a coupled convection-radiation simulation. It neglected conduction, as the conductivity of the most thermally sensitive components (elastomers, plastics, and rubbers) is poor. They were treated as adiabatic boundaries without significant loss of accuracy. The computation was carried out using the commercial package CFD-ACE+ which is a general purpose unstructured control volume based Navier-Stokes flow solver. Standard $k - \epsilon$ turbulence model in conjunction with wall functions was used for turbulence closure. A surface-to-surface (S2S) based radiation model was used and the emissivity of parts were set. Exhaust skin temperatures were values obtained from a one-dimensional model and specified as isothermal wall boundary conditions on the various sections of the exhaust sys-

tem. Through the use of this methodology, CFD temperatures and experimental test values were compared. For 13 components, it was found that on average, the CFD over predicted temperatures by 4 K with an average error of 8.29%. This could be attributed to the adiabatic boundary condition employed on the thermally sensitive parts. The procedure provided by Srinivasan et al. provides an accurate method to use for the exhaust part boundary conditions (isothermal), as well as the boundary conditions for the fascia (adiabatic).

Xiao et al. [3] also studied the radiation and conjugate heat transfer for the vehicle under-body. The authors completed a steady state analysis considering radiation and conjugate heat transfers. Unlike Srinivasan et al., they incorporated conduction into the analysis. They calculated the component temperature by integrating conjugate heat transfer on internal and external airflow of the exhaust system. Star-CD was used which solves the RANS equation using a finite volume technique. The high-Reynolds number $k - \epsilon$ turbulence model was used. Conduction was solved for both fluid and solid, assuming that the working fluid was incompressible air and the exhaust was stainless steel. Radiation was solved by the discrete ordinate method (DOM) in Star-CD. The exhaust boundary inlet was uniform and given a temperature and flow rate. The surface of the exhaust was given a constant heat flux rather than an isothermal temperature boundary, as exhaust gas was assumed to flow through the pipe. Findings were not compared with experimental results, so the accuracy of the methodology is unclear. This method incorporated the external flow over the exhaust pipe, as well as conduction through the exhaust pipe. The main finding was that the external temperature of the exhaust pipe will be reduced due to the external airflow. Incorporating the flow through the exhaust pipe greatly complicates the simulation as conduction through the exhaust pipe is now modelled. Srinivasan et al. [1] were able to impose isothermal boundary conditions from one-dimensional models which use less computational resources. The isothermal exhaust skin boundary condition in

CFD computations does not consider cooling via the external air as done by Xiao et al. [3]; however, one-dimensional skin temperatures are computed with convection to the external air, decreasing potential error.

Zhang and Romzek [9] outline the use of CFD in vehicle exhaust systems. They noted that the majority mass fraction of exhaust gas is nitrogen, and experimental test results show the exhaust gas can be treated as ideal gas. This was also confirmed by Xiao et al. [3] who also assumed that the gas can be modelled as air and treated as an ideal gas. Zhang and Romzek also note that the fluid flow inside the exhaust pipe is primarily turbulent flow and that the $k-\epsilon$ turbulence model can be used. For exhaust boundary conditions, they found that commonly, inlet boundary conditions are exhaust gas mass flow rate and temperature. Lastly, they noted that emissivity of material is another critical input to accurately simulate skin temperature when a radiation heat transfer model is active. This was also mentioned in the procedure outlined by Srinivasan et al. [1].

Kandylas and Stamatelos [10] investigated exhaust system design based on heat transfer computation. In their work, it is stated that although the exhaust gas flow in a real exhaust system is unsteady and compressible, the variation of pressure in automotive exhaust systems is on the order of 0.01 kPa and thus is of negligible importance. For this narrow pressure range, density was determined to be a function of temperature, and thus the flow of exhaust gas could be assumed to be steady and incompressible. Their model showed good agreement between computational and experimental exhaust gas temperatures.

A textbook by Modest [11], summarizes the radiation properties of molecular gases. Modest notes that when a gas has a temperature exceeding its characteristic vibration temperature, it will participate in radiative heat transfer. As suggested by Xiao et al. [3], Zhang and Romzek [9], and Kandlylas and Stamatelos [10], exhaust gas can be modelled as air. Since the characteristic vibration temperature of diatomic

nitrogen is 3521 K, and exhaust gas temperatures are typically below 1300 K, one would not expect to see any significant radiation heat transfer from the exhaust jets to the rear fascia.

In summary, both the vehicle (Re_V) and jet (Re_J) Reynolds numbers non-dimensionalize the external and jet flow, respectively. A velocity ratio, R, the ratio between vehicle and exhaust inlet velocity, where $R = \frac{U_V}{U_J}$ can be used to non-dimensionally analyze the two flows. The procedure described by Srinivasan et al. provided good agreement between experimental and CFD results while simplifying the heat transfer, removing conduction. Although it did not incorporate an exhaust jet, other studies indicate that it can be modelled as steady, incompressible and turbulent air. Modest indicates that neglecting radiation heat transfer from air is acceptable as the exhaust gas will not reach high enough temperatures to cause any significant radiation heat transfer. This past work sets the stage to complete the problem of determining the maximum fascia temperature due to the heat transfer from exhaust parts and exhaust jets.

2.2 Key Vehicle Thermal Management Case

It was indicated by Eller et al. [2] that slow uphill drive, idle, and maximum velocity operating conditions typically result in the most challenging vehicle thermal conditions. The case that Srinivasan et al. [1] analyzed in their under-body thermal simulations was identified as the case with the highest exhaust skin temperatures. This case was a vehicle travelling at 24.58 m/s (88.5 km/h) while pulling a trailer. The high temperatures were due to the heavy load. These cases give an initial set of operating conditions to analyze that have the potential to yield high fascia temperatures.

2.3 Surrogate Model Construction

The motivation for surrogate modelling is clearly defined in the literature. A surrogate approach saves time and money by decreasing the amount of experiments (whether physical or computational) completed, while allowing for fast analysis and approximations [12]. Similar definitions can be found in [5, 13, 14, 15, 16]. Surrogate modelling methodology can be found in many papers [5, 13, 14, 15] and also in textbooks [12, 16]. The methodology is similar between each piece of literature; however, the procedure outlined by Forrester et al. in Engineering Design via Surrogate Modelling [12], known as the surrogate modelling process was found to be the most clear and concise and is summarized below with additional information from other resources.

1. The design space is identified. The outputs of interest are identified and the inputs that impact the output(s) are analyzed. Here, the ranges of the input parameters can be selected as well.

2. Design of experiments (DOE) is completed. To generate the surrogate model, a sampling method is chosen to distribute the samples uniformly within the design space. A uniform level of model accuracy throughout the design space requires a uniform spread of points. When the number of input variables are small, or the experiments are not time consuming, full factorial sampling can be used [12]. Mckay et al. [13] notes that one of the most popular DOE methods for (relatively) uniform sample distributions is Latin hypercube sampling (LHS).

A full factorial sample uses every combination of inputs at the specified number of levels. As shown in Figure 2-1, 2 inputs with their range divided into 10 levels results in 100 experiments (10^2). The design space is uniformly sampled; however, many experiments are required to do so. With full factorial sampling, the number of inputs has a large impact on the number of experiments required [12]. The addition of a

single input sampled at the same 10 levels results in an increase of 900 experiments.

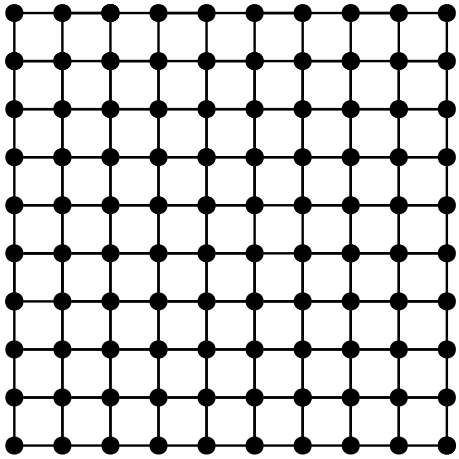

Figure 2-1: A 2 input, 10 level full factorial sample.

The LHS technique allows the designer total freedom in selecting the number of designs (λ) to run (as long as it is greater than the number of inputs), but at least 3λ designs is recommended to initialize a surrogate model [17]. LHS divides the design space into λ equal sized hypercubes known as bins. A point is placed randomly into each bin ensuring that the design space can be exited along any direction parallel to any axis without encountering any of the other occupied bins. In Figure 2-2, a 2 input, ten-point (ten-design) LHS is shown. Each row and column only contain one point, but the points are not distributed evenly throughout the design space.

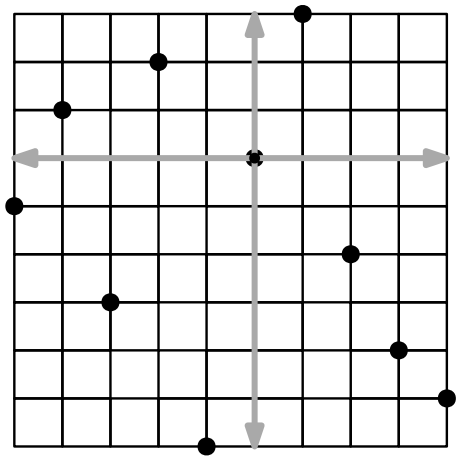

Figure 2-2: Sampling on a 2 input, 10-point LHS. [17]

A drawback to LHS is that it is not reproducible because samples are generated with random combinations [17]. In addition, as the number of points decreases, the chances of missing some regions of the design space increases [17]. To uniformly distribute the points evenly throughout the design space, the optimal Latin hypercube sampling (OLHS) method was developed [17]. The OLHS method gives the best opportunity to model the true function of the response across the range of the inputs [12]. OLHS uses an optimality criterion known as the ϕ_p criterion, based on the "maximin" distance criterion [17], which ensures the points are uniformly spaced throughout the design space while following the LHS methodology.

The following OLHS process is described by [17, 18]. First, a normal LHS is run. The design is a "maximin" distance design, [19] if it maximizes the minimum inter-site distance:

$$min_{1\leq i,\, j\leq \lambda,\, i\neq j} d(x_i, x_j)$$

where $d(x_i, x_j)$ is the distance between two sample points x_i and x_j:

$$d(x_i, x_j) = d_{ij} = \left[\sum_{k=1}^{m} |x_{ik} - x_{jk}|^t\right]^{1/t}, \; t = 1 \; or \; 2$$

Morris and Mitchell [20] built upon the maximin distance criterion. Further described by [17, 18], for a given design, by sorting all the inter-sited distance $d_{ij}(1 \leq i,\, j \leq \lambda,\, i \neq j)$, a distance list ($d_1$, d_2, ..., d_s), and an index list (J_1, $J_2, \ldots,$ J_s) are obtained, where d_i's are distinct distance values with $d_1 < d_2 < \cdots < d_s$, J_i is the number of pairs of sites in the design separated by d_i, and s is the number of distinct distance values. A design is called a ϕ_p-optimal design if it minimizes:

$$\phi_p = \left[\sum_{i=1}^{s} J_i d_i^{-p}\right]^{1/p}$$

where p is a positive integer. For a p that is very large, the ϕ_p criterion is equivalent

to the maximin distance criterion. Figure 2-3 shows a more evenly distributed set of points, which would lead to a better surrogate model.

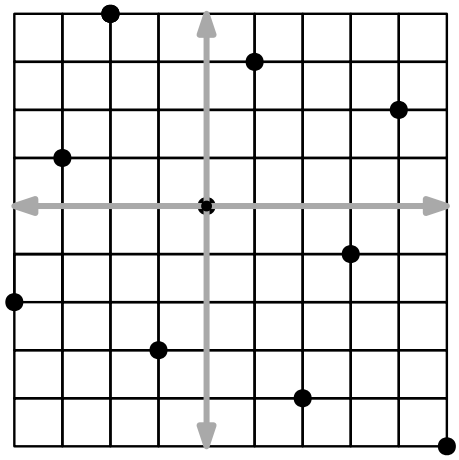

Figure 2-3: Sampling on a 2 input, 10-point OLHS. [17]

Once the DOE portion of the surrogate modelling process is finished, the following steps are completed:

3. the design space is sampled, meaning the experiments are run with the parameter values generated by the chosen sampling technique in the previous step.

4. The predictive model is built using the results from the experiments.

Methods to generate approximation models for non-linear, multi-dimensional landscapes include semi-parametric models (Kriging) and non-parametric models (Basis functions) [5]. Parametric models such as polynomial models are not used for non-linear, multi-dimensional problems as they assume that there is a single global function between the inputs and outputs. This can cause high amounts of error if the problem is highly non-linear.

Kriging models are semi-parametric meaning that they assume that a global function between the output and inputs is known, but incorporates a non-parametric covariance matrix [5]. As described by [17], the Kriging method estimates that an

output is the sum of two components:

$$y(x) = f(x) + S(x)$$

Here $y(x)$ is the unknown function of interest $f(x)$ is a known polynomial function of x called the trend and provides a global model of the design space. It is often taken to be a constant. $S(x)$ is a correlation that depends only on the distance between the locations under consideration and is known as the covariance matrix. While $f(x)$ globally approximates the design space, $S(x)$ creates localized deviations so the Kriging model can interpolate the sampled data points.

Basis function models are non-parametric, meaning that they use different models in different regions of the data to build an overall model [5]. These models known as basis functions φ_j are used to give an output [17]:

$$y(x) = \sum_{j=1}^{M} \varphi_j(x)\omega_j$$

where

$$\varphi_j(x) = \|x - x_c\|_2^2 = (x - x_c)^T(x - x_c)$$

is the Euclidean distance between the prediction site x and the centres x_c of the M basis functions. ω_j are the coefficients of the linear combinations, or weights. Basis functions can consist of Radial Basis Functions (RBF) and Elliptical Basis Functions (EBF). Compared to RBF networks where all inputs are handled equally, EBF networks treat each input separately using individual weights [17]. Instead of the Euclidean distance shown above, EBF networks use a Mahalanobis distance [21], defined as:

$$\|x - x_c\|_m^2 = (x - x_c)^T S^{-1}(x - x_c)$$

where S is known as the covariance matrix:

$$S \approx diag(S_i);\ i = 1, ..., n$$

where S_i are positive numbers and n is the number of input variables. The S_i values are optimized for a minimum sum of the errors for $M - 1$ data points. The S matrix ranks the input variables in the order of influence on the output variable, allowing the EBF model to typically better approximate the function better than the RBF model.

The procedure summarized from Forrester et al. is used to generate the surrogate model to predict the maximum fascia temperatures. Besides the procedure, OLHS methodology will be used to design the DOE to ensure the input parameters are evenly sampled. Surrogate models will be generated using the methods described in this section. Error will be analyzed in Chapter 4 and the approach that results in the least amount of error will be used for the finalized surrogate model.

Chapter 3

Approach

This chapter details the approach taken to computationally predict the maximum fascia temperature and generate the surrogate model. A flowchart outlining the approach is shown in Figure 3-1. To tackle the problem, it is split into three parts:

1. Carry out the CFD simulations and investigate the physics driving the heat transfer to the fascia.

2. Define and sample the design space.

3. Generate the surrogate model and assess its accuracy.

3.1 Non-Dimensional Parameters

The non-dimensional parameters presented in this subsection allow for straightforward analysis of the maximum fascia temperatures and the parameters influencing it.

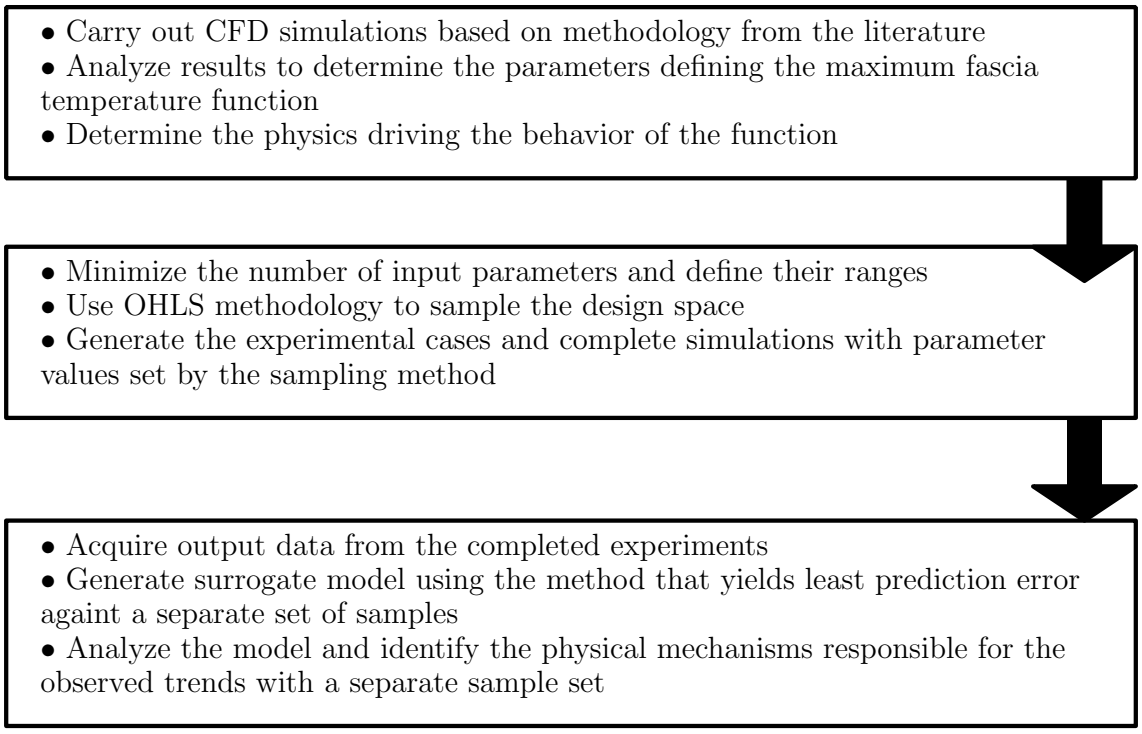

Figure 3-1: Flowchart of approach taken to complete the research.

θ is a non-dimensional temperature. It is described by the difference in highest temperature in the system, $T_{Exhaust\,Gas}$ and the lowest temperature in the system, $T_{Ambient}$. Their difference is the largest temperature difference in the system $\Delta T_{maximum}$.

$$\theta = \frac{T - T_{Ambient}}{T_{Exhaust\,Gas} - T_{Ambient}} = \frac{T - T_{Ambient}}{\Delta T_{maximum}}$$

θ_F and θ_{FM} are non-dimensional representations of the local fascia temperature and maximum fascia temperature, respectively:

$$\theta_F = \frac{T_{Fascia} - T_{Ambient}}{\Delta T_{maximum}}$$

and

$$\theta_{FM} = \frac{max(T_{Fascia}) - T_{Ambient}}{\Delta T_{maximum}} = max(\theta_F)$$

At a θ_F value of zero, the fascia temperature is the same as the ambient air. At one, the fascia temperature is the same temperature as the exhaust gas. θ_F would be invariant for a given set of exhaust gas temperatures if convection were the only heat transfer mechanism at play; the values of θ_F would not be a function of the actual system temperatures, but only their differences. However, since radiation heat transfer is modelled, this invariance breaks down as radiation heat transfer does not scale with temperature differences, but with differences in temperature to the fourth power. Thus, for a single load case, where the exhaust gas temperature and exhaust gas velocity is constant (and thus exhaust component temperatures are constant), θ_F is best to compare results, as the radiation-driving temperature difference to the fourth power will remain constant. In cases where radiation is less important and the heat transfer to the fascia is predominantly via convection, the θ_F behavior approaches the theoretical invariance of pure convective heat transfer.

When comparing non-dimensional temperatures for a set of cases where the temperature of the exhaust gas is not the same, (different load cases), using θ is not ideal, as the denominators of the respective θ's ($T_{Exhaust\,Gas} - T_{Ambient}$) are not equivalent. For a straightforward comparison, θ is calculated with respect to a single exhaust gas temperature, so that the denominator is the same for both calculations. Therefore, when comparing cases with different exhaust gas temperatures, the denominator is calculated with respect to the case with the highest exhaust gas temperature, so that the denominator is constant for all cases being analyzed. This is indicated by $\theta*$:

$$\theta* = (\theta)\left[\frac{\Delta T_{maximum}}{max(\Delta T_{maximum})}\right] = \frac{T - T_{Ambient}}{max(\Delta T_{maximum})}$$

θ_F* and $\theta_{FM}*$ follow the same methodology, the denominator is also calculated with the highest exhaust gas temperature from the cases under examination:

$$\theta_{F*} = \frac{T_{Fascia} - T_{Ambient}}{max(\Delta T_{maximum})}$$

and

$$\theta_{FM*} = \frac{max(T_{Fascia}) - T_{Ambient}}{max(\Delta T_{maximum})} = max(\theta_F)$$

The temperatures of the exhaust components can also be non-dimensionalized, where $\theta_{Exhaust\,Tip}$ and $\theta_{Tailpipe}$ are the non-dimensional exhaust tip and tailpipe temperature, respectively:

$$\theta_{Exhaust\,Tip} = \frac{T_{Exhaust\,Tip} - T_{Ambient}}{T_{Exhaust\,Gas} - T_{Ambient}}$$

and

$$\theta_{Tailpipe} = \frac{T_{Tailpipe} - T_{Ambient}}{T_{Exhaust\,Gas} - T_{Ambient}}$$

As discussed in Chapter 2, velocity ratios are used as non-dimensional parameters to analyze jets in an external flow. Re_V and Re_J are used to define the Reynolds number for the vehicle and exhaust jet, respectively, where:

$$Re_V = \frac{U_V L}{v}$$

$$Re_J = \frac{U_J D}{v}$$

U_V is vehicle speed, U_J is the inlet velocity of the exhaust gas, L is the characteristic length of the vehicle, D is the diameter of the exhaust inlet, and v is the kinematic viscosity of air, which is the same for both flows. The use of constant kinematic viscosity is discussed in Section 3.2.

A velocity ratio, R, defines the ratio of the vehicle speed to the exhaust gas

velocity:

$$R = \frac{U_V}{U_J}$$

This parameter allows for the analysis of the ability of the exhaust jets to remain coherent with respect to the under-body flow. A coherent and non-coherent jet is illustrated in Figure 3-2. A coherent exhaust jet is strong, will not be very spread out, and typically jets well away from the fascia. A non-coherent exhaust jet is weak and will spread into the surrounding area.

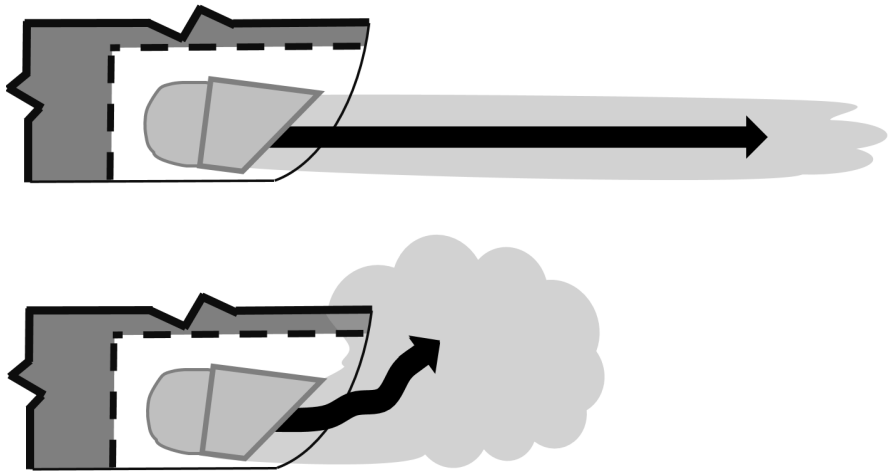

Figure 3-2: Top: coherent exhaust jet; bottom: non-coherent exhaust jet.

As will be shown, for R values larger than 0.24, the exhaust jets are weak in comparison to the under-body flow and likely to be dispersed. R values near 0.24 result in exhaust jets that will remain coherent but will have their direction changed towards the fascia by the under-body flow. For R values below 0.24, the exhaust jets will remain coherent and will jet freely into the domain without any change in direction from the under-body flow.

The exhaust temperature ratio, ETR, is used to analyze the exhaust gas temperature (the highest temperature in the system). It is non-dimensionalized with respect

to the lowest temperature in the system, the ambient temperature:

$$ETR = \frac{T_{Exhaust\,Gas}}{T_{Ambient}}$$

Throughout the thesis, ETR^4 is used to consider the importance of radiation. At one, the exhaust gas is the same temperature as ambient and as it increases, so does the exhaust gas temperature.

3.2 CFD Simulations

A single vehicle is used for all CFD simulations. Shown in Figure 3-3, the vehicle is a compact sports utility vehicle (C-SUV) from Fiat Chrysler Automobile's (FCA) fleet that has a dual tip exhaust recessed into the fascia.

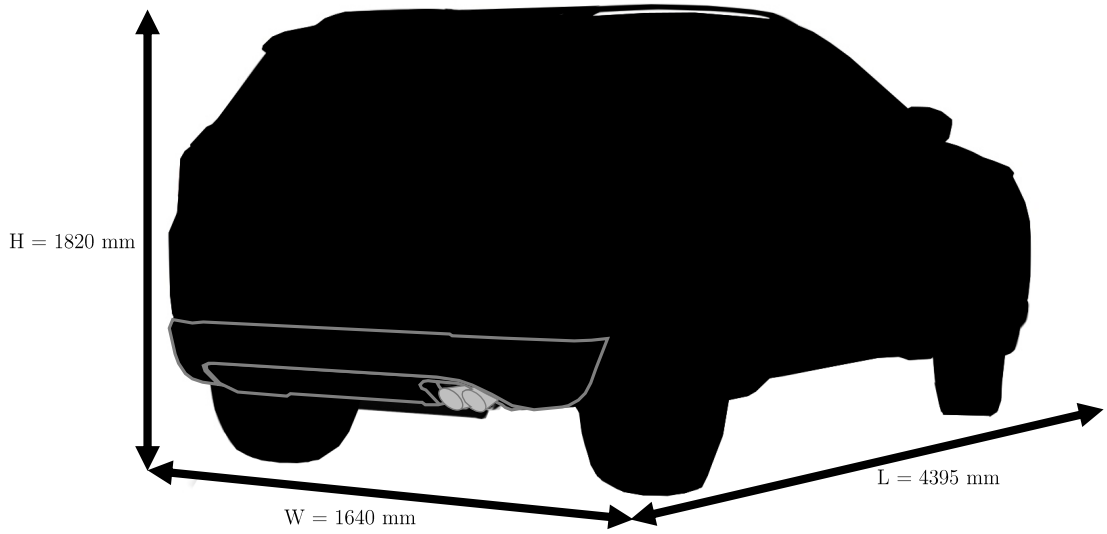

Figure 3-3: C-SUV used for all CFD simulations.

The commercial software ESI CFD-ACE+ Suite is used by FCA's vehicle thermal management department for complete thermal protection analysis. The collaboration of this project with FCA allowed for the use of this software in combination with their high performance computing (HPC) cluster. This greatly reduced computational time

and allowed for detailed full vehicle CFD simulations to be completed. The ACE+ Suite has its own 3D viscous, unstructured adaptive Cartesian mesh grid generation system for use with the CFD-ACE+ solver. It also has its own post-processor, CFD-View. The CFD-ACE+ solver is able to solve both turbulent flow and heat transfer CFD problems. It uses a finite-volume, pressure-based unstructured flow solver, with a collocated, cell centered approach [22].

All simulations were steady state (as the maximum fascia temperature needed to be calculated in steady state) and incompressible, as Mach numbers remained below 0.19 for all cases. The standard $k - \varepsilon$ turbulence model was used based on guidance from the literature. An S2S model is most appropriate for enclosed radiative transfer with non-participating media [23], and as air is not a participating media, an S2S model can be used. The discrete ordinate method (DOM), which solves the radiative transfer equation (RTE) for a number of discrete solid angles, allows for participating media, scattering, and emissivity, and is best suited for cases with localized heat sources. Most other models, such as the P-1 model will over-predict radiative fluxes [23]. Thus, due to localized heat sources, the DOM radiation model is used.

The CFD domain, shown in Figure 3-4, models the dynamometer test cells at the Chrysler Technical Center (CTC). The dimensions and the placement of the vehicle match the experimental configurations used. This allows for the resultant CFD fascia temperatures to be compared with thermocouple data acquired in the test cell.

The walls of the test cell are dark, always stationary, and smooth. The walls of the CFD domain have an emissivity value of 0.9, are adiabatic, all stationary, and no slip, with a roughness height of 0 m. Slip conditions would remove the boundary layer of the flow and change the under-body flow. A change in under-body flow would greatly affect the wake behind the vehicle and thus the heat transfer to the rear fascia.

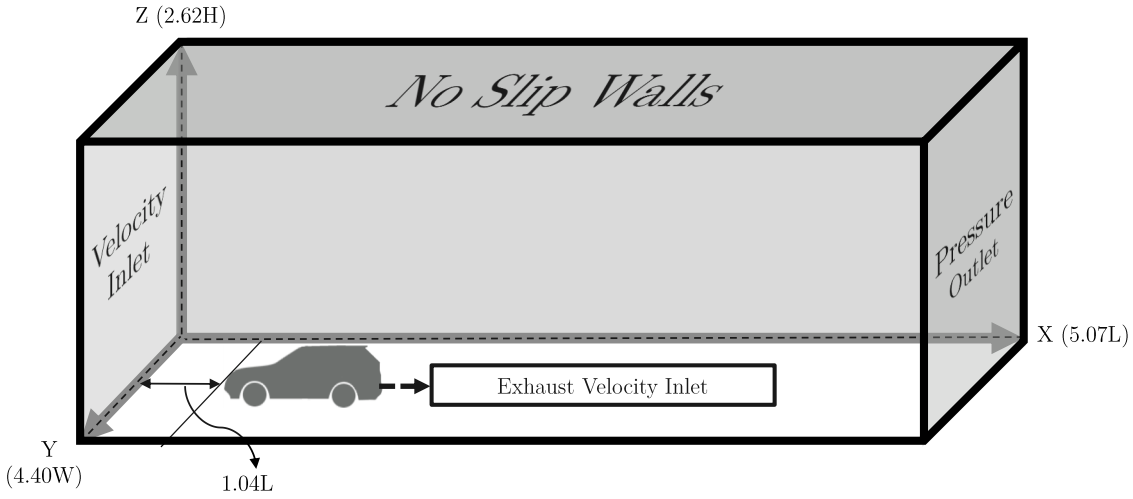

Figure 3-4: CFD domain matches experimental configuration.

The front of the computational domain is a uniform velocity inlet with air as the working fluid. It is 1.04L (car lengths) away from the front of the vehicle to reduce the upstream influence the vehicle has on the flow. The pressure outlet is 3.03L away from the rear of the vehicle.

The ground temperature is constant at 339 K, while the ambient temperature is 311 K. Both of these values are used in the simulation of the Davis Dam load case, a drive-cycle used by automakers to simulate extreme vehicle thermal conditions. The high ground temperature simulates the temperature of asphalt on a hot day, which would be much higher than the air temperature due to its absorption of solar radiation.

Two heat transfer mechanisms are shown in the heat transfer resistance diagram of the fascia in Figure 3-5. The heat transfer from the sources to other sinks are not shown in the diagram. Changing the ambient temperature affects the maximum fascia temperature linearly in the same direction as the ambient temperature change, as the only heat transfer between the fascia and the ambient air is convection. Changing ground temperature affects the maximum fascia temperature in a non-linear manner in the same direction as the ground temperature change due to the non-linear behavior

of radiation.

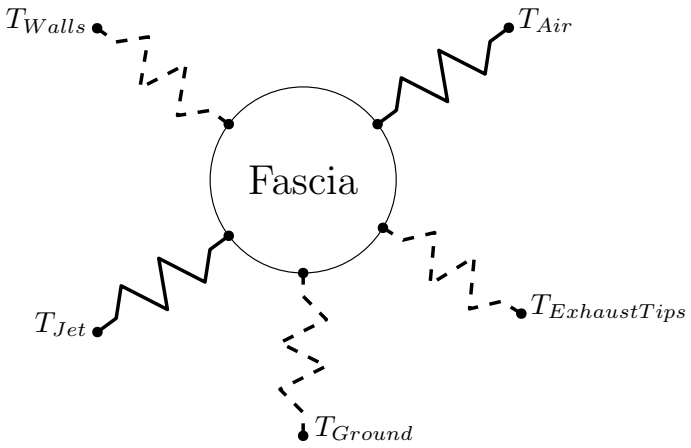

Figure 3-5: Heat transfer resistance diagram, to and from the fascia. Dashed: radiative; solid: convective.

For a sample simulation, compared with an adiabatic fascia boundary condition, conduction was found to decrease θ_{FM} by 0.04. This is due to conduction being a diffusive process. Conduction was not modelled in the simulations used to build the surrogate model as it significantly increased computational time. Due to plastic's low thermal conductivity, the resultant increase in θ_{FM} was not large, with a temperature difference of 12 K. An emissivity of 0.9 was applied to the fascia, as painted plastic ranges from 0.85 to 0.94 depending on the finish [24].

The research completed by Srinivasan et al. [1] established that modelling the exhaust parts as isothermal correlated well with experimental data. The isothermal exhaust part temperatures in this thesis were set using values extracted from a one-dimensional model of the exhaust, to be detailed later. An emissivity that corresponds the average between aged and new steel, 0.3, was also applied to the exhaust parts [24].

A uniform velocity inlet located at the exit of the muffler, which is the inlet to the tailpipe, is used as exhaust gas inlet boundary condition. This inlet, with diameter, D, shown in Figure 3-6 is a value of $149D$ away from the domain outlet. At the inlet, temperature and velocity boundary conditions are applied. Found to be acceptable

in the literature, the exhaust gas is modelled as air. The exhaust gas jet does not emit radiation as noted by Modest [11] as the characteristic vibration temperature of air is well above the temperature of the exhaust gas.

Constant properties of air are used, resulting in the same constant density, viscosity, and thermal conductivity for both the external flow and exhaust jets. Due to the large temperature difference between the external flow and exhaust jets, Re_J calculated with respect to the ambient air properties is larger than if it were calculated with properties that varied with temperature. Occurring at the highest exhaust gas temperature used in the thesis, the maximum difference in Re_J is 90% and the Re_J value remains in the turbulent regime. The calculation can be viewed in Appendix B. In the case where the exhaust gas temperature is at its highest temperature, so is the exhaust velocity, and the mechanism responsible for the maximum fascia temperature is radiation, as will be shown later. This is due to the high temperature exhaust components and the high strength exhaust jets being well away from the fascia.

Two CFD simulations, one with varying parameters and one with constant parameters were completed at the operating condition with the highest exhaust gas temperature. The result was a maximum fascia temperature via radiation heat transfer. A small drop in the maximum fascia temperature (0.5%) was found going from constant to varying parameters. At the location in which a high temperature (not the maximum) was due to convective heat transfer from the exhaust jets, there was a larger temperature change, resulting in a 5% decrease in temperature due to the use of variable properties. For all other cases, the change in maximum fascia temperature is expected to be less than this case, as the change in Re_J will always be less due to decreasing difference in densities as the exhaust gas temperature studied will always be less than the one simulated for this case.

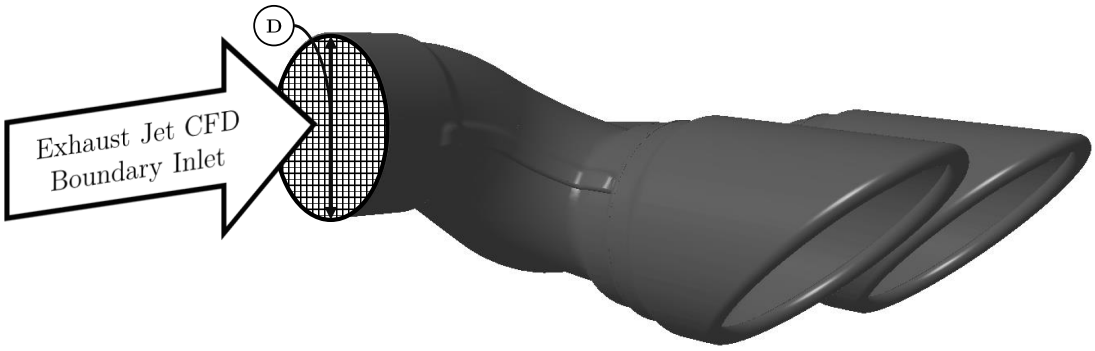

Figure 3-6: Uniform velocity inlet simulates exhaust flow.

An area for potential discrepancy between CFD and experimental tests is the location of the exhaust inlet. The uniform flow inlet at the entrance of the tailpipe assumes that the exhaust velocity is constant at the exit of the muffler. In reality, to perfectly capture the exhaust flow out of the tailpipe, the inlet would need to be at the entrance of the exhaust manifold and flow through the whole exhaust system and muffler. This would involve less economical computational modelling of the flow through the catalytic converter as well as the muffler.

If the flow was assumed to be fully turbulent out of the muffler, a profile boundary condition representative of a fully developed turbulent pipe flow could be applied to the CFD boundary inlet. To simplify the CFD modelling for the DOE cases run, this wasn't done in this way; however, this would better capture the non-uniformity in the flow without having to model the flow through the catalytic converter and muffler.

A one-dimensional model is capable of giving accurate temperatures and exhaust velocities at the end of the muffler, but due to the short duct length, minimal boundary layer development will take place resulting in a more uniform flow than if the whole exhaust system was modelled. There are still non-uniform exit velocities between the two exhaust tips, as shown in Figure 3-7, due to the 90 degree bend in the tailpipe. It is likely that any uniformity is completely removed due to the bend. The outboard tip (top) will always have a larger velocity and thus a larger Re_J value than

the inboard tip (bottom) due to this radical change in direction. The Re_J value of the inner tip will always be lower, leading to easier dispersion of the inboard exhaust jet.

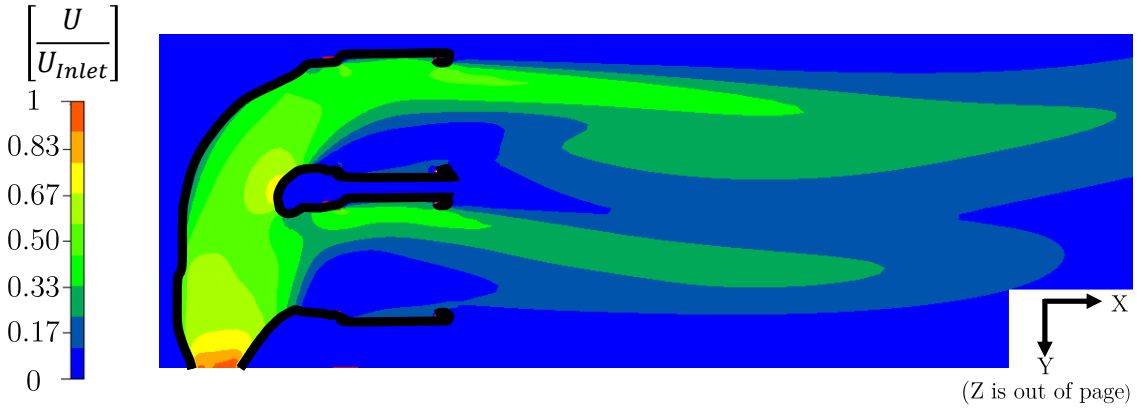

Figure 3-7: Flow separation in center section of the exhaust tailpipe, from CFD data. Viewing XY plane.

Grid independence of the computational results was assured. Simulations were completed increasing the grid refinement level until the change in θ_{FM} was below 0.01. The boundary conditions for the simulations completed are displayed in Table 3.1.

Table 3.1: Case used to assess grid independence.

ETR^4	Re_J	Re_V	R
85.4	1.31×10^5	0	0

Each level in refinement decreased the minimum cell size by a factor of two. Table 3.2 displays that from the default mesh, an increase in one level of refinement, decreased θ_{FM} by 0.01. From the first level of refinement to the second, there was no difference in θ_{FM}, so grid independence was established at the first level of refinement.

With and without a trailer, simulations were completed to identify external conditions that yield the highest fascia temperatures. The trailer, which is placed at a distance $\frac{\Delta x}{L}$ of 0.25 from the rear of the vehicle is shown with its dimensions in Figure

3-8.

Table 3.2: Grid independence refinement results.

Refinement Level	θ_{FM}
Default Mesh	0.29
+ 1 Level Finer	**0.28**
+ 2 Levels Finer	0.28

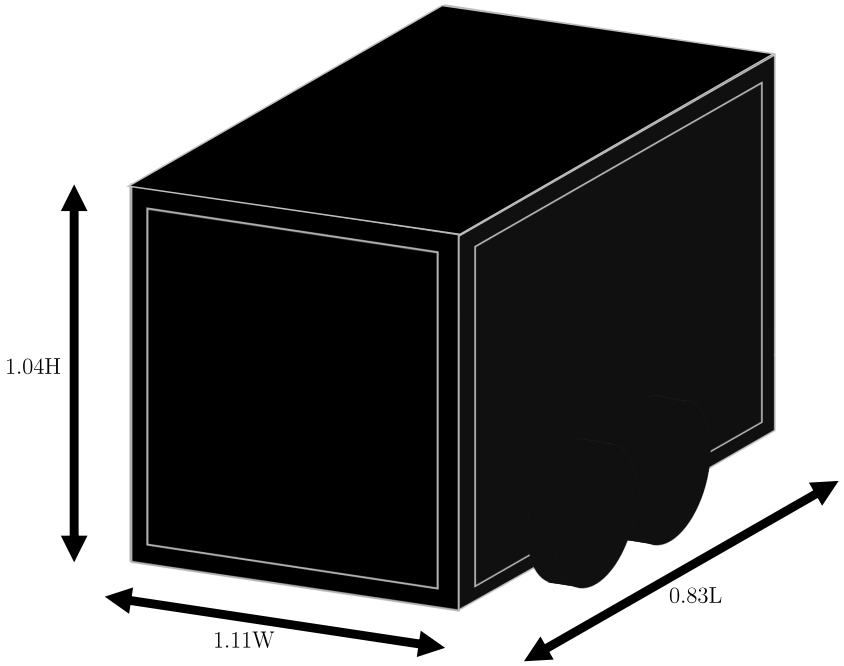

Figure 3-8: Trailer used in CFD simulations and its dimensions.

To accommodate a trailer, the initial domain size is increased, as shown in Figure 3-9. The configuration, modelled as a wind tunnel, allowed for continuity between the large and small domains. The height and width of the domain are doubled, reducing any influence of the flow field around the vehicle and trailer, as the peak velocity around the vehicle remains unchanged for simulations in the two domains.

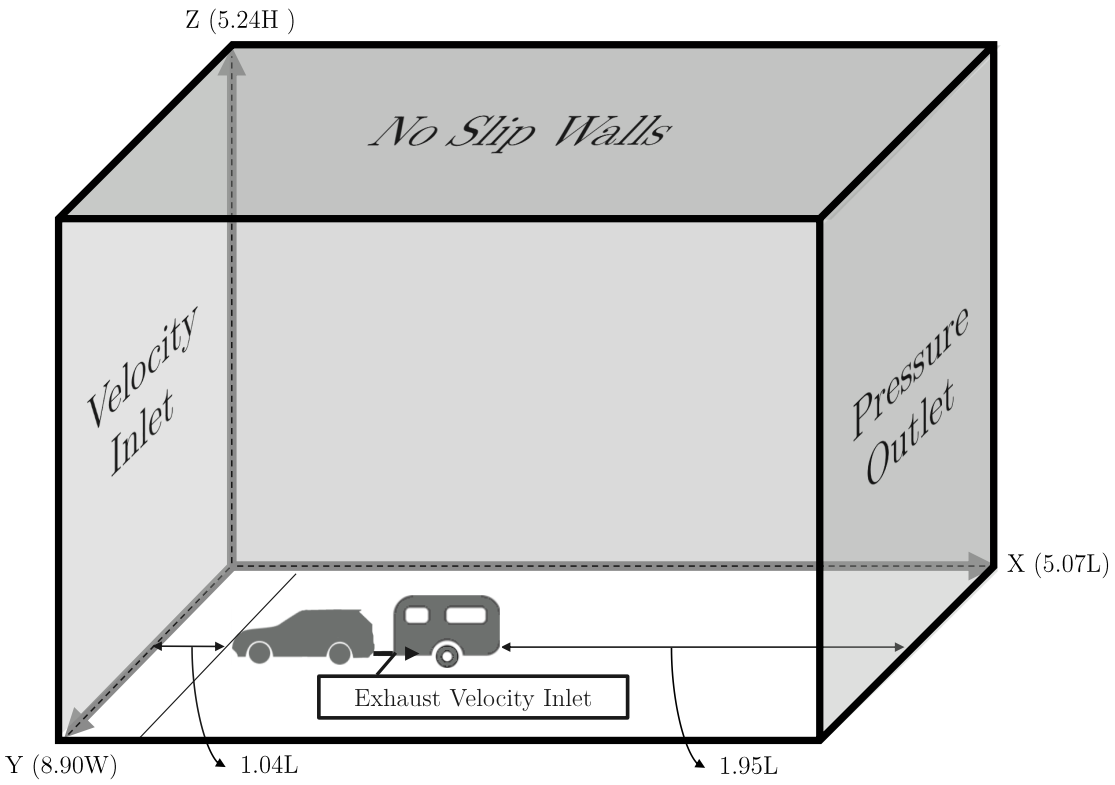

Figure 3-9: Increased domain size accommodates trailer.

To connect the results from the simulations in the large domain, with a trailer, to the small domain, without a trailer, intermediate simulations were completed. The intermediate simulations were completed in the large domain without a trailer. The results of the intermediate simulations were compared with the results of simulations completed in the small domain. With only domain size increasing, the change in θ_{FM} was less than 0.03. As view factors remain unchanged, the increase is due to a small reduction in convective velocity below the vehicle, shown in Figure 3-10.

This chain of dependency between simulations is visually depicted in Figure 3-11. It was also found that the increase in maximum fascia temperature due to the larger domain was always smaller than the increase in maximum fascia temperature due to the addition of a trailer. So, the addition of the trailer in the large domain yielded higher maximum fascia temperatures due to the trailer reflecting radiated heat back to the rear fascia. This configuration was used for the DOE and in generation of the

surrogate model.

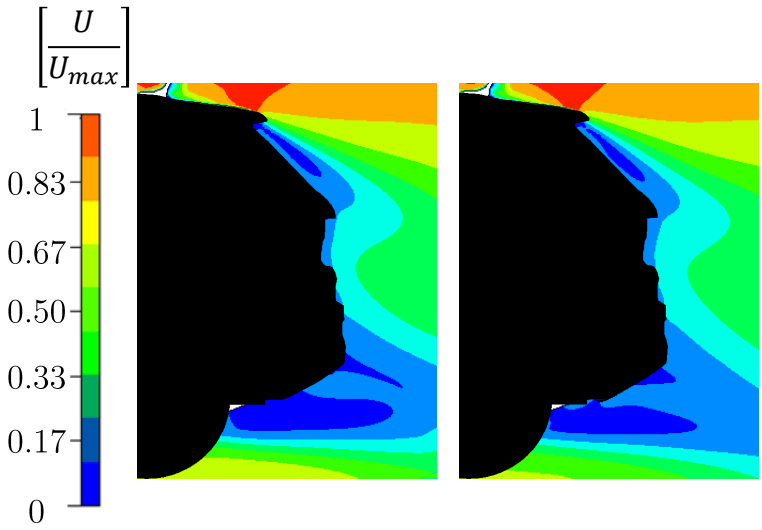

Figure 3-10: Decrease in under-body convective velocity in large domain. Velocity contours cut at centre of vehicle. Left: small domain; right: large domain.

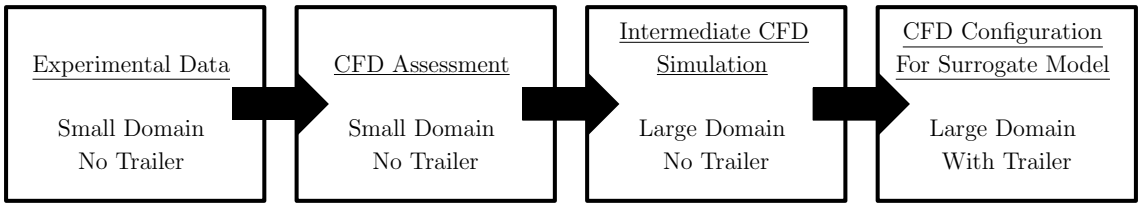

Figure 3-11: Chain of dependency between experimental data and configuration used for surrogate model.

Experimental data only exists for the configuration in the small domain, without a trailer. As a result, assessment of the CFD simulations was completed in the small domain, without a trailer. Thus, the CFD simulations were grounded with the experimental data; however, in Chapter 5, recommendations are made to further map these configurations together.

In summary, the simulation configuration used throughout the surrogate model construction consisted of the vehicle towing a trailer in the larger domain. The CFD simulations modelled radiation and convection but not conduction, as the adiabatic fascia boundary condition was more economical, while resulting in only minimal in-

creases in θ_{FM}. Exhaust parts were set as isothermal boundaries, with the exhaust gas temperature and velocity being set as a uniform flow inlet at the exit of the muffler. The working fluid was air with constant properties, which did not contribute to radiation heat transfer.

3.3 Parameter Development

Geometric and non-geometric parameters affect the maximum fascia temperature. They are described and their ranges for the DOE are defined in this section.

3.3.1 Geometric Parameter Development

The placement of the exhaust within the rear fascia is defined by four non-dimensional parameters. Three correspond to X, Y, and Z translation – parameters X_+, Y_+, and Z_+ respectively. Increasing X_+, Y_+, and Z_+ corresponds to moving in the negative X, negative Y, and negative Z direction, respectively. The last parameter, the pitch of the exhaust tailpipe (rotation with respect to the XY plane) is defined by β_+. These are depicted graphically in Figure 3-12.

The initial geometry provided by FCA defined the baseline position of the exhaust. The values of the parameters are given in Table 3.3. Their ranges, also known as the design space, were defined with the cooperation of FCA and their exhaust design procedures.

Any change in X_+ value translates the exhaust tips in the positive or negative X direction. This corresponds to the rear and front of the vehicle. The tailpipe length is adjusted to accommodate the position of the exhaust tips. The minimum X_+ value extends the exhaust as far as possible towards the rear of the vehicle, without passing the rear bumper of the vehicle. The maximum value positions the exhaust tips into the fascia as far as possible, without interfering with other under-body components.

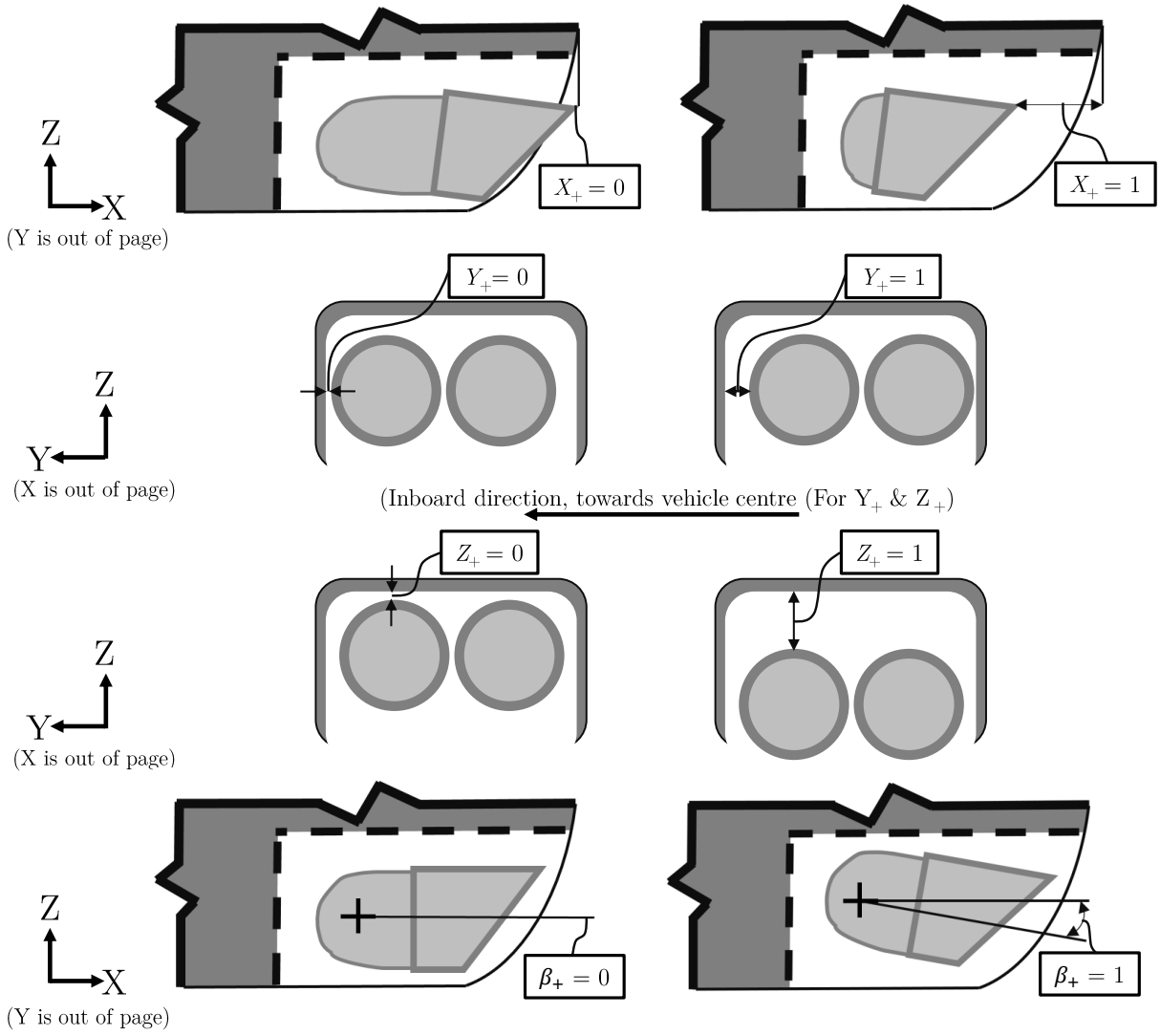

Figure 3-12: Geometric parameters (driver's side view for X_+ and β_+ and rear view for Y_+ and Z_+).

Table 3.3: Baseline (normalized) geometric values.

X_+	Y_+	Z_+	β_+
0.90	0.50	0.50	0.21

Modifying the Y_+ value translates the exhaust tips in the negative or positive Y direction, corresponding to outwards and inwards (towards the center) of the vehicle,

respectively. Complying with the movement of the exhaust tips, the tailpipe length upstream of the 90 degree bend is adjusted so that it always connects the muffler to the 90 degree bend. The minimum and maximum Y_+ values produce no contact between the outer edges of the fascia and the exhaust tips.

The Z_+ position dictates the translation of the exhaust tips in the positive or negative Z direction, corresponding to the top and bottom (towards the ground) of the vehicle. The minimum Z_+ value ensures no contact with the fascia, while the maximum meets ground clearance guidelines. A change in β_+ value rotates the tips and tailpipe with respect to the center of the tailpipe inlet to the muffler.

The minimum β_+ value corresponds to the exhaust tips parallel with the road. Any position above parallel directs the exhaust jets into the fascia, increasing heat transfer to the fascia, so positions above parallel were not investigated. The maximum β_+ value meets styling guidelines in the FCA exhaust department. Due to the coupling between β_+, X_+, and Z_+, during geometry modification, the exhaust tips and tailpipe were first rotated to the correct β_+ value. The height of the exhaust was then adjusted to the specified Z_+ value and lastly, the length of the tailpipe was adjusted such that the specified X_+ value was met. This process is visually depicted in Figure 3-13.

3.3.2 Non-Geometric Parameter Development

An analysis of an initial set of CFD simulations using the baseline exhaust geometry provided by FCA identified non-geometric parameters. Two drive-cycles provided by FCA set boundary conditions for the set of simulations. The boundary conditions, consisting of Re_V, Re_J, ETR, $\theta_{Exhaust\,Tip}$, and $\theta_{Tailpipe}$ made up an initial set of non-geometric parameters to investigate. The boundary conditions of the two drive-cycles are shown in Table 3.4.

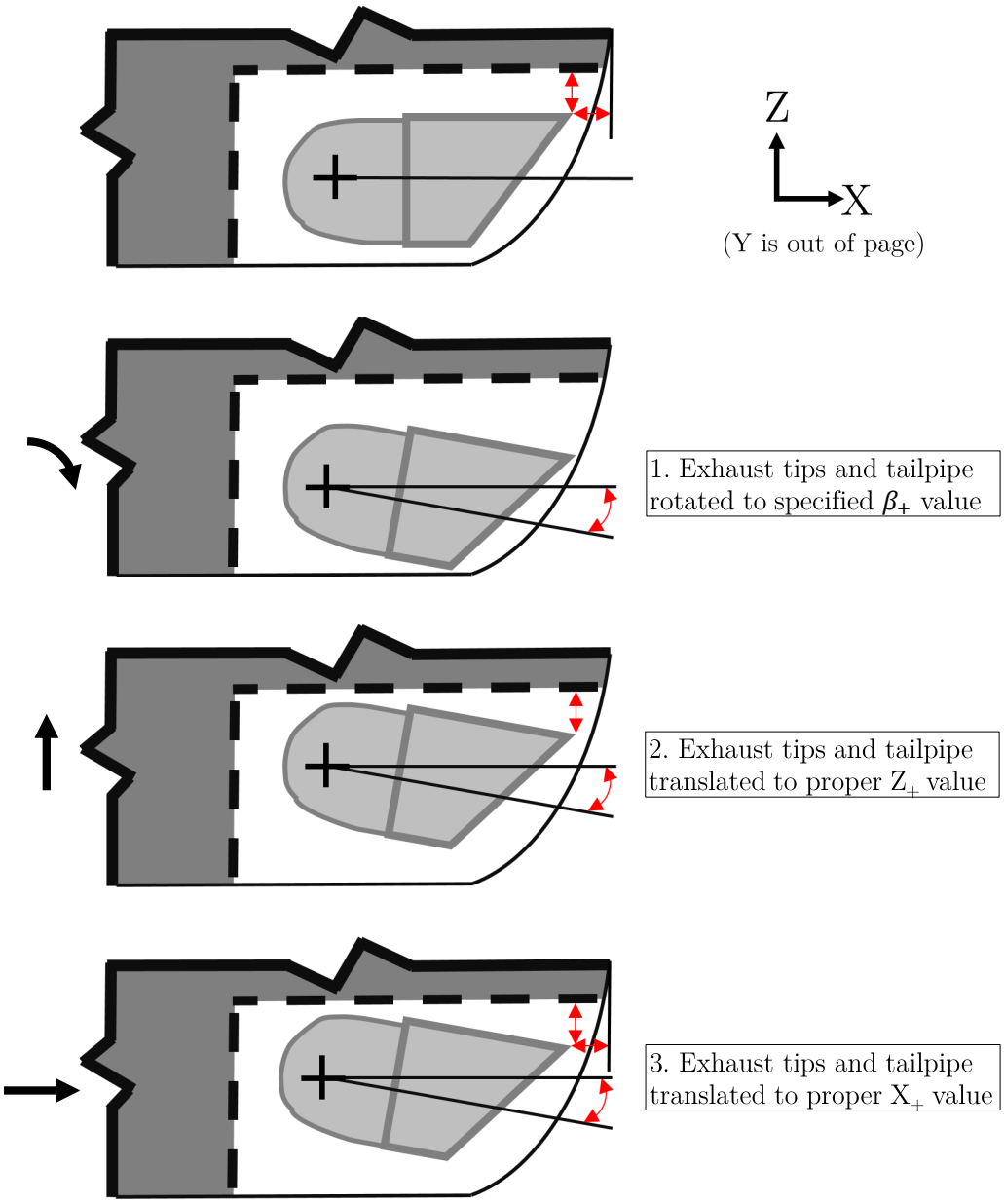

Figure 3-13: Modifying β_+ while maintaining X_+ and Z_+.

As shown in the Table, ETR^4 differs between the two cases. ETR^4 and Re_J directly define the values of $\theta_{Exhaust\,Tip}$ and $\theta_{Tailpipe}$. The two sets (two drive-cycles) of Re_J, ETR^4, and $\theta_{Exhaust\,Tip}$ remained constant while varying only Re_V. These initial simulations determined the impact the boundary conditions have on θ_{FM} and provided the parameters for use in the DOE.

Table 3.4: Cases analyzed to determine non-geometric parameters.

Drive-Cycle	ETR^4	$\theta_{Exhaust\,Tip}$	$\theta_{Tailpipe}$	Re_J	Re_V	R
1	30.9	0.65	0.88	1.31×10^5	0	0
					2.61×10^6	0.27
					8.53×10^6	0.86
2	65.1	0.76	0.91	3.82×10^5	0	0
					2.61×10^6	0.09
					8.53×10^6	0.29

In Figure 3-14, where $\theta_{FM}*$ is calculated with respect to the highest exhaust gas temperature out of the two drive-cycles (drive-cycle 2), it is shown that there is a change in $\theta_{FM}*$ due to the change in Re_V, for different values of Re_J and ETR^4. Also, the change in $\theta_{FM}*$ is not constant as Re_V increased, showing $\theta_{FM}*$'s dependence on all three parameters. Thus, the three variables (Re_V, Re_J, and ETR) were taken to be inputs into the DOE. Due to $\theta_{Exhaust\,Tip}$ and $\theta_{Tailpipe}$'s deterministic relationship with ETR and Re_J, they were not considered as independent inputs into the DOE.

ETR determines the temperature difference between the fascia and exhaust jets as well as the exhaust components. Re_V governs the wake produced behind the vehicle and the amount of forced convection caused by the interaction of the under-body flow with the rear fascia. Re_J governs the distance the exhaust jets remain coherent. The velocity ratio, R, is used in conjunction with the Reynolds numbers to analyze the coupling between the two flows. At $R = 0$, Re_V is zero. Due to the decrease of convective under-body flow, the highest $\theta_{FM}*$ values are observed in Figure 3-14 at an Re_V value of zero. The relationships of the three non-geometric parameters used as inputs into the DOE (Re_V, Re_J, and ETR) and their impact on θ_{FM} are determined from the surrogate model and further explored in Chapter 4.

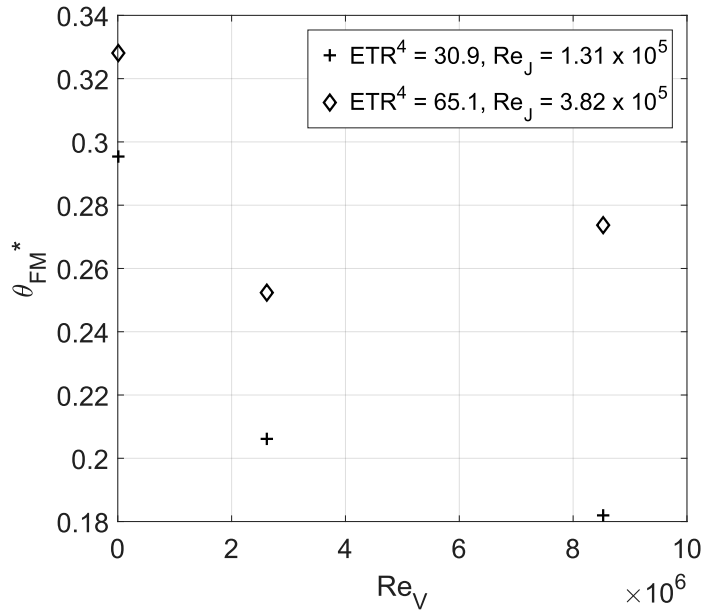

Figure 3-14: $\theta_{FM}*$ values of cases simulated with CFD to determine non-geometric parameters.

3.3.2.1 Non-Geometric Parameter Design Space

A specific load case is defined as the power required by the engine. This corresponds to a combination of exhaust gas temperature and exhaust gas velocity. A vehicle under high load will have a high exhaust gas temperature and a high exhaust gas velocity, as the engine is producing high power with a high engine speed. This corresponds to combustion occurring more frequently. Heat will be released at a faster rate and flow through the exhaust system at a higher velocity. The vehicle speed may vary depending on the load case and together, these variables set a specific operating condition. Examples include the cases explored in Chapter 2: slow uphill climb while pulling a heavy trailer or at the vehicle's maximum velocity. A vehicle under low load will have a low exhaust gas temperature and low exhaust gas velocity. Again, the vehicle speed may vary. Examples include: gliding down a hill at high speed or sitting at idle.

An engine map sets the ranges of the exhaust gas temperature and exhaust gas velocity and thus ETR and Re_J. One-dimensional simulation and dynamometer data acquired from the smallest and largest engines that would be found in a typical FCA C-SUV generated the map used in this thesis. Data at the lowest and highest engine speeds produced the lower and upper bounds of the map. Exhaust gas temperature and exhaust flow rate data were collected while keeping the engine speed at a constant value and increasing the power output of the engine. To capture all load cases, the two engine maps were joined together so that exhaust temperature and velocity range would cover the absolute minimums and maximums for both engines. The exhaust temperatures and flow rates were captured at the catalytic converter. These values were non-dimensionalized and the resulting engine map is shown in Figure 3-15. Clearly defined are the upper and lower bounds of the plot. The shaded area provides the range ETR^4 and Re_J at the catalytic converter. Intermediate engine speeds were not provided, thus the maximum Re_J values at the highest engine speeds for the two engines are connected to close the bounds of the engine map.

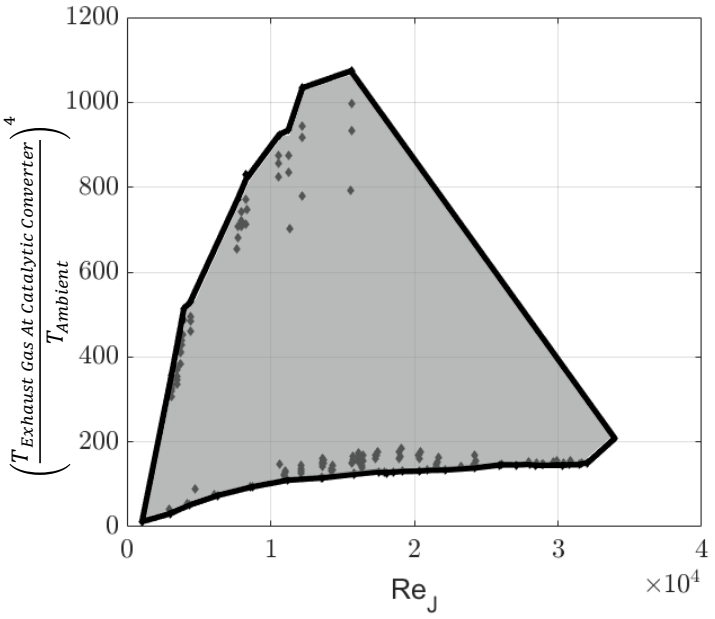

Figure 3-15: Engine map of exhaust conditions at the catalytic converter.

As detailed in Section 3.2, the CFD simulations' boundary condition for the exhaust gas temperature and velocity is defined at the exit of the muffler. The data from the engine map measured these values at the catalytic converter. *ETR* and exhaust velocity (Re_J) was acquired at the end of the muffler using a GT-Power [25] model of the exhaust system. Beginning with an exhaust system template within GT-Power, the catalytic converter, resonator, muffler, the piping throughout, as well as the tailpipe, and exhaust tips are input using measurements of the exhaust system from the vehicle studied. The material of the exhaust piping is steel, which sets the roughness of the internal piping. Ambient temperature remained the same as that in the CFD simulations, 311 K. The model used air as the working fluid. Although external flow around the exhaust is neglected, convection from the exhaust parts to the still ambient air was not. The thermal solver is steady state and simulations are automatically shut-off when steady state is reached. Figure 3-16 illustrates the location of the inputs into the model and CFD boundary location in the model.

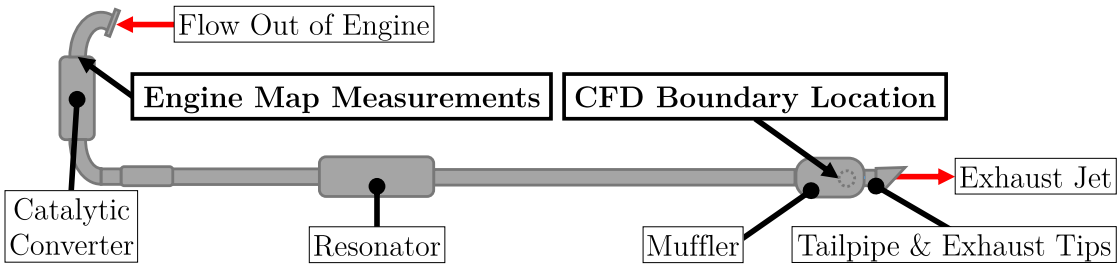

Figure 3-16: GT-Power model sets CFD boundary conditions.

The GT-Power model also provides exhaust skin temperatures for input as boundary conditions into the CFD simulation. In comparison with actual test cell data, the values of the skin and exhaust gas temperatures are hotter on average by 7%, likely due to the model reaching steady state, unlike the test data. This error was found to be allowable as vehicle conditions will vary and this captures the worst case scenario.

The final engine map at the CFD boundary location is shown in Figure 3-17. The ranges for ETR^4 and Re_J are in the shaded area.

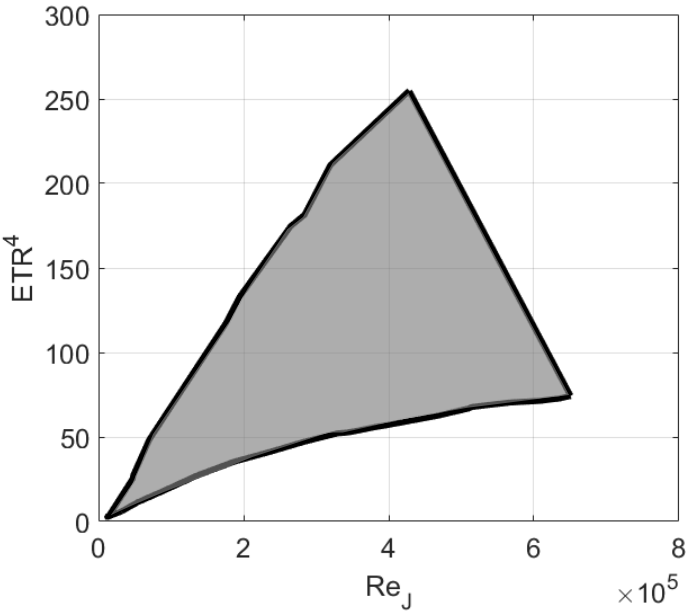

Figure 3-17: Exhaust conditions at CFD exhaust jet inlet, extracted from GT-Power.

The range of Re_V is independently set as it is not dependent on engine load. The range is set from 0 to 1.09×10^7. This range covers typical drive-cycle speeds a vehicle will endure. At its minimum, the vehicle is stationary and at its maximum, the vehicle is at highway speed.

3.4 Design of Experiments

Surrogate models are always most accurate in the vicinity of points that have been sampled. A uniform spread of points will give the model a uniform level of accuracy throughout the design space. As discussed in Chapter 2, the OLHS method is best because it optimizes the spread of the points throughout the design space, creating a more uniform distribution thus a more uniform level of accuracy of the surrogate model. The software used to generate the DOE is Simulia-Isight, provided by FCA. This software allows for the use of DOE for surrogate modelling. The optimality criteria used by Isight in the use of the OLHS method is described in Chapter 2.

Using the OLHS method in the Isight software, a set of 24 cases was generated, satisfying the requirement the number of initial DOE cases is at least three times the number of inputs. For each case, the value of each input parameter into the CFD simulations is shown in Appendix A.

ETR^4 and Re_J are bound within the engine map (before the catalytic converter) that was shown previously, while the Re_V values are sampled from their defined range. Boundary conditions for the CFD exhaust inlet and isothermal part temperatures are extracted from the GT-Power model for each specific case defined by the sampling.

3.5 Surrogate Model Generation

The 24 CFD experiments are completed with the parameter values set from the DOE. The output of interest (maximum fascia temperature) is extracted from the CFD results. The initial surrogate model (SM_1) is then generated using the experimental CFD results with the approximation model of choice. To construct the surrogate model, Isight allowed for the use of Kriging, Radial Basis Functions, or Elliptical Basis Functions. Their functions are defined in Chapter 2.

A priori, it was unknown which approximation method would result in the lowest surrogate model error. A set of CFD experiments, separate from the DOE is used to assess the error of the surrogate model. Each approximation model is assessed and the model resulting in the least amount of error in (Chapter 4) is selected to use for SM_1. For increased accuracy, the final surrogate model (SM_2) is generated by adding the cases used to assess the different approximation models.

Chapter 4

Results

In this section, the CFD simulation results are assessed and the resultant surrogate model is analyzed. The prediction error of SM_1 is assessed using a set of CFD cases separate from the initial DOE. These cases individually modify the parameter values to also identify the physical mechanisms responsible for the observed trends. SM_2 is generated from the addition of these cases.

4.1 Assessment of CFD Results

As discussed in Chapter 3, experimental data was collected in the test cell at CTC. The CFD accuracy was assessed using the small domain without a trailer, consistent with the experimental configuration.

A drive-cycle using the baseline exhaust position was completed in the test cell and boundary condition values were extracted from the measured data. The non-geometric boundary conditions are shown in Table 4.1.

Table 4.1: Boundary conditions for assessment of CFD.

ETR^4	Re_J	Re_V	R
59.9	2.35×10^5	9.18×10^6	0.48

The assessment could not be made on the basis of θ_{FM} as the thermocouples in the experiment were not placed so as to capture the maximum fascia temperature. Figure 4-1 shows computed θ_F contours on the surface of the fascia together with numbered thermocouple locations in the experiment.

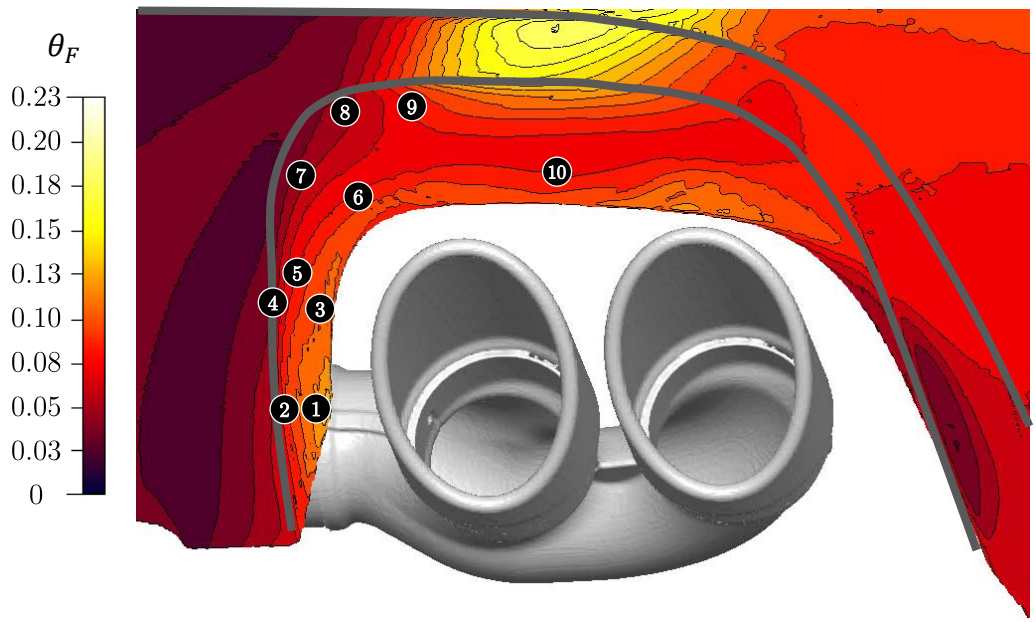

Figure 4-1: Thermocouple locations do not capture hotspot location.

Comparing θ_F values at the locations of the thermocouples between the CFD experimental data, good agreement is obtained. In areas where thermocouple data was available, the CFD predicts the θ_F value to be within 0.041 of the value measured experimentally. The absolute temperature difference as well as the absolute θ_F difference is represented in Table 4.2.

Table 4.2: Absolute difference in θ_F and temperature between CFD and experimentally measured values.

Thermocouple #	$\lvert\Delta\theta_F\rvert$	$\lvert\Delta T\rvert$[K]
1	0.010	5.54
2	0.041	22.7
3	0.037	20.5
4	0.039	21.6
5	0.024	13.3
6	0.028	15.5
7	0.025	13.9
8	0.027	15.0
9	0.029	16.1
10	0.020	11.1

To properly assess the surrogate model, experiments would need to be completed incorporating the trailer.

4.2 Model Construction

Resulting θ_{FM} values captured from the CFD simulations that made up the DOE are shown in Figure 4-2. The cases are defined in Appendix A. θ_{FM} ranged from 0.08 to 0.48.

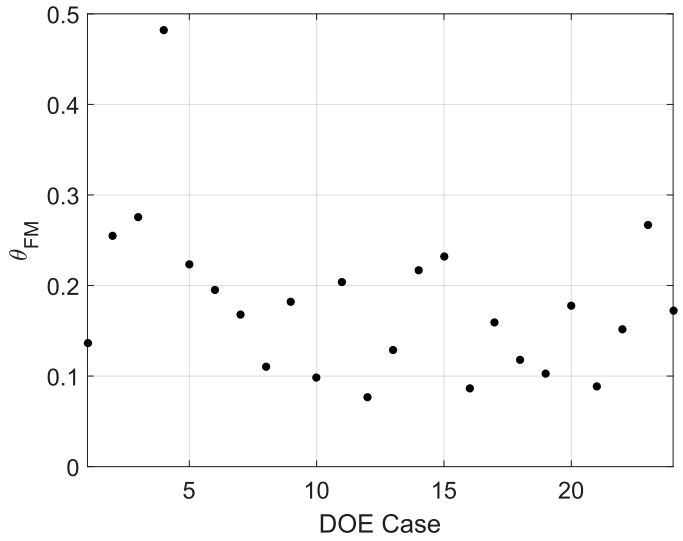

Figure 4-2: DOE Results.

4.3 Model Assessment

Cases at the minimum, midpoint, and maximum values of each of the geometric parameters were used to assess the error of SM_1, generated from the 24 cases in Figure 4-2. These cases are shown in Table 4.3.

4.3.1 Model Prediction Error

Prediction error was evaluated with the EBF, RBF, and Kriging approximation models using the cases in Table 4.3. The Kriging model resulted in the most error, averaging 30%, with a maximum of 73%. As mentioned in Chapter 2, Kriging models are semi-parametric and thus assume that there is a single global function between

the input and outputs, while incorporating a non-parametric covariance matrix. Due to the relationship between the inputs and output being highly non-linear, a single global function was not capable of predicting the output, resulting in a high amount of error.

Table 4.3: Model assessment cases.

<table>
<tr><th>X_+</th><th>Y_+</th><th>Z_+</th><th>β_+</th><th>ETR^4</th><th>Re_J</th><th>Re_V</th><th>R</th></tr>
<tr><td>0.9</td><td>0.5</td><td>0.5</td><td>0.21</td><td rowspan="10">88.3</td><td rowspan="10">3.66×10^5</td><td rowspan="10">5.45×10^6</td><td rowspan="10">0.20</td></tr>
<tr><td>0</td><td rowspan="3">0.5</td><td rowspan="3">0.5</td><td rowspan="3">0.21</td></tr>
<tr><td>0.5</td></tr>
<tr><td>1</td></tr>
<tr><td rowspan="2">0.9</td><td>0</td><td rowspan="2">0.5</td><td rowspan="2">0.21</td></tr>
<tr><td>1</td></tr>
<tr><td rowspan="2">0.9</td><td rowspan="2">0.5</td><td>0</td><td rowspan="2">0.21</td></tr>
<tr><td>1</td></tr>
<tr><td rowspan="3">0.9</td><td rowspan="3">0.5</td><td rowspan="3">0.5</td><td>0</td></tr>
<tr><td>0.5</td></tr>
<tr><td>1</td></tr>
</table>

The RBF and EBF models resulted in similar error due to their use of basis functions. The RBF model resulted in a maximum error of 49%, with an average of 18%, while the EBF model resulted in a maximum error of 45% with an average of 16%. As predicted in Chapter 2, the EBF model performed better than the RBF model due to its ability to weight each input. Thus, the EBF approximation model was selected to generate SM_1. The difference between the CFD values, θ_{FM} and the SM_1's predicted values, $\hat{\theta}_{FM}$, ranged from 0 to 0.16.

To increase the accuracy of SM_1, it was re-generated with all of the cases analyzed in the following sections to create the final surrogate model, SM_2. Any DOE data

used to generate an EBF model will lie directly on its surface. Thus, the model with the additional cases (SM_2) has no error with respect to the cases analyzed. Two models:

1. SM_1 - initial (without additional cases),
2. SM_2 - final (with additional cases)

are analyzed in the following sections. The resulting models' basis center array, scaling array, and covariance matrix are shown in Appendix 3-2.

4.3.2 Geometric Parameters

In this section, the effect of each geometric parameter in isolation is analyzed in detail to gain insight into the physical mechanisms governing the changes in maximum fascia temperature. Isolation was completed by modifying the parameter of interest, while keeping the others constant. Cases at the minimum, midpoint, and maximum value for each parameter is analyzed. For parameters X_+ and β_+, as shown in Table 4.3 an additional case was completed to capture the midpoint value, as the baseline geometry did not do so. The convective and radiative heat transfer fractions of the total heat transfer to the fascia are analyzed over the area outlined in Figure 4-3. The total heat transfer is taken over the whole area and for each specific parameter, it is normalized with respect to the case that results in the highest total heat transfer.

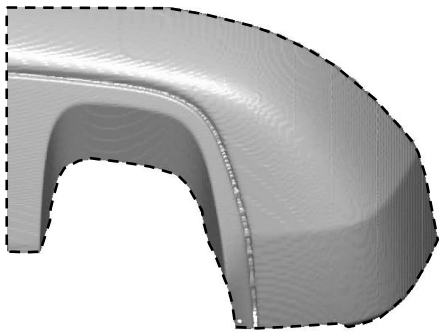

Figure 4-3: Fascia area used for heat transfer analysis.

4.3.2.1 X_+

In the CFD cases, Figure 4-4 displays θ_{FM} increasing as X_+ is increased.

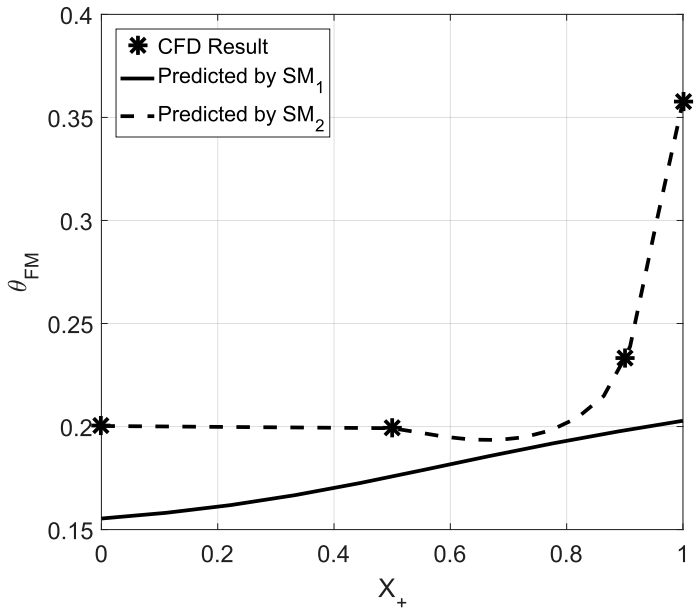

Figure 4-4: Predicted vs. CFD θ_{FM} values for X_+.

SM_1 shows a slightly non-linear increase of θ_{FM} as X_+ increases. Due to a lack of simulations in the design space as X_+ approaches one, SM_1 does not capture the large increase in θ_{FM}, resulting in a large amount of error. This increase is properly captured with SM_2 (with additional cases), which also predicts a slight decrease in θ_{FM} between X_+ values of 0.5 and 0.7. This is realistic and is detailed in the location analysis of X_+ further in this section. The exhaust jets may not impinge on the fascia until X_+ reaches 0.7, when the exhaust is more recessed within the fascia. This impingement is shown at the location of θ_{FM} in Figure 4-5 for X_+ values of 0.9 and 1. Additionally, the amount of radiative heat transferred to the hotspot at X_+ values of 0 and 0.5 is decreased as the exhaust recedes into the fascia. This total decrease in heat transfer decreases the θ_{FM} value.

Furthermore, from Figure 4-5 at an X_+ value of 0, it can be seen that 96% of the heat transferred to the fascia is via radiation due the large surface area of the exhaust

parts. The large surface area results in an increased view factor between the inboard exhaust tip and fascia, which is responsible for θ_{FM}. The exhaust jets are far from the fascia to avoid any interaction, reducing convective heat transfer fraction to the fascia. This is shown in Figure 4-6. The high decrease in convective heat transfer results in the lowest θ_{FM} value, 0.20, for the X_+ cases. The high amount of radiative heat transfer leads to the highest amount of total heat transfer to the fascia for the X_+ cases.

Receding the exhaust into the fascia to an X_+ value of 0.5, a high fraction of radiative heat transfer remains. There is a decrease in surface area in comparison to the minimum X_+ case, as can be seen in Figure 4-5, which decreases the total heat transfer to the fascia. Convective heat transfer is 6.0% of the total heat transfer to the fascia as the exhaust jets are still well away from the fascia, as shown in Figure 4-7. There is a decrease in total heat transfer to the fascia; however, θ_{FM} remains the same as the minimum X_+ case, as the view factor, and thus radiative heat transfer remains unchanged at the location of θ_{FM}.

At an X_+ value of 0.9, as a result of the decreased exhaust surface area and increased outboard exhaust jet interaction, in comparison to X_+ values of 0 and 0.5, there is an increase in convective heat transfer to the fascia and the radiative heat transfer drops to 83%. This is observed in the lower image in Figure 4-8, where there is noticeable interaction between the outboard exhaust jet and fascia. Due to this concentrated location of convective heat transfer, a change in the location of θ_{FM} occurs, as shown in Figure 4-5. Due to the reduction in radiative heat transfer, the total heat transfer to the fascia decreases, but due to the concentrated area of convective heat transfer from the exhaust jets on the fascia, the θ_{FM} value increases to a value of 0.23.

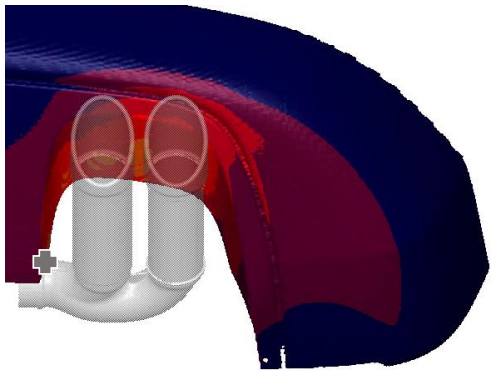

Minimum
$X_+ = 0$
$\theta_{FM} = 0.20$

Normalized Heat Transfer: 1

Heat Transfer Fraction %
Radiation: 96
Convection: 4.0

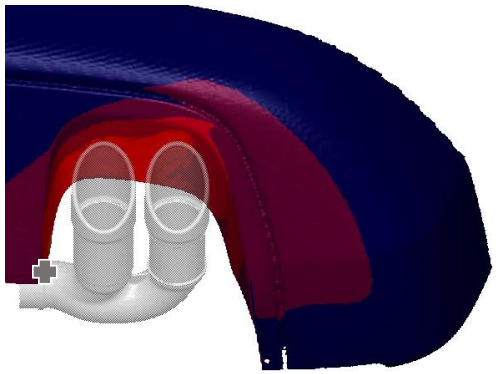

Midpoint
$X_+ = 0.50$
$\theta_{FM} = 0.20$

Normalized Heat Transfer: 0.74

Heat Transfer Fraction %
Radiation: 94
Convection: 6.0

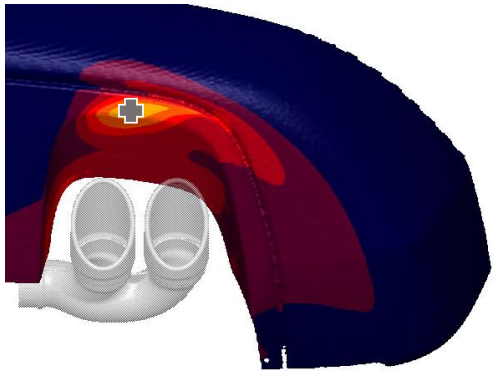

Baseline
$X_+ = 0.90$
$\theta_{FM} = 0.23$

Normalized Heat Transfer: 0.43

Heat Transfer Fraction %
Radiation: 83
Convection: 17

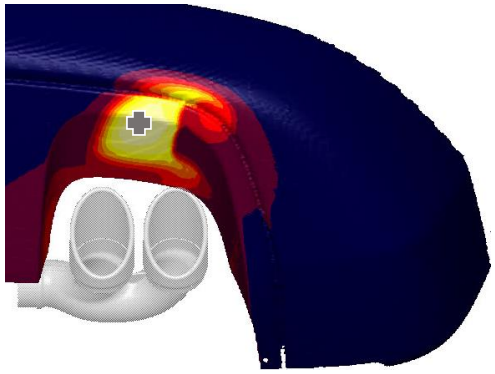

Maximum
$X_+ = 1$
$\theta_{FM} = 0.36$

Normalized Heat Transfer: 0.80

Heat Transfer Fraction %
Radiation: 36
Convection: 64

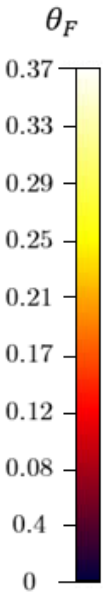

Figure 4-5: Heat transfer and θ_F values for X_+. θ_{FM} located with gray cross.

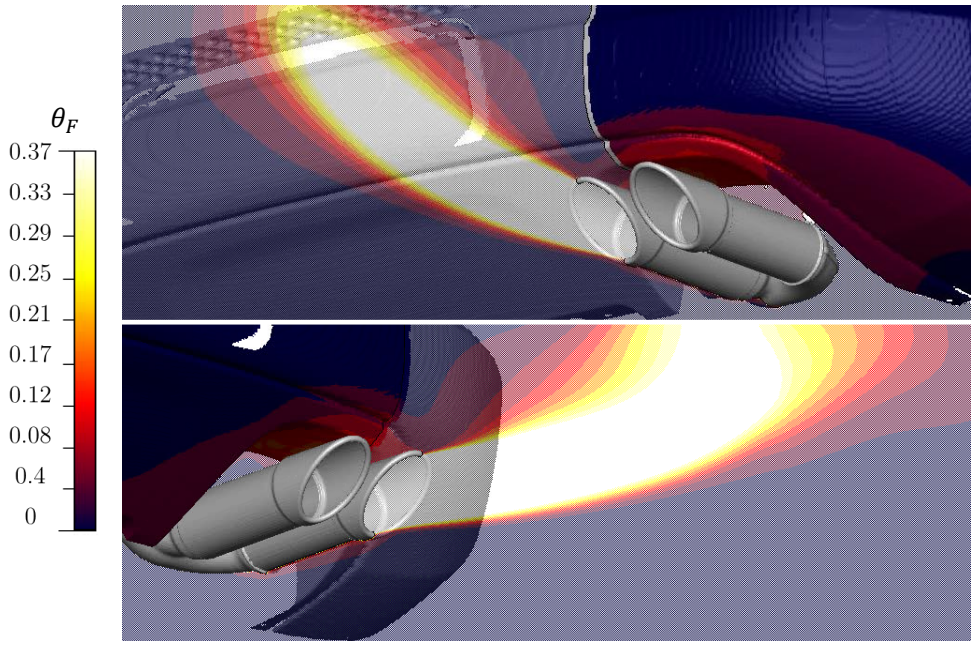

Figure 4-6: Exhaust jet and fascia θ_F contours for $X_+ = 0$. Top: view towards inboard exhaust tip, plane cut at centre of inboard exhaust tip; bottom: view towards outboard exhaust tip, plane cut at centre of outboard exhaust tip. Exhaust, as well as fascia surface behind plane do not have θ_F contours.

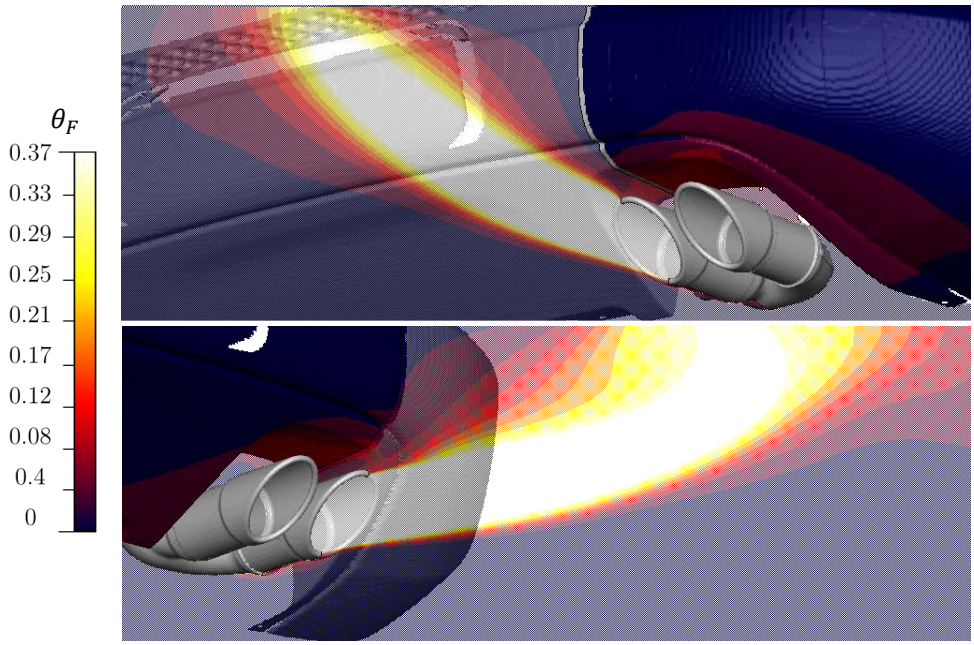

Figure 4-7: Exhaust jet and fascia θ_F contours for $X_+ = 0.5$. Top: view towards inboard exhaust tip, plane cut at centre of inboard exhaust tip; bottom: view towards outboard exhaust tip, plane cut at centre of outboard exhaust tip.

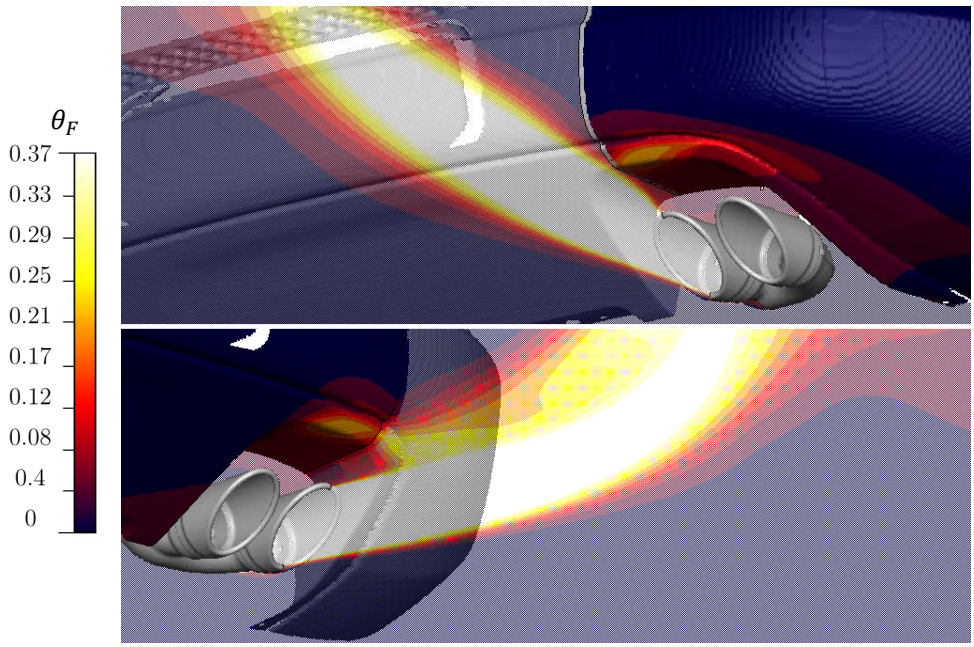

Figure 4-8: Exhaust jet and fascia θ_F contours for $X_+ = 0.9$. Top: view towards inboard exhaust tip, plane cut at centre of inboard exhaust tip; bottom: view towards outboard exhaust tip, plane cut at centre of outboard exhaust tip.

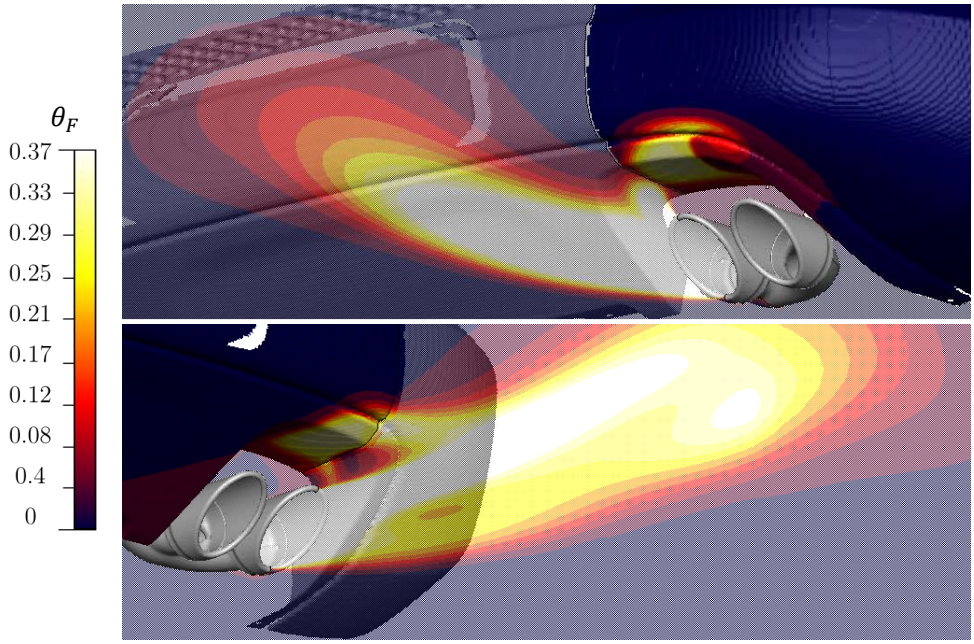

Figure 4-9: Exhaust jet and fascia θ_F contours for $X_+ = 1$. Top: view towards inboard exhaust tip, plane cut at centre of inboard exhaust tip; bottom: view towards outboard exhaust tip, plane cut at centre of outboard exhaust tip.

At an X_+ value of 1, the exhaust is fully recessed into the fascia. Due to a large

decrease in exhaust surface area and an area of concentrated jet interaction on the fascia, the convective heat transfer is 64% of the total heat transfer to the fascia. This is observed from both exhaust tips in Figure 4-9, where there is noticeable interaction of the jets with the fascia. This large increase in convective heat transfer increases the θ_{FM} value to 0.36, the highest out of the X_+ cases, as shown in Figure 4-5. Due to the θ_{FM} location being dominated by concentrated convective heat transfer, the location of θ_{FM} remains unchanged from the X_+ value of 0.9. The total heat transfer is the second highest out of the four X_+ cases investigated due to the decrease in radiation but high amount convective heat transfer.

Figure 4-10 shows the θ_F values measured at the two θ_{FM} locations for all four X_+ cases. These locations can be seen on the fascia in Figure 4-5. One location, radiation dominated (inboard corner) is the location for θ_{FM} at X_+ values of 0 and 0.5. The second, convection dominated (outside face of fascia), is the location for θ_{FM} at X_+ values of 0.9 and 1. Between X_+ values of 0.6 and 0.8, these two intersect and it would be expected that the θ_F value would be similar at each location. Depending on the value of θ_F, this has the potential to cause material failure at both locations.

At the radiation dominated location, the value of θ_F remains relatively constant due to the exhaust's constant view factor to the radiation dominated location, whether it is recessed into the fascia or not. After a value of 0.5, a slight decrease is shown as X_+ approaches one due to a slightly decreasing view factor of the exhaust parts the radiation dominated location. The trend predicted by SM_2 in Figure 4-4 coincides with the trend produced from CFD results in Figure 4-10. The trend from SM_2, although at a higher rate, predicts a decreasing θ_{FM} value between 0.5 and 0.7, in which the θ_{FM} value would be at the radiation dominated location. After an X_+ value of 0.7 where the two hotspots would likely intersect, SM_2 predicts an increase in θ_{FM} values, following the trend of the convection dominated hotspot location.

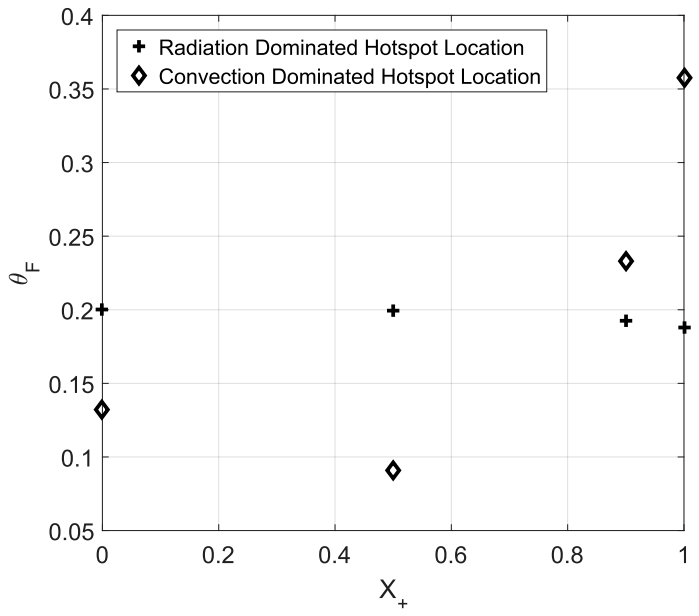

Figure 4-10: θ_F values for X_+ at the two locations of θ_{FM}, CFD results.

Minimizing X_+ values results in decreased θ_{FM} values due to the large decrease in concentrated convective heat transfer to the fascia. There are minimal increases in θ_{FM} values between 0 and 0.9, thus it is not recommended to increase the X_+ parameter past 0.9 as concentrated convective heat transfer occurs after this value.

4.3.2.2 Y_+

Figure 4-11 displays θ_{FM} decreasing as Y_+ is increased. SM_1 shows a slightly non-linear decrease of θ_{FM} as Y_+ increases. SM_1 captures the main trend; however, on average, underpredicts the θ_{FM} values by 0.026. SM_2 properly captures the trend as well as θ_{FM} values.

From Figure 4-12, at a Y_+ value of 0, 66% of the total heat transferred to the fascia is via radiation heat transfer. This is due to a high view factor to the fascia due to the exhaust's placement within the fascia. In Figure 4-13, both exhaust jets interact with the fascia, sweeping across it. The large amount of jet impingement on the fascia results in the highest θ_{FM} value, 0.26, for the Y_+ cases. This, in combination with

the high amount of radiative heat transfer leads to the highest amount of total heat transfer to the fascia for the Y_+ cases.

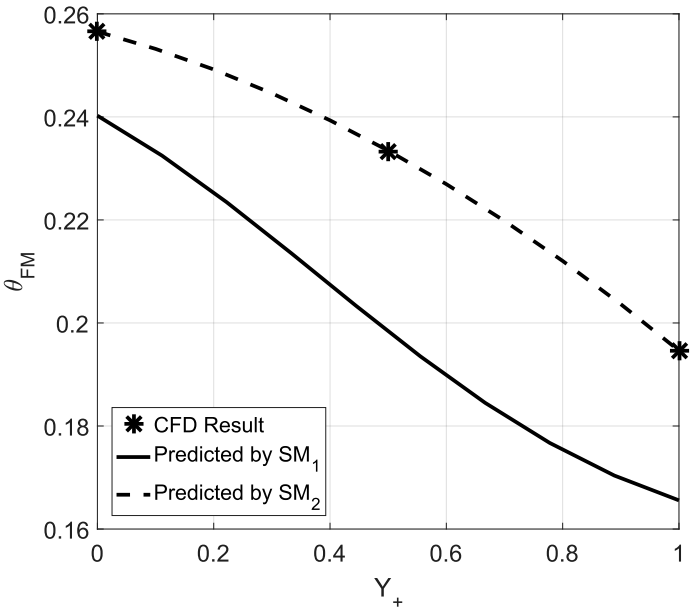

Figure 4-11: Predicted vs. CFD θ_{FM} values for Y_+.

The exhaust is centred within the fascia at Y_+ value of 0.5. A high fraction of radiative heat transfer to the fascia exists and there is a decrease in the convective heat transfer fraction in comparison to the minimum Y_+ case. Thus the fraction of radiation heat transfer increases to 83%. The decrease in convective heat transfer is due to the exhaust jets sweeping a lesser area of the fascia. This is shown in Figure 4-14. There is a decrease in total heat transfer to the fascia and θ_{FM} decreases in comparison the minimum Y_+ case, to a value of 0.23. The location of θ_{FM} remains similar, translated slightly in the direction of the translation of the exhaust, due to the impingement of the exhaust jets on the fascia being aligned with the exhaust tips.

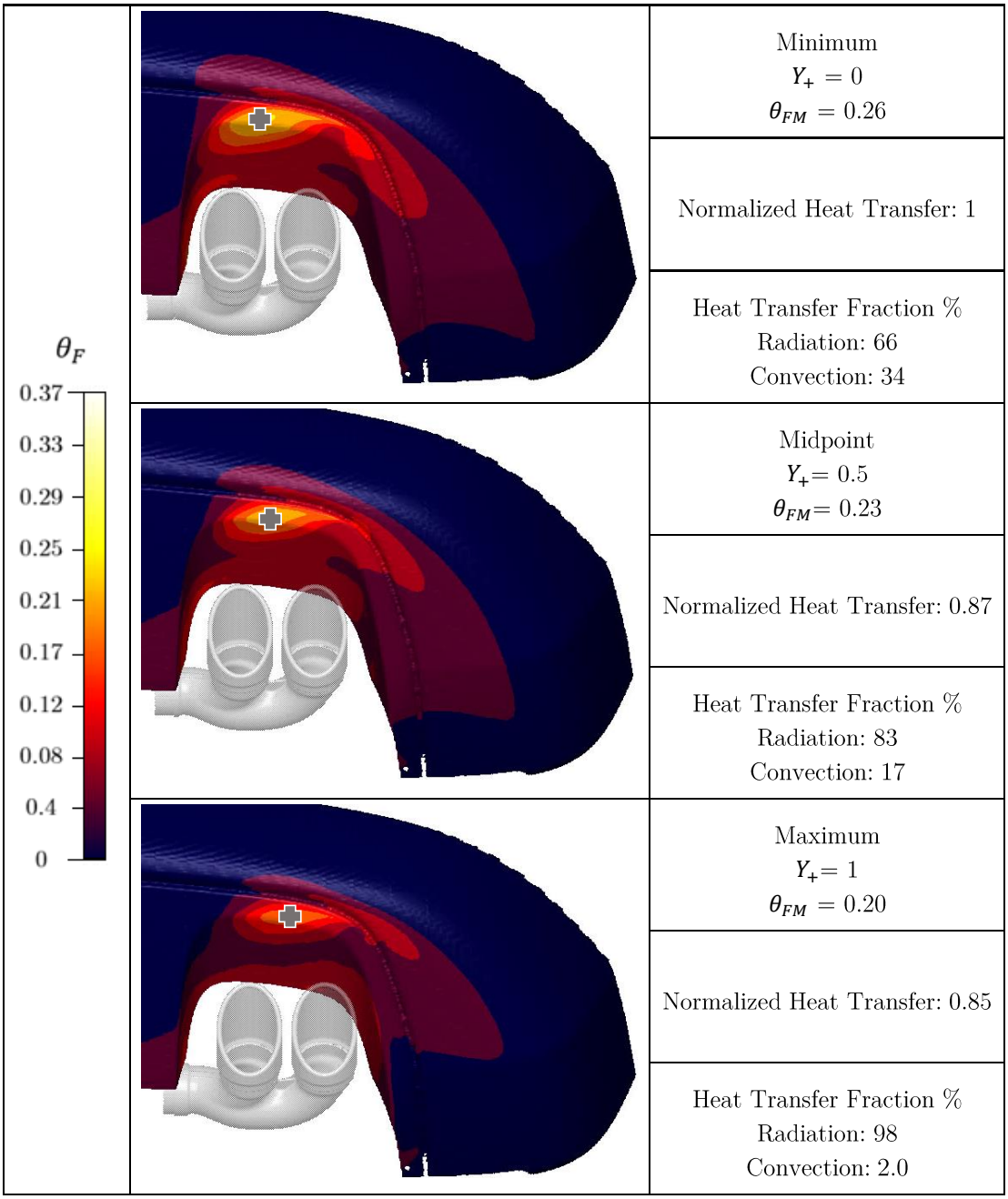

Figure 4-12: Heat transfer and θ_F values for Y_+.

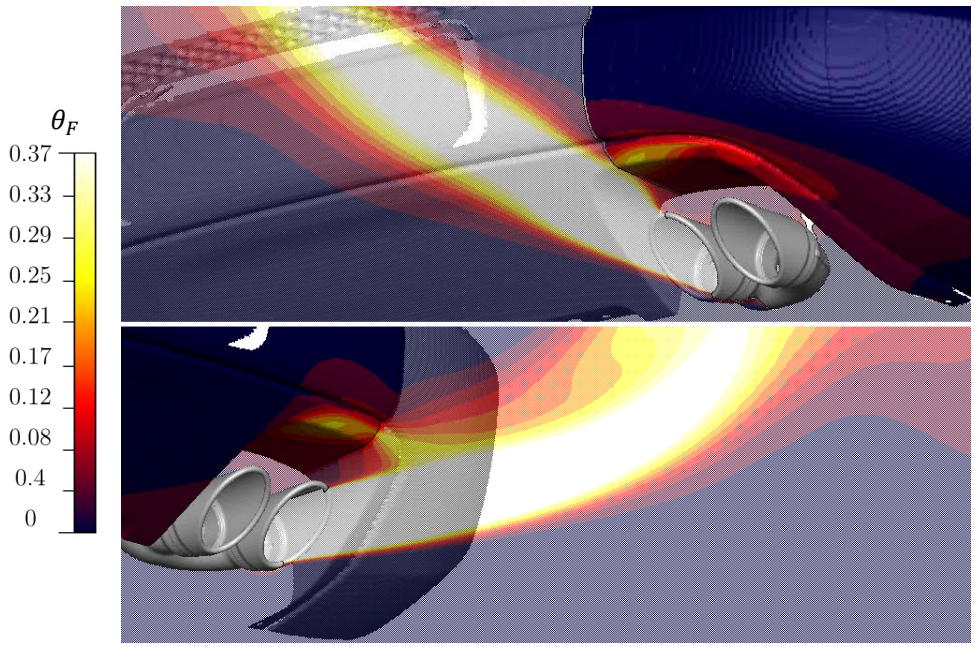

Figure 4-13: Exhaust jet and fascia θ_F contours for $Y_+ = 0$. Top: view towards inboard exhaust tip, plane cut at centre of inboard exhaust tip; bottom: view towards outboard exhaust tip, plane cut at centre of outboard exhaust tip.

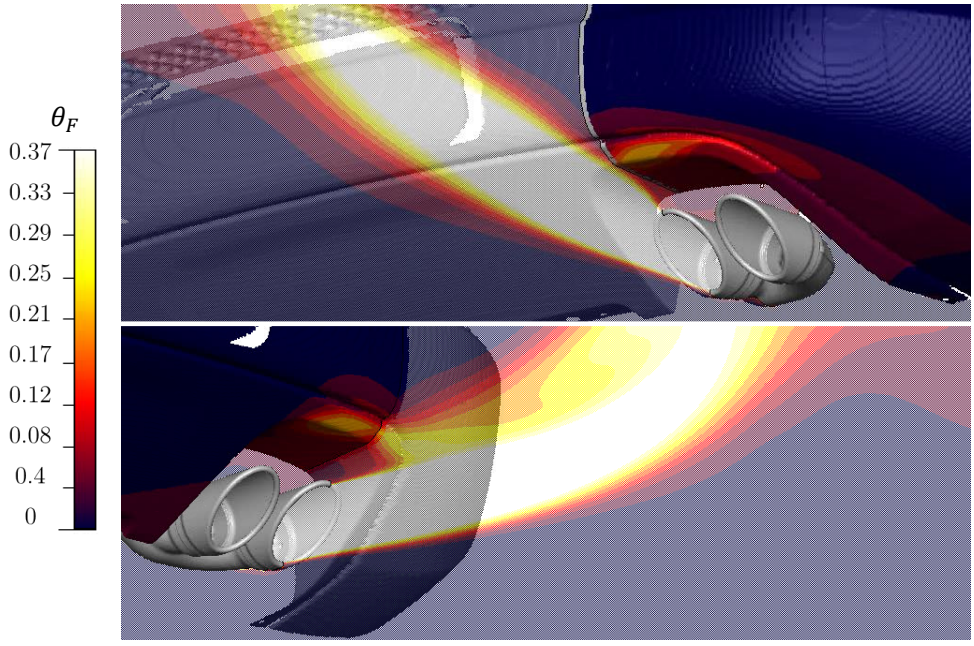

Figure 4-14: Exhaust jet and fascia θ_F contours for $Y_+ = 0.5$. Top: view towards inboard exhaust tip, plane cut at centre of inboard exhaust tip; bottom: view towards outboard exhaust tip; plane cut at centre of outboard exhaust tip.

Further translating the exhaust in the negative Y direction, the Y_+ value is at

1. The fraction of radiative heat transfer is high and there is a small fraction of convective heat transfer. 98% of the heat transferred to the fascia is via radiation. The convective heat transfer is decreased due to the exhaust jets sweeping over a lesser area of the fascia, shown in Figure 4-15. There is also an increase in radiative heat transfer due to the exhaust's view factor being increased to the outboard edge of the fascia. Overall, there is a decrease in total heat transfer to the fascia as well a decrease in θ_{FM}, to 0.20, which remains in the vicinity to the location of the other cases, again translated in the same direction of the exhaust tips, due to concentrated convective heat transfer in alignment with the exhaust tips.

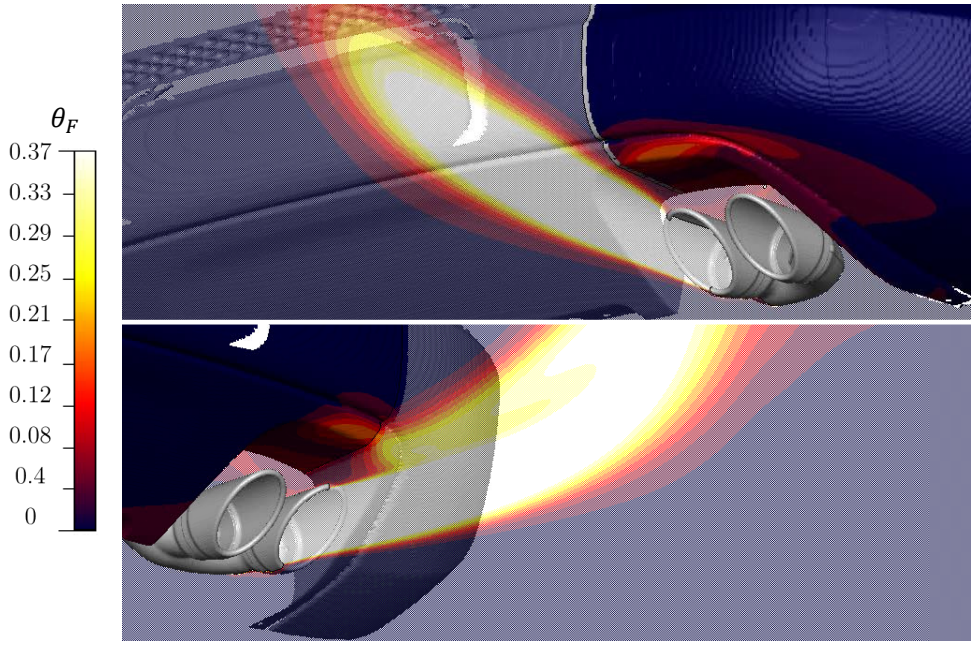

Figure 4-15: Exhaust jet and fascia θ_F contours for $Y_+ = 0.5$. Top: view towards inboard exhaust tip, plane cut at centre of inboard exhaust tip; bottom: view towards outboard exhaust tip, plane cut at centre of outboard exhaust tip.

Increasing Y_+ values translates the exhaust towards the outboard direction and decreases θ_{FM} values due to the decrease in concentrated convective heat transfer to the location of the hot spot observed for the cases analyzed.

4.3.2.3 Z_+

In the cases completed for Z_+, Figure 4-16 indicates that as Z_+ increases, θ_{FM} decreases in a trend similar to a concave up parabola with a local minimum. SM_1 gives a similar trend; however, on average, underpredicts θ_{FM} values by 0.058. SM_2 follows a similar trend, capturing the high θ_{FM} value at a Z_+ value of 0.

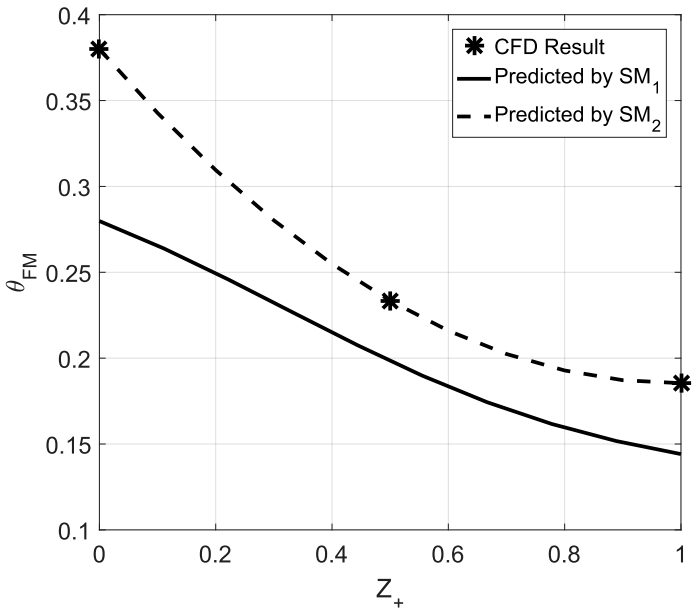

Figure 4-16: Predicted vs. CFD θ_{FM} values for Z_+.

From Figure 4-17, at a Z_+ value of 0, there is a similar fraction of both radiative (47%) and convective (53%) heat transfer to the fascia. The exhaust tips are within close vicinity to the top edge of the fascia and thus, there is a large view factor, as well high amount of exhaust jet interaction with the fascia. The concentrated convective heat transfer from both of the exhaust jets is shown in Figure 4-18. Due to this, at the minimum Z_+ value, both the highest amount of total heat transfer and θ_{FM} value, 0.38, for the Z_+ cases occurred.

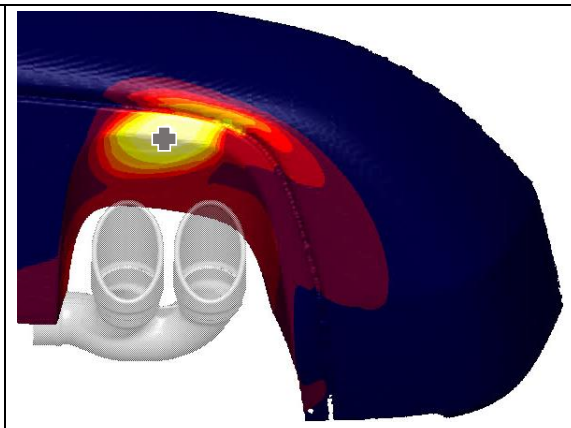

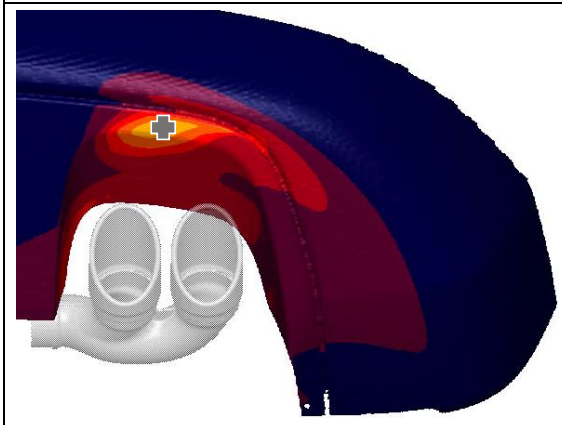

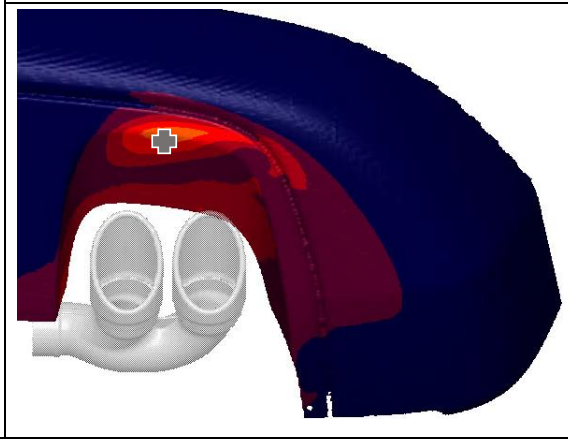

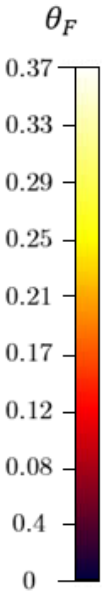

Minimum $Z_+ = 0$ $\theta_{FM} = 0.38$	
Normalized Heat Transfer: 1	
Heat Transfer Fraction % Radiation: 47 Convection: 53	
Baseline $Z_+ = 0.5$ $\theta_{FM} = 0.23$	
Normalized Heat Transfer: 0.56	
Heat Transfer Fraction % Radiation: 83 Convection: 17	
Maximum $Z_+ = 1$ $\theta_{FM} = 0.19$	
Normalized Heat Transfer: 0.39	
Heat Transfer Fraction % Radiation: 97 Convection: 3.0	

Figure 4-17: Heat transfer and θ_F values for Z_+.

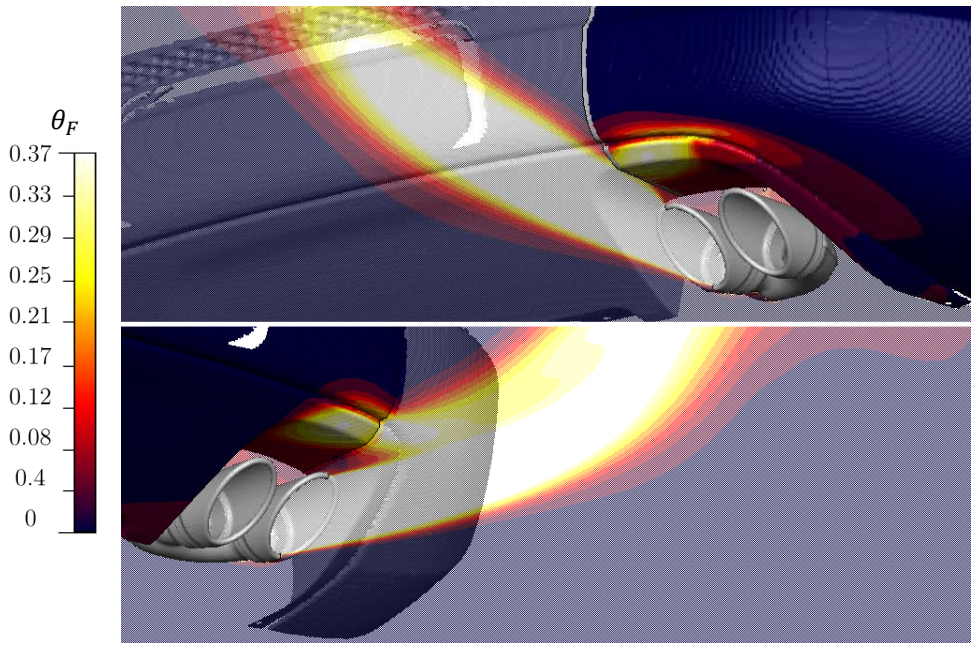

Figure 4-18: Exhaust jet and fascia θ_F contours for $Z_+ = 0$. Top: view towards inboard exhaust tip, plane cut at centre of inboard exhaust tip; bottom: view towards outboard exhaust tip, plane cut at centre of outboard exhaust tip.

At a Z_+ value of 0.5, due to the increased vertical distance between the fascia and exhaust tips, there is less convective heat transfer and as a result, there is a higher fraction of radiation heat transfer, 83%. There is a lesser amount of jet interaction with the fascia in comparison to the case at a minimum Z_+ value, as shown in Figure 4-19. Due to the decrease in convective heat transfer, with respect to the minimum case, the total heat transfer to the fascia is decreased, and θ_{FM}, which occurs in the same location, decreases to 0.23.

At the maximum Z_+ value, a large decrease in the convective heat transfer fraction is observed and thus the radiative heat transfer fraction is increased, accounting for 97% of the heat transferred to the fascia. This is due to the exhaust jets having little interaction with the fascia due to maximum Z_+ corresponding to the largest distance between the exhaust tips and fascia. This produces the lowest amount of total heat transfer out of the Z_+ cases, as well as the lowest θ_{FM} value, 0.19. In Figure 4-20, the outboard exhaust jet has some concentrated interaction with the fascia, where

the θ_{FM} occurs.

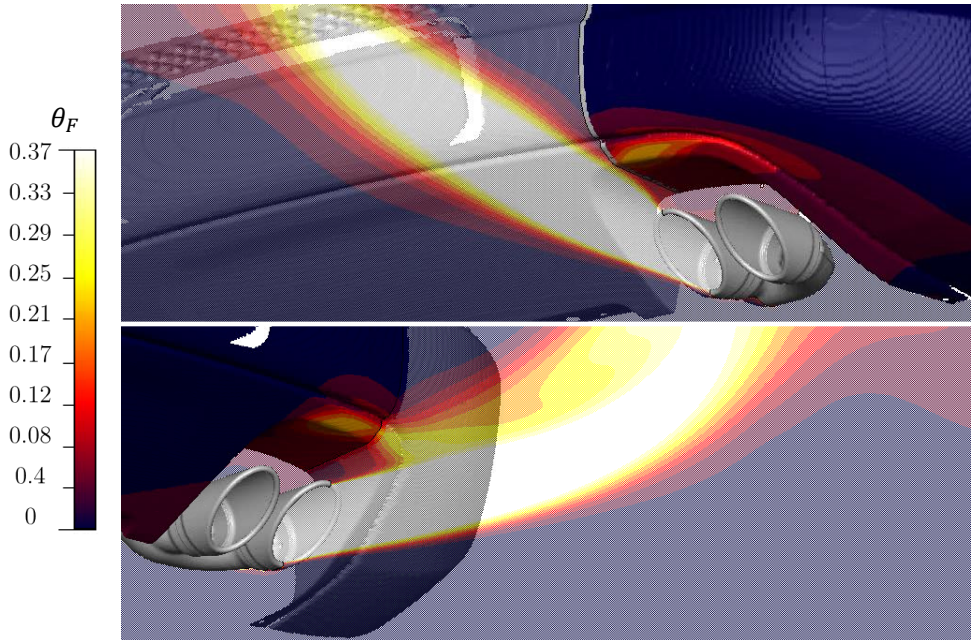

Figure 4-19: Exhaust jet and fascia θ_F contours for $Z_+ = 0.5$. Top: view towards inboard exhaust tip, plane cut at centre of inboard exhaust tip; bottom: view towards outboard exhaust tip, plane cut at centre of outboard exhaust tip.

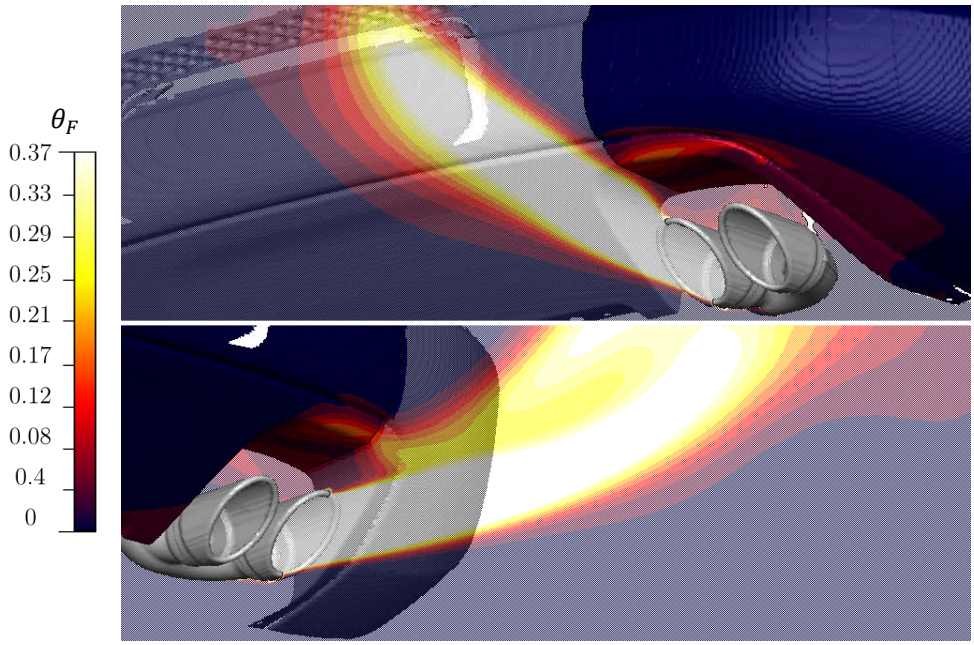

Figure 4-20: Exhaust jet and fascia θ_F contours for $Z_+ = 1$. Top: view towards inboard exhaust tip, plane cut at centre of inboard exhaust tip; bottom: view towards outboard exhaust tip, plane cut at centre of outboard exhaust tip.

Increasing Z_+ will always decrease θ_{FM} values and total heat transfer to the fascia, as observed in this subsection.

4.3.2.4 β_+

Due to the coupling between β_+, X_+, and Z_+, to isolate β_+, the angle of the exhaust tip was first rotated to its specific value, then the exhaust was swept or translated to its baseline X_+ and Z_+ value, respectively. From SM_2 and the CFD results, Figure 4-21 indicates that as β_+ increases, θ_{FM} follows a concave up, parabolic trend with a local minimum between 0 and 0.5, increasing as β_+ approaches 0.5, where a maximum is reached, and then decreasing linearly from 0.5 to 1, where its absolute minimum is reached. SM_1 has a large amount of error. This is due to few cases existing at the minimum value of β_+ in the initial DOE.

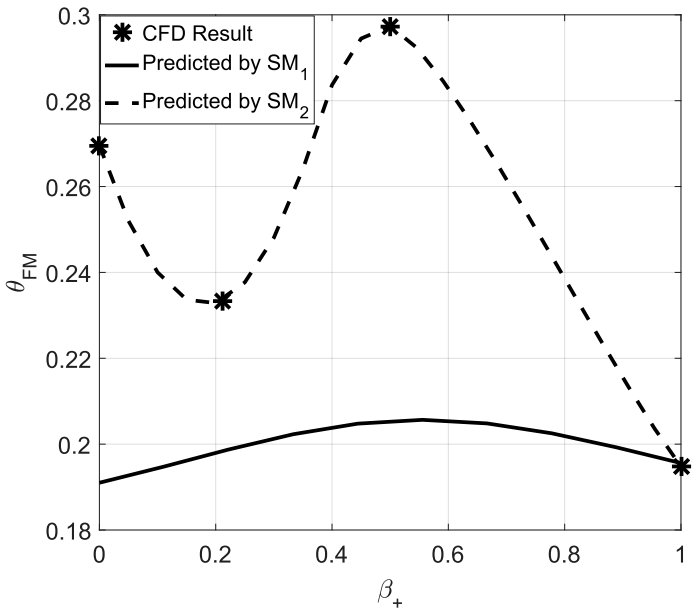

Figure 4-21: Predicted vs. CFD θ_{FM} values for β_+.

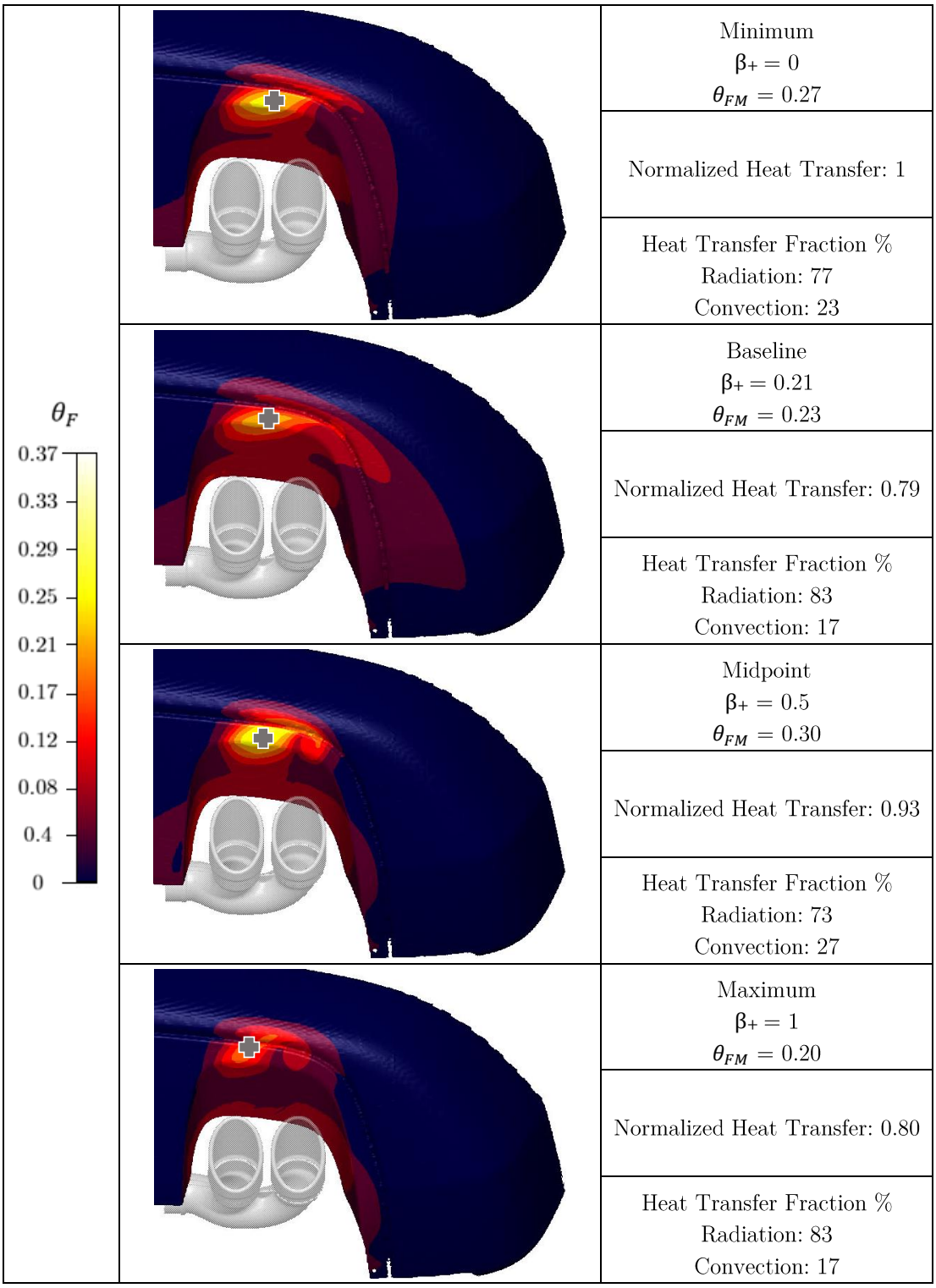

Figure 4-22: Heat transfer and θ_F values for β_+.

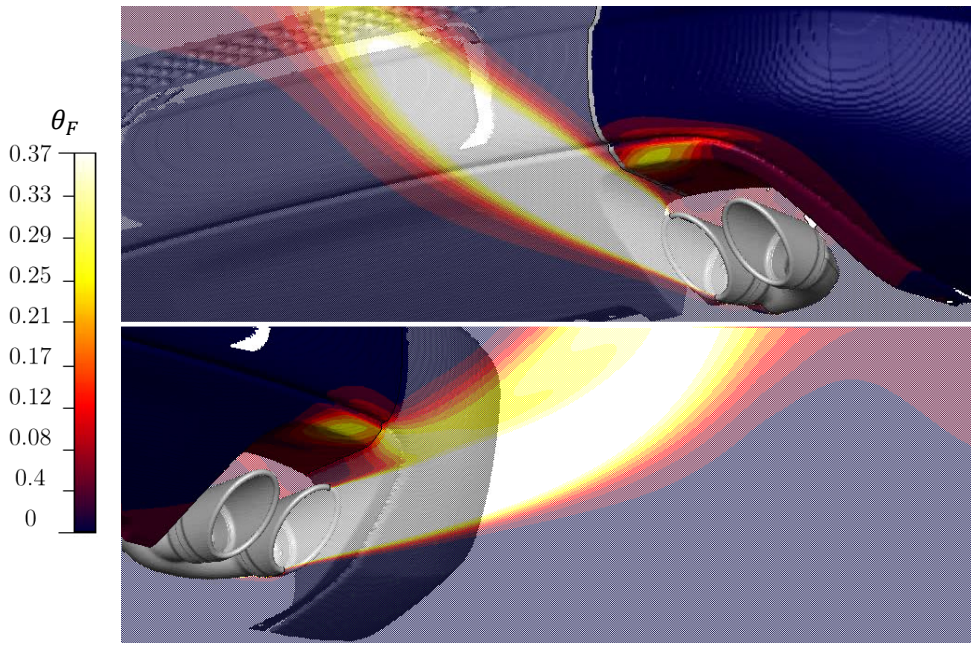

Figure 4-23: Exhaust jet and fascia θ_F contours for $\beta_+ = 0$. Top: view towards inboard exhaust tip, plane cut at centre of inboard exhaust tip; bottom: view towards outboard exhaust tip, plane cut at centre of outboard exhaust tip.

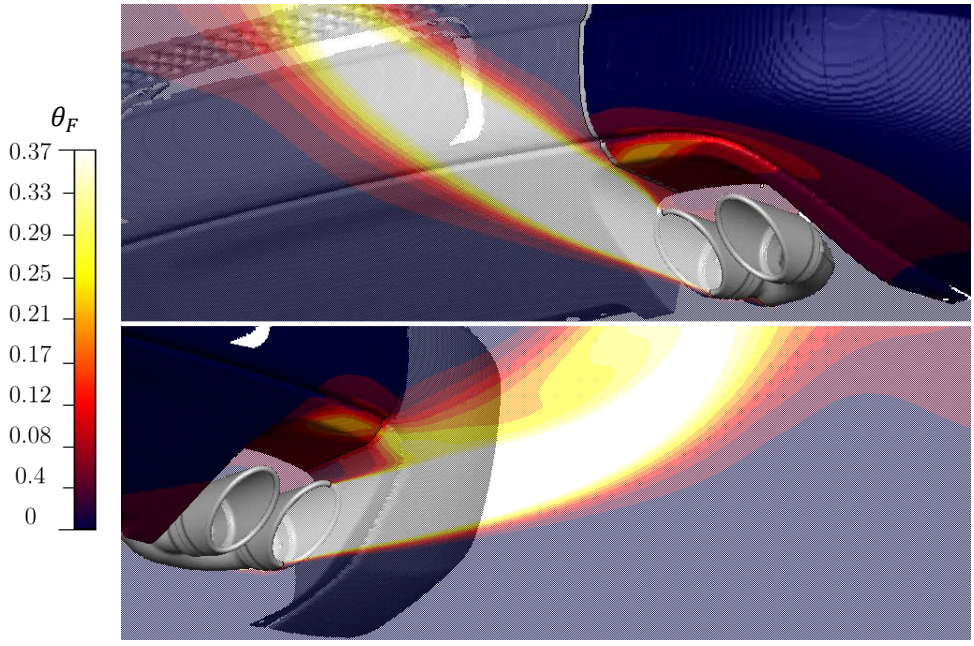

Figure 4-24: Exhaust jet and fascia θ_F contours for $\beta_+ = 0.21$. Top: view towards inboard exhaust tip, plane cut at centre of inboard exhaust tip; bottom: view towards outboard exhaust tip, plane cut at centre of outboard exhaust tip.

At a β_+ value of 0.21, in comparison to the minimum case, due to the increased

angle of the exhaust tips, a lower amount of convective heat transfer occurs. As a result, the radiative heat transfer fraction increases and is 83% of the total heat transferred to the fascia. The jets impinge on the fascia, resulting in an area of concentrated convective heat transfer, as shown in Figure 4-24; however, due to the decrease in convective heat transfer, there is a decrease in θ_{FM} to 0.23. Also occurring is a decrease in overall heat transfer. This is due to the decrease in convective heat transfer to the fascia.

At a β_+ value of 0.5, in comparison to the cases at 0 and 0.21, there is an increase in convective heat transfer fraction and a decrease in radiative heat transfer fraction, which becomes 73% of the heat transferred to the fascia. Unlike previous geometric cases where the under-body flow had less of an impact on θ_{FM}, at this β_+ value, the exhaust jets are directed by the under-body flow into the fascia from both the inboard and outboard exhaust tips, resulting in an area of highly concentrated convective heat transfer, as shown in Figure 4-25. As a result, θ_{FM} is highest out of the β_+ cases, 0.30. If there were no under-body flow, it would be expected that the θ_{FM} value would decrease, rather than increase due to the lack of under-body flow to direct the exhaust jets into the fascia.

At its maximum, due to the large downwards angle of the exhaust tips, there is a large decrease in convective heat transfer as there is decreased interaction between the fascia and the exhaust jets, especially from the outboard exhaust jet, as shown in Figure 4-26. In comparison to a β_+ value of 0.5, the angle of the exhaust with respect to the under-body flow is larger, and thus the inboard exhaust jet is dispersed, rather than directed into the fascia. This can be seen in Figure 4-26, where the size of the inboard exhaust jet is larger than in Figure 4-25. The majority of the heat transfer is via radiation, making up 83% of the heat transferred to the fascia. The lowest value of θ_{FM} (0.20), occurs due to the decrease in concentrated convective heat transfer to the hotspot location, one that remains constant throughout the β_+ analysis, as can

be seen in Figure 4-22.

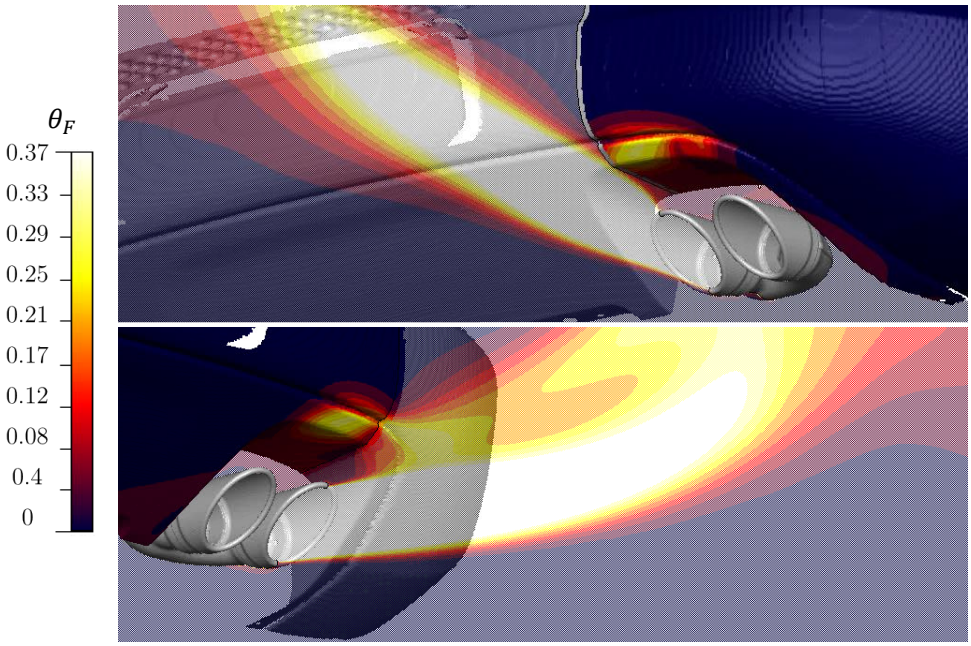

Figure 4-25: Exhaust jet and fascia θ_F contours for $\beta_+ = 0.5$. Top: view towards inboard exhaust tip, plane cut at centre of inboard exhaust tip; bottom: view towards outboard exhaust tip, plane cut at centre of outboard exhaust tip.

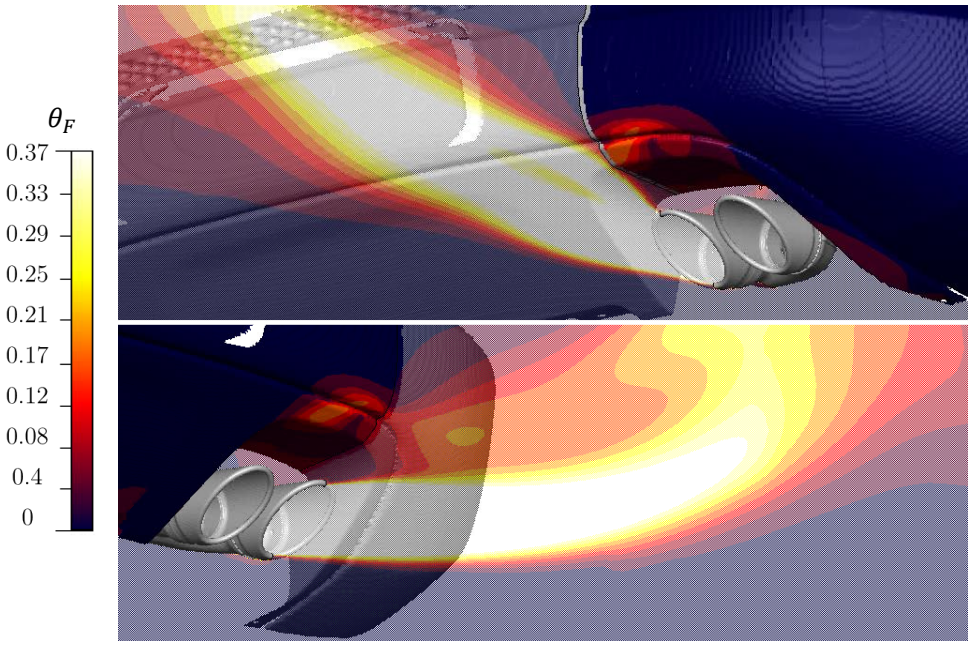

Figure 4-26: Exhaust jet and fascia θ_F contours for $\beta_+ = 1$. Top: view towards inboard exhaust tip, plane cut at centre of inboard exhaust tip; bottom: view towards outboard exhaust tip, plane cut at centre of outboard exhaust tip.

Existing at a consistent location due to concentrated convection heat transfer, between β_+ values of 0 and 0.21 there is a small decrease in θ_{FM}, which reaches a minimum. θ_{FM} increases as β_+ approaches 0.5, where a maximum is found. θ_{FM} then decreases as β_+ increases, reaching the lowest value of θ_{FM} at a β_+ value of 1. In Figure 4-27, without the interaction of under-body flow, at an Re_V value of 0, SM_2 predicts that the θ_{FM} would decrease as β_+ increases due to decreased convective heat transfer. Regardless of under-body flow, the lowest value of θ_{FM} occurs at a β_+ value of 1, so to reduce θ_{FM}, a large exhaust tip angle is suggested.

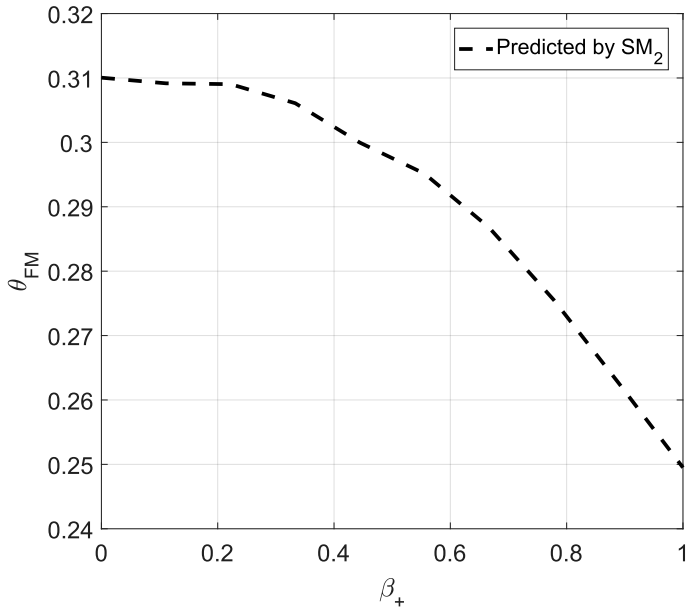

Figure 4-27: θ_{FM} prediction with increasing β_+ values at a Re_V value of 0.

4.3.3 Non-Geometric Parameters

In this subsection, the effect of each non-geometric parameter is analyzed in detail to gain insight into the physical mechanisms governing the changes in θ_{FM}. The analysis is completed with FCA's baseline exhaust positioning. Minimum, midpoint, and maximum cases are analyzed for ETR, while Re_J, and Re_V are analyzed together through the use of the velocity ratio, R. SM_1 is now removed from the analysis to

solely focus on SM_2 and the CFD results.

4.3.3.1 Exhaust Temperature

Defined in Chapter 3, the exhaust temperature ratio, ETR, non-dimensionally defines the ratio between the exhaust gas temperature and the ambient temperature of the system. The importance of radiation is captured by calculating the ratio to the fourth power.

Increasing the ETR was done alongside Re_J due to the engine map. As Table 4.4 indicates, Re_V remained constant for the three cases analyzed. As discussed in Chapter 3, θ_{FM} does not allow for straightforward analysis when ETR values are varying. This is the case in Table 4.4, where θ_{FM} is decreasing as ETR^4 values increase. The maximum fascia temperature is increasing with ETR^4; however, since the denominator of θ_{FM}, $(T_{Exhaust\,Gas} - T_{Ambient})$, increases as ETR^4 increases, the resultant θ_{FM} value is lower. Through the use of $\theta_{FM}*$, in which the denominator, $(max(T_{Exhaust\,Gas}) - T_{Ambient})$, uses the exhaust gas temperature from the case with the highest ETR^4, θ_{FM} is normalized and straightforward analysis follows.

Shown in Table 4.4, as ETR^4 increases, so does $\theta_{FM}*$. This corresponds to the maximum fascia temperature increasing as ETR^4 increases. As shown in Figure 4-28, the minimum ETR case ($ETR^4 = 2.05$) lies at the bounded corner of the engine map and thus only occurs for a single Re_J value. As Re_J is changing for the cases analyzed in Table 4.4, to fully isolate the trend ETR^4 has on $\theta_{FM}*$, ETR^4 is analyzed with respect to a constant Re_J and Re_V, and thus a constant R value. The Re_J values, at which the midpoint and maximum cases occur, span multiple ETR^4 values across the engine map as shown in Figure 4-28.

Table 4.4: Cases analyzed for exhaust temperature.

Case	ETR^4	Re_J	Re_V	R	θ_{FM}	$\theta_{FM}*$
Minimum	2.05	8.14×10^3	5.45×10^6	8.81	0.37	0.02
Midpoint	88.3	3.66×10^5		0.20	0.23	0.16
Maximum	253	4.28×10^5		0.17	0.21	0.21

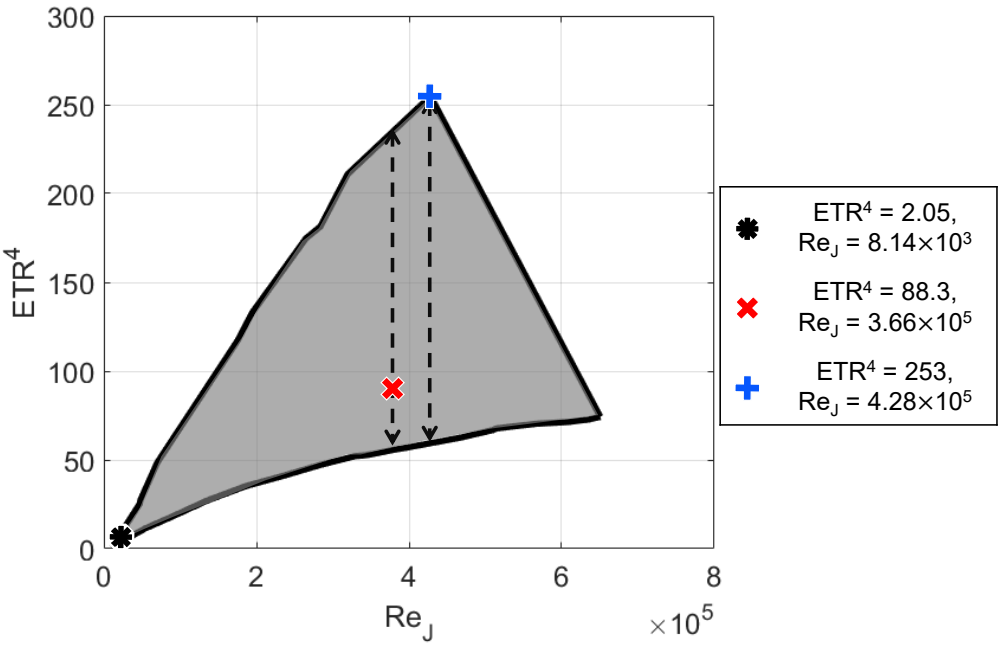

Figure 4-28: ETR^4 cases studied, shown on the engine map.

To remove any influence of Re_J on the trend of ETR on $\theta_{FM}*$, the trend predicted by SM_2 passing through the midpoint and maximum case, is shown in Figure 4-29. A similar trend for both Re_J values is shown. As ETR^4 is increased, both radiation and convective heat transfer are increased due to the increase in temperature difference between the exhaust jets, parts, and fascia. Thus, as ETR increases, θ_{FM} increases.

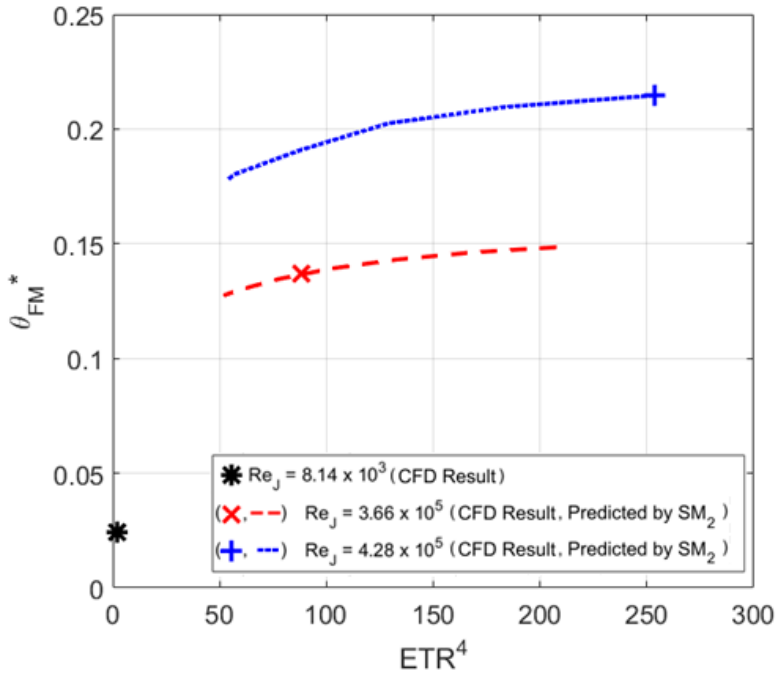

Figure 4-29: Predicted vs. CFD θ_{FM} values for ETR^4.

4.3.3.2 Vehicle Speed and Exhaust Velocity

Vehicle speed and thus Re_V defines the external flow around the vehicle. The under-body flow interacts with both the rear fascia as well as the exhaust jets, having potential to increase or decrease θ_{FM} values. The under-body flow contributes to convective cooling of the rear fascia; however, it also has the ability to disperse the exhaust jets or to direct them towards the fascia. The velocity of the exhaust inlet, and thus Re_J determines the strength of the exhaust jets. The velocity ratio (R) determines the ability of the exhaust jets to stay coherent or to resist re-direction due to the under-body flow.

To further understand the coupling of Re_V and Re_J, the following analysis is completed with constant ETR^4 value. Three separate Re_J values are studied. For each Re_J value, simulations are completed at a minimum, midpoint, and maximum Re_V. The cases analyzed are shown in Table 4.5.

Table 4.5: Cases simulated with CFD for Re_V and Re_J analysis.

ETR^4	Re_V	Re_J	R
88.3	0	1.23×10^5	0
		3.66×10^5	0
		6.06×10^5	0
	5.45×10^6	1.23×10^5	0.58
		3.66×10^5	0.20
		6.06×10^5	0.12
	1.09×10^7	1.23×10^5	1.2
		3.66×10^5	0.39
		6.06×10^5	0.24

The θ_{FM} values of the cases in Table 4.5 are shown in Figure 4-30. The general trend of Re_V on θ_{FM} values is a concave up parabola, with a local minimum, and varying rates of change, dependent on Re_J. As Re_J increases, so does the rate of change of the trend. At $Re_V = 0$, maximum θ_{FM} values are found. As Re_V increases, θ_{FM} decreases to a local minimum, and then increases as Re_V increases.

At the largest Re_V value studied (1.09×10^7), the θ_{FM} value is always less than that at $Re_V = 0$. However, if the range of Re_V were expanded, there is potential that the trend would continue and a θ_{FM} value higher than that at $Re_V = 0$ may occur. SM_2 captures the same values as the CFD results and follows the observed trend, a concave up parabola with varying rates of change.

In Figure 4-30 it can be seen that at the minimum and maximum Re_V, a larger Re_J value results in a higher θ_{FM} value. At the midpoint Re_V value, this trend does not continue due to the interaction of the under-body flow and exhaust jets. CFD results in Figure 4-30 are further analyzed below with respect to the velocity ratio to determine the physical mechanisms responsible for the inversion of the trend at

$Re_V = 5.5 \times 10^6$.

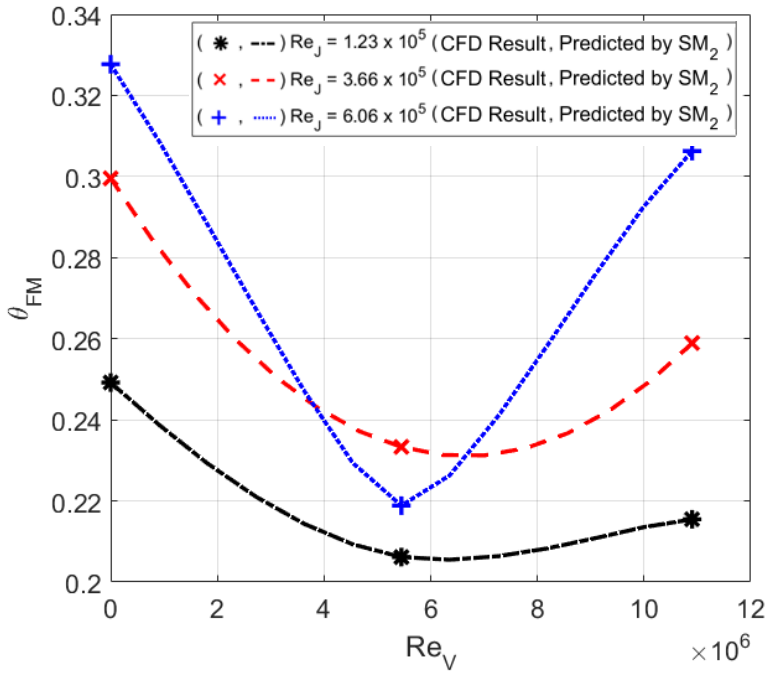

Figure 4-30: Predicted vs. CFD θ_{FM} values for increasing Re_V with increasing Re_J.

4.3.3.3 R=0

For the lowest R values, the exhaust jets remain coherent and the under-body flow does not have the ability to direct the exhaust jets towards the fascia, resulting in decreased convective heat transfer. Radiative heat transfer from the exhaust components determines the θ_{FM} value. At $Re_V = 0$, the resulting R value is 0 and no under-body flow cools the fascia. Likewise, there is no external flow for the exhaust jets to interact with. The exhaust jets can not be dispersed or directed towards the fascia.

At an R value of 0, for the lowest Re_J value (1.23×10^5), 58% of the heat transfer to the fascia is via convection. The high amount of convective heat transfer is due to the inboard exhaust jet interacting with the fascia. This interaction is shown in Figure 4-32. The interaction, although concentrated, results in a lower θ_F value than

in the inboard corner of the fascia, where θ_{FM} occurs, as shown in Figure 4-31. The lowest θ_{FM} and total heat transfer occurs at the lowest Re_J value, as the exhaust components are at their lowest temperature, resulting in less heat transfer. As Re_J increases, so does the temperature of the components. Although the exhaust gas temperature at the CFD inlet is the same for all cases, the exhaust components are not the same temperature, due to the difference in exhaust velocity. This is due to increased heat transfer to the exhaust components as higher velocity gas flows through them.

At the midpoint Re_J value (3.66×10^5), the radiative heat transfer fraction increases to 61% as a result of the increased temperature of the exhaust components. In comparison the the minimum Re_J case (Figure 4-32), the flow out of the inboard exhaust tip in Figure 4-33 is similar. There is slightly more interaction with the fascia, as shown on the θ_F contours in Figure 4-31, where θ_F values are higher. The location of θ_{FM} remains the same and the total heat transfer and θ_{FM} value (0.30) increases with the increased Re_J value.

At the maximum Re_J value (6.06×10^5), the convection heat transfer fraction decreases to 21% and the highest total heat transfer, as well as θ_{FM} value (0.33) is observed in Figure 4-31. Increased concentrated convective heat transfer occurs from the interaction between the flow out of the inboard exhaust tip and the fascia as shown on the θ_F contours in Figure 4-34. However, due to a lack of cool under-body flow, the location of θ_{FM} is unchanged, at the inboard side of the fascia.

At an R value of 0, for a constant ETR, the θ_{FM} value is dependent on Re_J. As Re_J increases, as does the temperature of the exhaust components, increasing the temperature difference between the fascia and these components. With radiation heat transfer being responsible for θ_{FM}, at an R value of 0, and thus Re_V value of 0, θ_{FM} increases as Re_J increases.

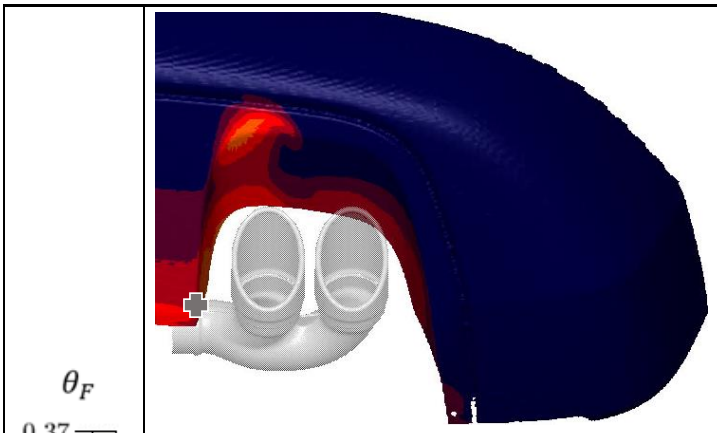

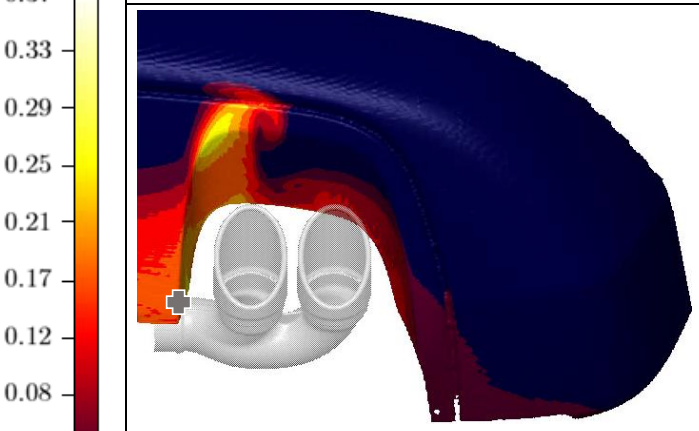

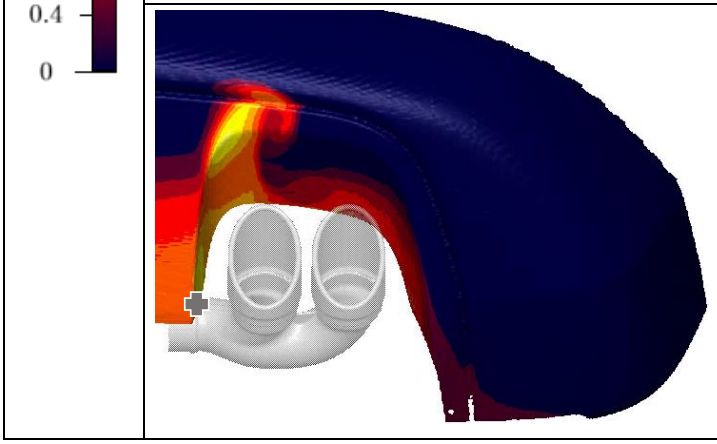

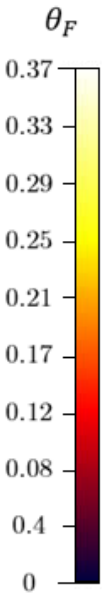

Minimum $Re_J = 1.23 \times 10^5$ $Re_V = 0$, R = 0 $\theta_{FM} = 0.25$	
Normalized Heat Transfer: 0.37	
Heat Transfer Fraction % Radiation: 42 Convection: 58	
Midpoint $Re_J = 3.66 \times 10^5$ $Re_V = 0$, R = 0 $\theta_{FM} = 0.30$	
Normalized Heat Transfer: 0.67	
Heat Transfer Fraction % Radiation: 61 Convection: 39	
Maximum $Re_J = 6.06 \times 10^5$ $Re_V = 0$, R = 0 $\theta_{FM} = 0.33$	
Normalized Heat Transfer: 1	
Heat Transfer Fraction % Radiation: 79 Convection: 21	

Figure 4-31: Heat transfer and θ_F values for $R = 0$, increasing Re_J.

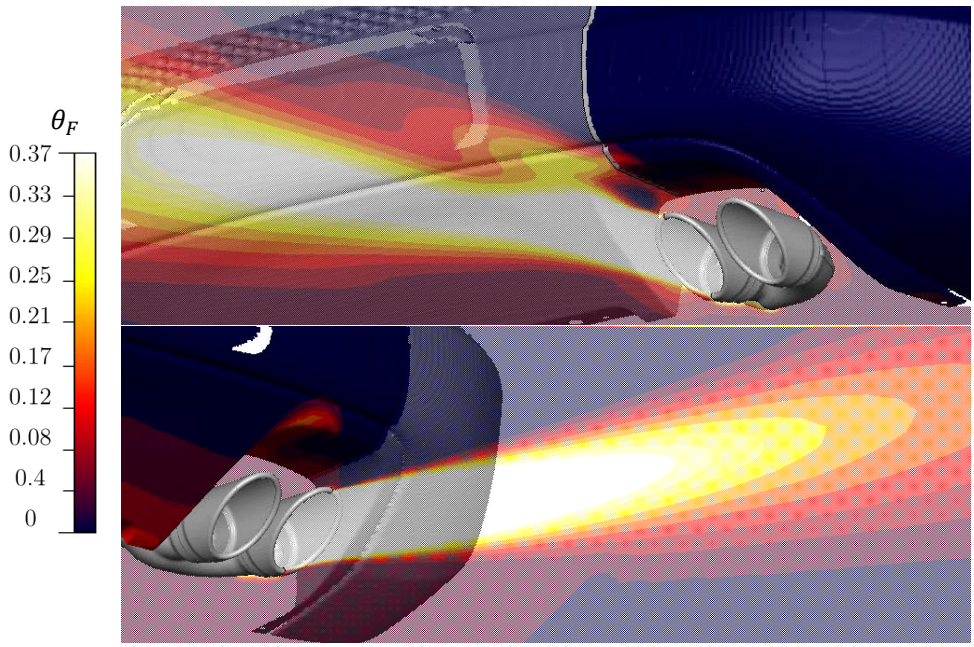

Figure 4-32: Exhaust jet and fascia θ_F contours for $R = 0$, $Re_J = 1.23 \times 10^5$. Top: view towards inboard exhaust tip, plane cut at centre of inboard exhaust tip; bottom: view towards outboard exhaust tip, plane cut at centre of outboard exhaust tip.

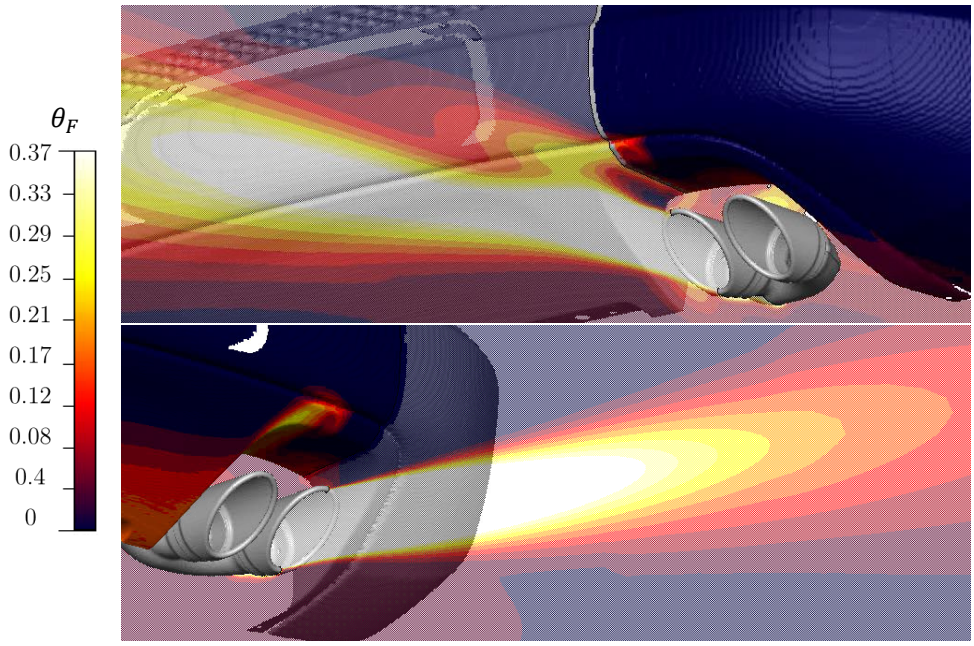

Figure 4-33: Exhaust jet and fascia θ_F contours for $R = 0$, $Re_J = 3.66 \times 10^5$. Top: view towards inboard exhaust tip, plane cut at centre of inboard exhaust tip; bottom: view towards outboard exhaust tip, plane cut at centre of outboard exhaust tip.

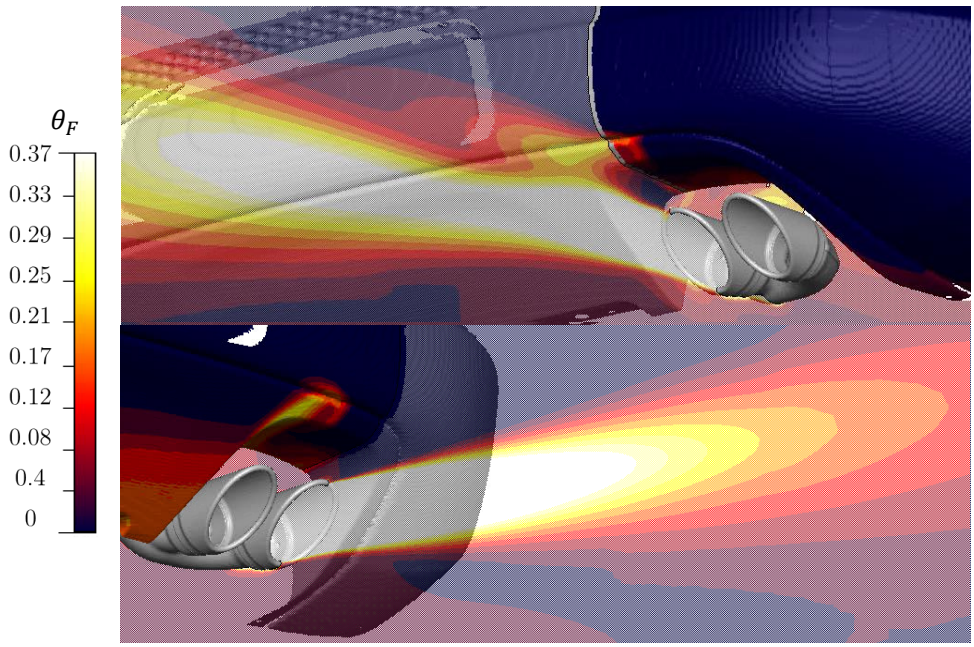

Figure 4-34: Exhaust jet and fascia θ_F contours for $R = 0$, $Re_J = 6.06 \times 10^5$. Top: view towards inboard exhaust tip, plane cut at centre of inboard exhaust tip; bottom: view towards outboard exhaust tip, plane cut at centre of outboard exhaust tip.

4.3.3.4 R>0

For non-zero values of R, the resulting θ_{FM} values are plotted in Figure 4-35. Their respective Re_V and Re_J values are shown in Table 4.6. As values increase from 0.12 to 0.24, the exhaust jets will remain coherent; however, due the increasing strength of the under-body flow, the exhaust jets will be directed towards the fascia, resulting in areas of concentrated convective heat transfer, increasing θ_{FM} values. For R values above 0.24, the exhaust jets are not as strong and the higher strength under-body flow will disperse the exhaust jets, spreading them over a larger area of the fascia. This is shown in Figure 4-36, where the θ_F contours span a larger area of the fascia as R increases. With less concentrated convective heat transfer, this results in lower θ_{FM} values in comparison to the strong exhaust jets being directed towards the fascia. At a value of 1.2, the exhaust inlet velocity is less than the vehicle speed; however, it is still larger than the actual under-body flow velocity in the vicinity of the exhaust tip.

There exists a slightly higher θ_{FM} value than the case at 0.58 due to less dispersion of the exhaust jets. The decrease in dispersion and under-body flow velocity differing from the vehicle speed is discussed further in the analysis of the case for $R = 1.2$.

Table 4.6: Re_V and Re_J values for $R > 0$ and $ETR^4 = 88.3$.

R	Re_V	Re_J
0.12	5.45×10^6	6.06×10^5
0.20	5.45×10^6	3.66×10^5
0.24	1.09×10^7	6.06×10^5
0.39	1.09×10^7	3.66×10^5
0.58	5.45×10^6	1.23×10^5
1.2	1.09×10^7	1.23×10^5

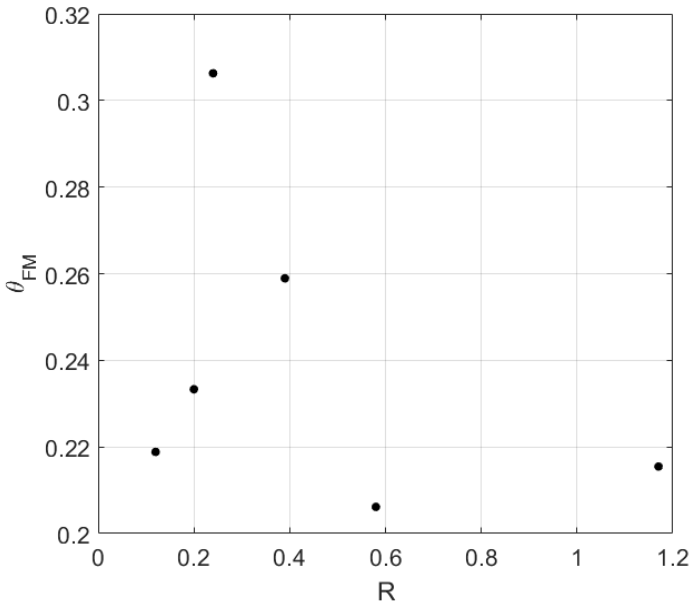

Figure 4-35: θ_{FM} values for $R > 0$ and $ETR^4 = 88.3$.

In Figures 4-35 and 4-36, the case with the lowest R value (0.12), results in one of the lowest θ_{FM} values (0.22). Due to the strength of the exhaust jets in comparison to the under-body flow, the exhaust jets are not directed towards the fascia, nor

dispersed over the fascia. This is shown in Figure 4-37. This results in a large radiation heat transfer fraction (93%). The resulting θ_{FM} is the same location as the cases with an R value of 0. It is expected that below an R value of 0.12, that the mechanism responsible for θ_{FM} is radiation heat transfer, as the exhaust jets will be well away from the fascia.

At an R value of 0.20, the convective heat transfer fraction increases to a value of 17%. As shown in Figure 4-38, the exhaust jets remain coherent; however, they are directed towards the fascia. In comparison to the case at an R value of 0.12, the location of θ_{FM} changes to the location of concentrated convection and has a small increase, to 0.23.

At an R value of 0.24, the convective heat transfer increases to 18% and the highest θ_{FM} value (0.31) occurs. The exhaust jets have enough strength to remain coherent; however, the under-body flow also has enough strength to direct the jets towards the fascia. The exhaust jets interact with the fascia at an area of concentrated convective heat transfer that can be seen in Figure 4-39.

At an R value of 0.39, the convective heat transfer fraction increases to 70%. The exhaust jets are not strong enough to remain coherent and are dispersed over the area of the fascia, as shown in Figure 4-40. With less concentrated convective heat transfer than the case at an R value of 0.24, a lower θ_{FM} value (0.26) is observed and the total heat transfer increases due to the distributed convective heat transfer over the surface of the fascia.

At an R value of 0.58, the strength of the exhaust jets is decreased more in comparison to the under-body flow and the convective heat transfer fraction increases to 92%. In Figure 4-41 it can be seen that the exhaust jets are dispersed over a larger area of the fascia in comparison to all non-zero R cases, resulting in the highest total heat transfer to the fascia. Due to a lack of concentrated convective heat transfer, θ_{FM}, a value of 0.21, is lower than the previous case at an R value of 0.39.

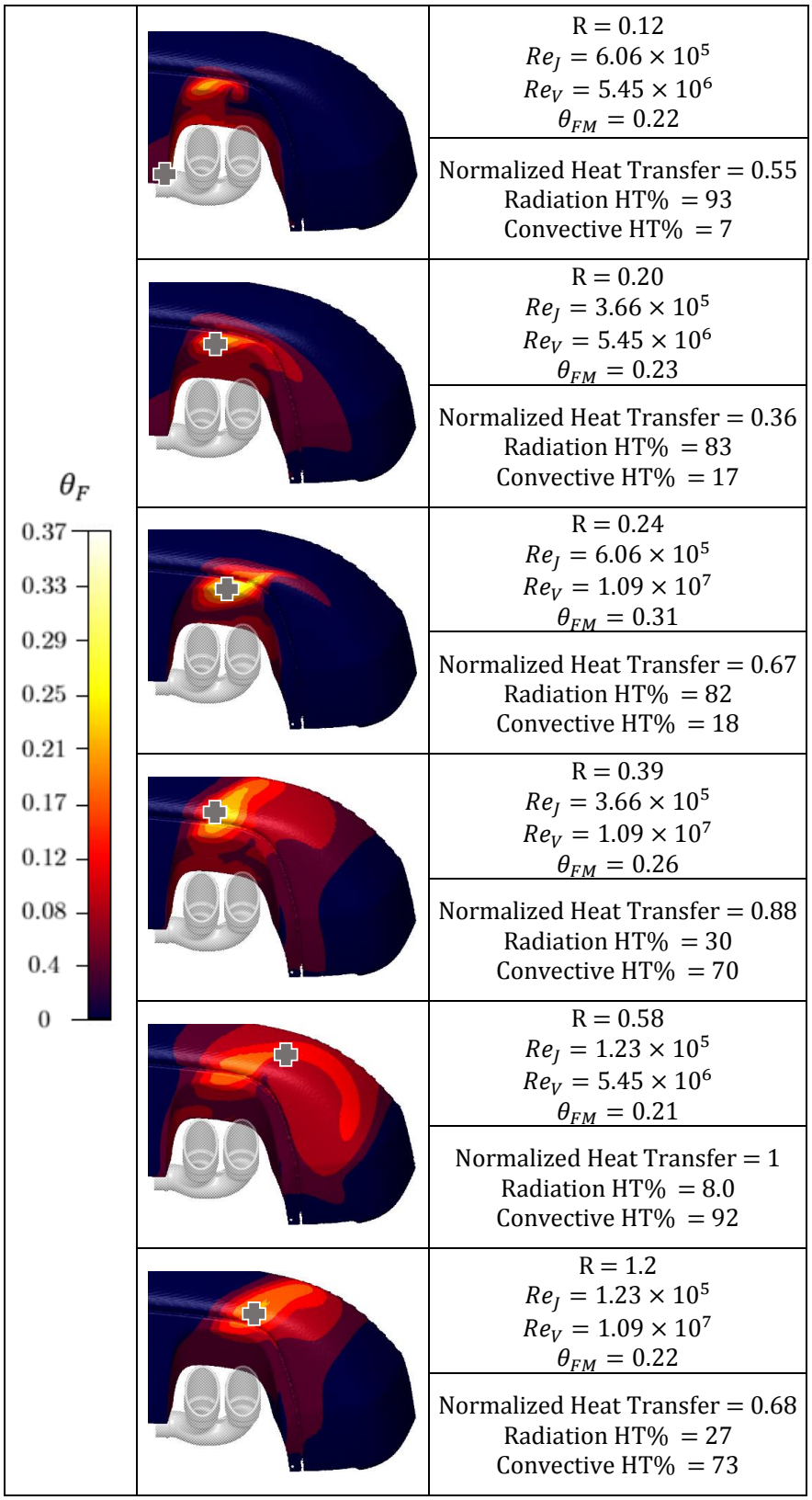

Figure 4-36: Heat transfer and θ_F values for non-zero R values, increasing R.

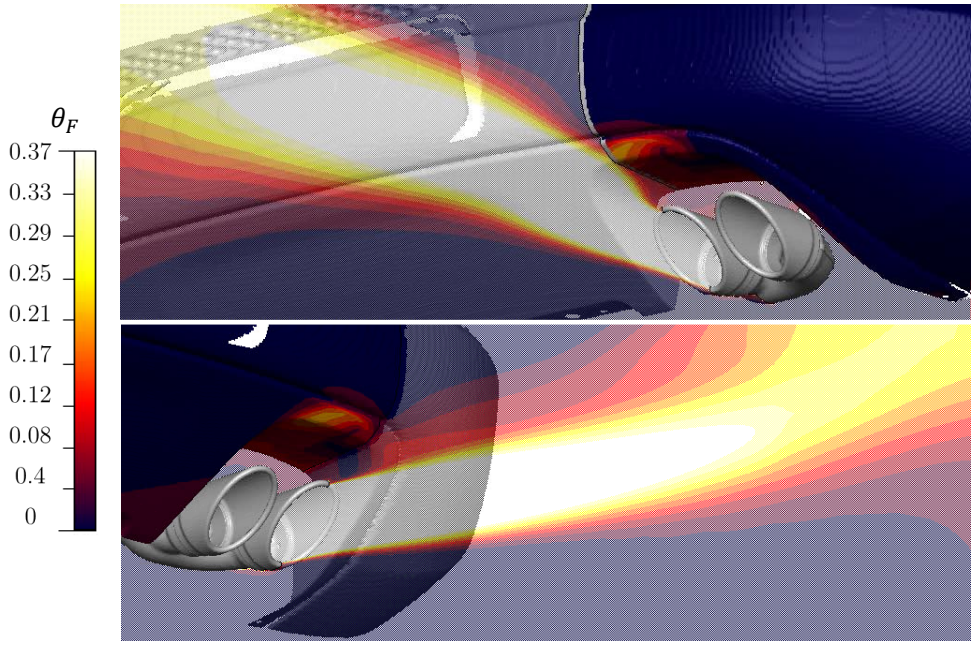

Figure 4-37: Exhaust jet and fascia θ_F contours for $R = 0.12$. Top: view towards inboard exhaust tip, plane cut at centre of inboard exhaust tip; bottom: view towards outboard exhaust tip, plane cut at centre of outboard exhaust tip.

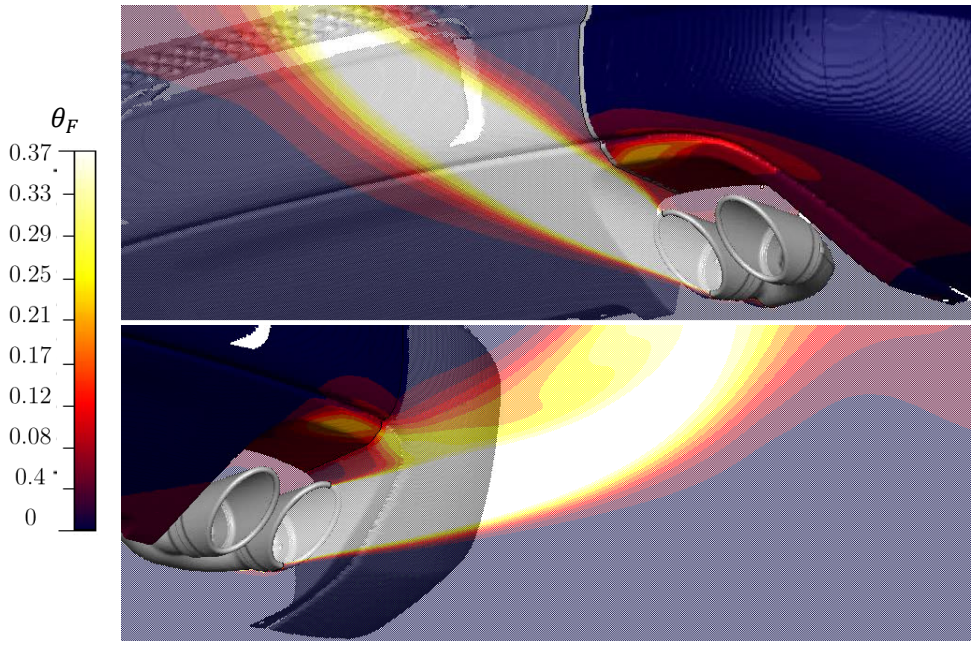

Figure 4-38: Exhaust jet and fascia θ_F contours for $R = 0.20$. Top: view towards inboard exhaust tip, plane cut at centre of inboard exhaust tip; bottom: view towards outboard exhaust tip, plane cut at centre of outboard exhaust tip.

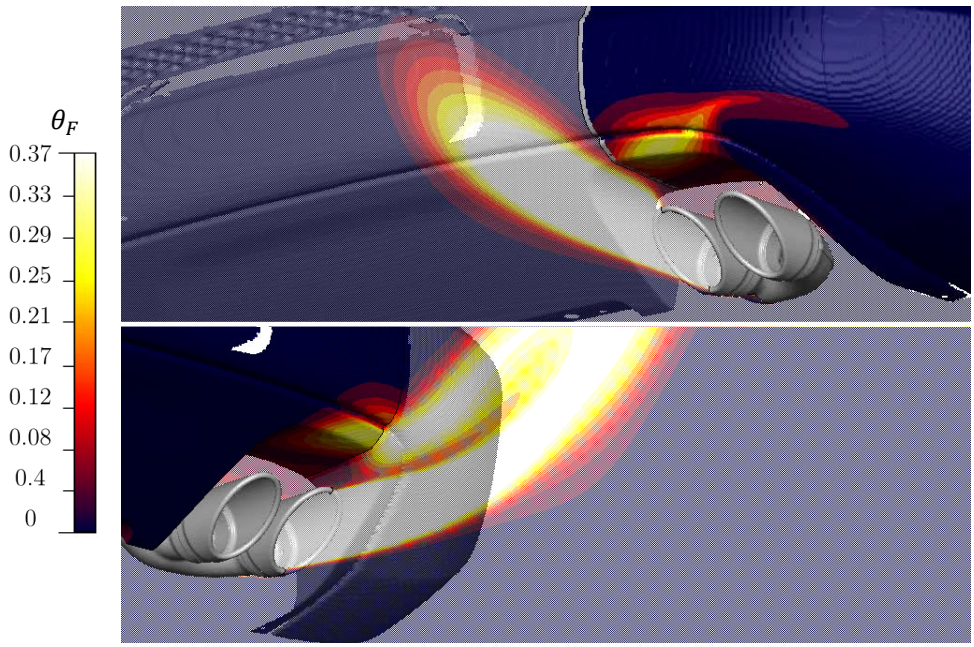

Figure 4-39: Exhaust jet and fascia θ_F contours for $R = 0.24$. Top: view towards inboard exhaust tip, plane cut at centre of inboard exhaust tip; bottom: view towards outboard exhaust tip, plane cut at centre of outboard exhaust tip.

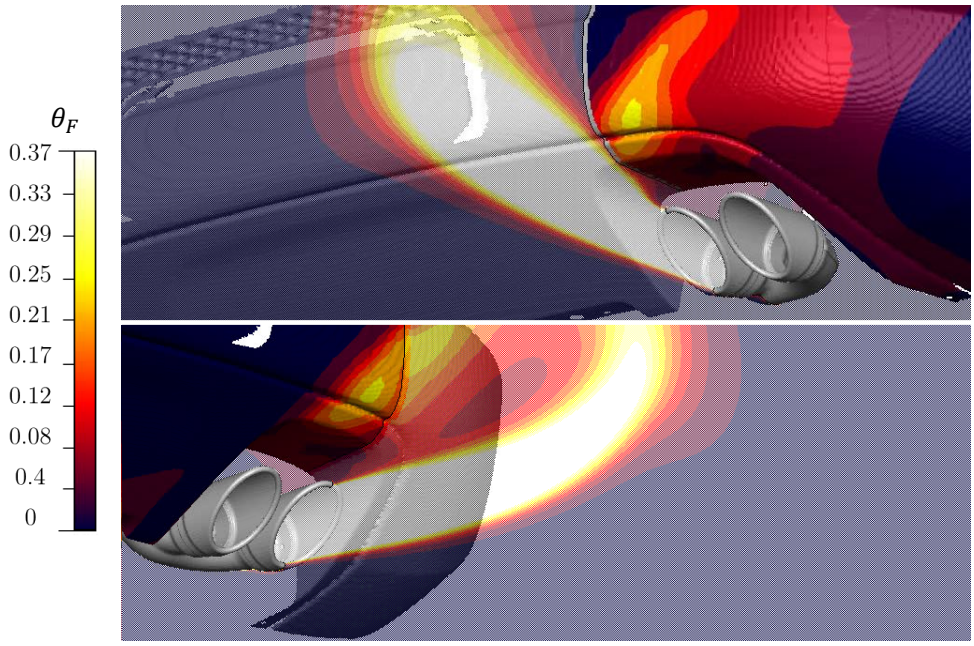

Figure 4-40: Exhaust jet and fascia θ_F contours for $R = 0.39$. Top: view towards inboard exhaust tip, plane cut at centre of inboard exhaust tip; bottom: view towards outboard exhaust tip, plane cut at centre of outboard exhaust tip.

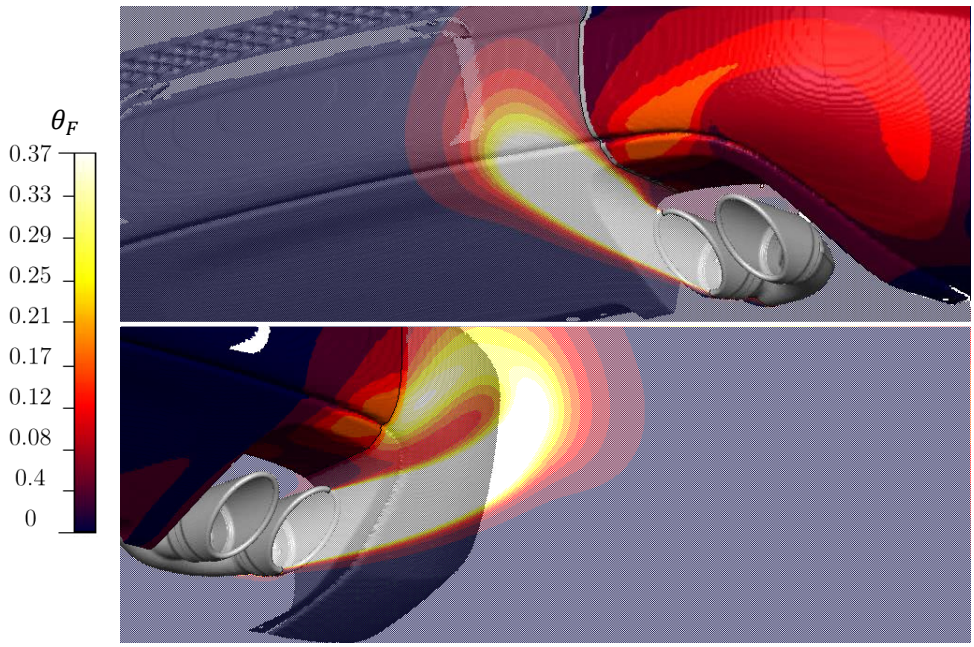

Figure 4-41: Exhaust jet and fascia θ_F contours for $R = 0.58$. Top: view towards inboard exhaust tip, plane cut at centre of inboard exhaust tip; bottom: view towards outboard exhaust tip, plane cut at centre of outboard exhaust tip.

At an R value of 1.2, the velocity of the vehicle is higher than that of the exhaust gas inlet, and in theory, the exhaust behaves as a wake rather than as jets. However, in Figure 4-42, it can be seen that local to the outboard exhaust tip (bottom), that the under-body velocity is lower than the highest velocity flow out of the outboard tip. Measuring the velocity for Re_V at a location under the exhaust tips, rather than using the vehicle speed, may result in a more accurate representation of Re_V and the velocity ratio. This is most relevant for this case, where the velocity ratio is assumed to be above 1, although the under-body flow velocity in some locations is lower than the exhaust jet inlet velocity. The impact on Re_V is minimal as large wake changes aren't expected in the turbulent regime. This is discussed further in Section 5.3.2.

In Figure 4-43, the non-uniformity of the exhaust jets exiting the exhaust tips is apparent. The size of the inboard exhaust jet is less than previous cases and less overall dispersion of the jet occurs. As a result, the convective heat transfer fraction slightly decreases to 73%. Due to the weak jet exiting the inboard exhaust tip having

little dispersion, it does not effect the outboard jet. The exhaust jet exiting the outboard tip is immediately directed into the fascia. In comparison to the case at an R value of 0.58, there is a small increase in θ_{FM}, to 0.22, due to more concentrated jet interaction with the fascia.

In summary, referring back to Figure 4-30, θ_{FM} varies in what resembles a quadratic trend with Re_V, resulting in maximum θ_{FM} values at $Re_V = 0$. Decreasing θ_{FM} values are observed as Re_V is increased, until a minimum is reached and then θ_{FM} increases as Re_V increases. Re_J's influence on θ_{FM} values is dependent on Re_V and thus the ratio of exhaust velocity and vehicle speed is best used for analysis.

For $R = 0$, a higher Re_J value will result in higher θ_{FM} values. Between 0 and 0.12 the exhaust jets are much stronger than the under-body flow and little interaction between the jets and fascia occurs, and such, the result is a θ_{FM} value dominated by radiation heat transfer. For values of the velocity ratio between 0.12 and 0.24, there are concentrated areas of convective heat transfer due to the strong exhaust jets, but with low θ_{FM} values due to cooling from the under-body flow and the lesser ability of the under-body flow to direct the jets into the fascia. At $R = 0.24$, under-body flow directs the coherent exhaust jets into the fascia and highest θ_{FM} values are observed. For $R > 0.24$, with increasing under-body flow strength, there is more dispersion of the exhaust jets and there are large areas of convective heat transfer, with decreased heat flux, decreasing θ_{FM}. At $R = 1.2$, when the exhaust inlet velocity is less than the vehicle speed, there exists a slightly higher θ_{FM} value than the case at 0.58 due to minimal interaction of the inboard exhaust jet with the outboard exhaust jet, resulting in lesser dispersion of the outboard jet and the outboard exhaust jet is directed into the fascia.

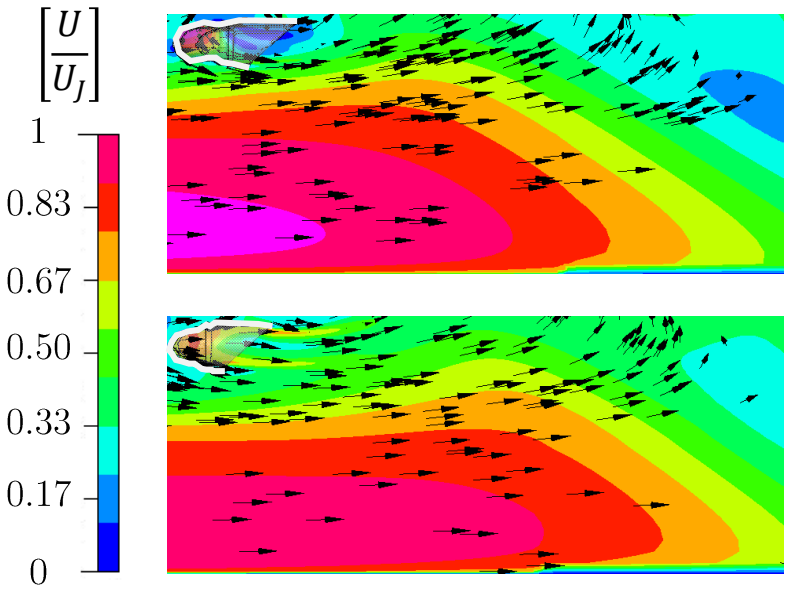

Figure 4-42: Exhaust jet and fascia velocity contours for $R = 1.2$. Exhaust outlined in white. View towards inboard exhaust tip. Top: velocity plane cut at centre of inboard exhaust tip; bottom: plane cut at centre of outboard exhaust tip.

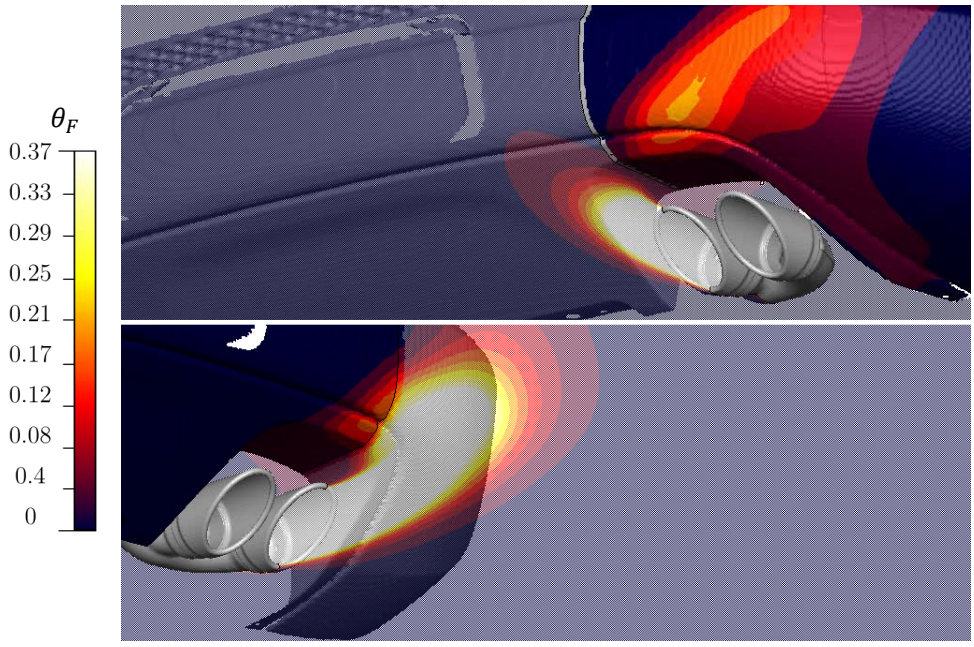

Figure 4-43: Exhaust jet and fascia θ_F contours for $R = 1.2$. Top: view towards inboard exhaust tip, plane cut at centre of inboard exhaust tip; bottom: view towards outboard exhaust tip, plane cut at centre of outboard exhaust tip.

4.3.4 Final Surrogate Model Predictions (SM_2)

4.3.4.1 Non-Geometric

Using the SM_2, the vehicle operating condition that results in the highest maximum fascia temperature is predicted. In Table 4.7, the non-geometric parameters are shown. The resulting values are the highest ETR and Re_J at the lowest Re_V value. This coincides with the analysis completed in Section 4.3.3.

Table 4.7: Non-geometric parameters predicted by SM_2 to yield highest maximum fascia temperature.

ETR[4]	Re_V	Re_J	R	$\hat{\theta}_{FM}$	θ_{FM}
253	0	4.28×10^5	0	0.23	0.29

At the baseline geometry, the non-dimensional maximum fascia value predicted by SM_2 ($\hat{\theta}_{FM}$) is 0.23. Full vehicle CFD yields $\theta_{FM} = 0.29$ at this vehicle operating condition and its θ_F contours are shown in Figure 4-44. With $R = 0$, θ_{FM} occurs at the inboard corner of the fascia, dominated by radiation heat transfer. In comparison with the current vehicle thermal management case used to benchmark exhaust designs, the resulting increase in maximum fascia temperature is 16%. Thus, the case predicted by SM_2 to have the highest maximum fascia temperature is best used as a worst case analysis with respect to the thermal protection of the rear fascia.

4.3.4.2 Geometric

SM_2 predicts a set of geometric parameters that will result in lowest fascia temperatures. In Table 4.8, the resulting values coincide with the analysis completed in Section 4.3.2, with exception of the X_+ value. SM_2's predicted optimal X_+ value is 1, whereas it was found that individually, minimizing X_+ was best (decreased jet interaction). When the other geometric parameters are maximized, maximizing the X_+ value results in a decreased exhaust surface area and due to the other maximized

parameters, the exhaust jets will be directed away from the fascia, and thus both convective and radiative heat transfer are minimized.

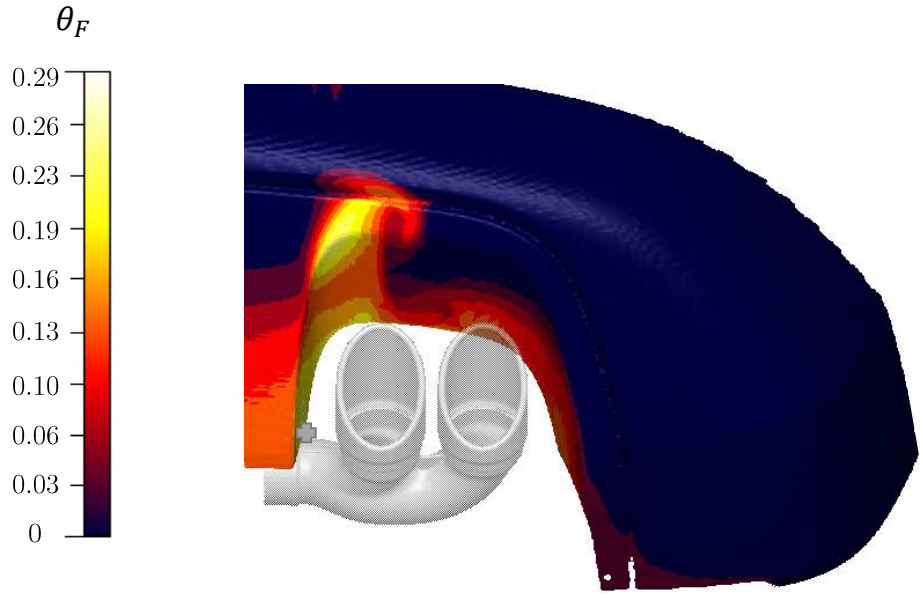

Figure 4-44: θ_F contours for predicted highest θ_{FM} case, baseline geometry.

Table 4.8: Exhaust position predicted by SM_2 to produce lowest maximum fascia temperatures.

X_+	Y_+	Z_+	β_+	$\hat{\theta}_{FM}$	θ_{FM}
1	1	1	1	0.12	0.15

At the optimized geometry, at the worst operating vehicle condition (Table 4.7), the value predicted by SM_2 ($\hat{\theta}_{FM}$) is 0.12. The resulting CFD simulation, with a θ_{FM} value of 0.15 is shown in Figure 4-45.

Due to the decrease in surface area and decrease in view factor, in comparison to the baseline geometry in Figure 4-44, radiation heat transfer to the fascia is decreased by 23%, resulting in a decrease in θ_{FM} by 0.14 (130 K). Over the surface of the fascia, it can be seen that the heat transfer from the exhaust jet is greatly reduced, and convective heat transfer to the fascia is decreased by 58%. In comparison to the baseline

positioning, where the maximum fascia temperature exceeds the maximum allowable value by 200 K, the optimized geometry only exceeds the maximum allowable value by 70 K.

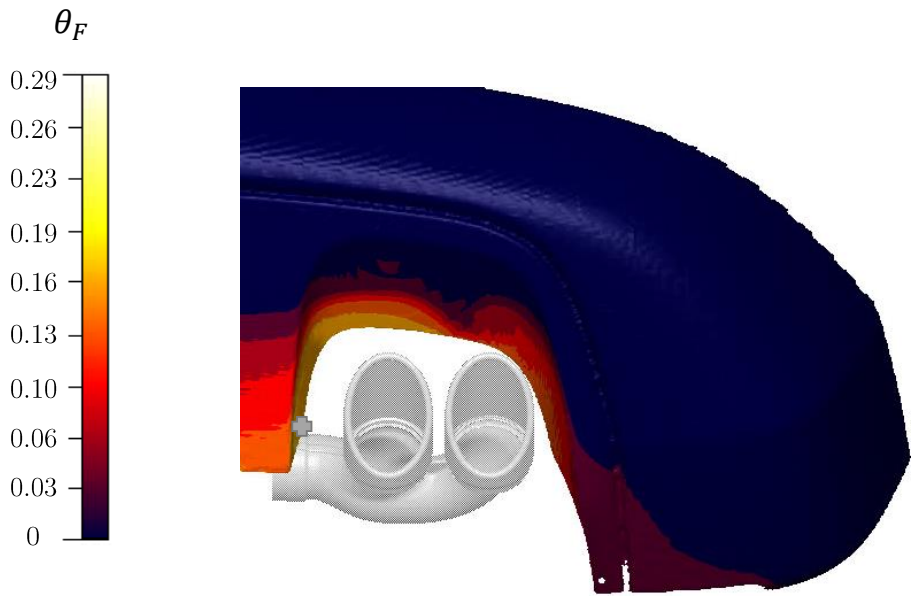

Figure 4-45: θ_F contours for predicted highest θ_{FM} case, optimized geometry.

Chapter 5

Summary, Conclusions, and Recommendations for Future Work

5.1 Summary

A parametric study was completed and the function defining the maximum fascia temperature was broken down into seven input parameters. The surrogate models along with the cases analyzed identify each parameter's individual effect on the maximum fascia temperature.

At a minimum X_+ value, a high amount of radiative heat transfer occurs due to the large surface area of the exhaust. Increasing X_+ decreases the surface area of the exhaust, and thus decreases radiation heat transfer to the fascia. Consequently, convective heat transfer is increased, resulting in a change of maximum fascia temperature location to a convection dominated location. Increasing X_+ increases concentrated convective heat transfer to the fascia and will in general increase maximum fascia temperature.

Increasing Y_+ slightly increases radiation heat transfer but also decreases the convective heat transfer from the exhaust jets to the fascia. Maximum fascia temperature

occurs at the same location regardless of Y_+ value, thus, increasing Y_+ decreases the concentrated convective heat transfer to the location of maximum fascia temperature, reducing it.

Increasing Z_+ decreases both radiation and convective heat transfer to the fascia, resulting in a net decrease of heat transfer to the fascia. Increasing Z_+ decreases maximum fascia temperature values.

Increasing β_+ decreases maximum fascia temperature, decreasing convective heat transfer, until a local minimum is reached, and then increases maximum fascia temperature to a maximum, due to the exhaust jets being directed into the fascia from under-body flow. With increasing β_+, the maximum fascia temperature will then decrease to its lowest value at the largest β_+ value studied. Without the interaction of under-body flow, SM_2 predicts that the maximum fascia temperature would decrease as β_+ increases due to decreased convective heat transfer, with the lowest maximum fascia temperature occurring at the highest β_+ value.

As exhaust temperature is increased, both radiation and convective heat transfer are increased due to the increase in temperature difference between the exhaust jets, parts, and fascia. As exhaust temperature increases, maximum fascia temperature increases.

The general trend of vehicle speed on maximum fascia temperature resembles that of a concave up parabola. At a vehicle speed of zero, the highest maximum fascia temperatures are found. As vehicle speed increases, maximum fascia temperature decreases to a local minimum, and then increases as vehicle speed increases. Over the speed range studied, the highest vehicle speed always yields lower maximum fascia temperatures than at a vehicle speed of zero.

The exhaust velocity is best analyzed with respect to the vehicle speed. The interaction with the under-body flow depends on the strength of the exhaust jets with respect to the under-body flow. Strong exhaust jets will either flow freely without

any interaction from the under-body flow, and not increase maximum fascia temperature, or it will be directed from the under-body flow towards the fascia, increasing maximum fascia temperature. Weak exhaust jets will be dispersed towards the fascia and without any areas of concentrated convection, the maximum fascia temperature will be lower.

5.2 Conclusions

As shown in the surrogate model's predictions at the optimized and baseline positioning for the worst case vehicle operating condition in Section 4.3.4, SM_2 is not perfect. The EBF model was found to typically under-predict large variations in the output, which was also shown with SM_1 for the geometric parameters. Qualitatively, it is correct; however, once a general design is in place and SM_2 determines that it is acceptable in comparison to others, a CFD simulation should be completed to confirm the surrogate model's predicted results.

When positioning the exhaust within the rear fascia, consideration must be given to the heat transfer mechanisms that will be increased or decreased depending on the exhaust's location. Positioning the exhaust in such a way to minimize convective heat transfer can increase radiative heat transfer, and may result in a maximum fascia temperature location dominated by radiation. The opposite is true as well and as such, one must carefully take into consideration the sum of the individual effects of each change in exhaust positioning. The same goes for the vehicle operating condition. The ratio of the exhaust inlet velocity to the vehicle speed determines the under-body flow and its interaction with the exhaust jets, which is shown to direct or disperse the exhaust jets depending on their strength. At a value of 0.24, highest maximum fascia temperatures were found due to the strength of the under-body flow directing the coherent exhaust jets into the rear fascia. The value of the ratio that

the maximum fascia temperature occurs at may differ for different exhaust designs; however, when designing an exhaust system, the balance between the under-body flow and exhaust jets must be understood to minimize both radiative and convective heat transfer. Thus, for both the vehicle operating condition and exhaust positioning, a balance of heat transfer mechanisms is necessary to minimize the possibility of one mechanism dominating the other. A surrogate model considers a change in multiple inputs and their total impact on the maximum fascia temperature.

Highest fascia temperatures were predicted by the surrogate model to occur at low speed and high load. In reality, a vehicle will very rarely sit stationary at wide open throttle for the amount time required to reach steady-state, (as done in the CFD simulations). This is why even with the optimized geometry, the maximum fascia temperature is still over the maximum allowable value. For a more realistic maximum fascia value at this operating condition, transient simulations could be completed as well, and it is expected that they will result in lower, but more realistic fascia temperatures as the exhaust components temperatures will be at lower, non steady-state values. This case that yields the highest fascia temperatures can still be used to benchmark different exhaust designs as it gives the absolute maximum fascia temperature that will occur.

Lastly, the geometric parameters have a large impact at the design stage. For example, a small change in X_+ from 0.9 to 1 results in a large increase in maximum fascia temperature. It is important to carefully consider the positioning of the exhaust within the fascia. Small changes in positioning matter.

5.2.1 Contributions

Although noted by literature to do a good job of sampling the design space, when using OLHS with outputs that are sensitive to small changes in inputs, (as noted with the geometric parameters impact on the maximum fascia temperature), sampling the

bounds of the inputs is important, otherwise the model will not capture large changes at the extreme values of each input. Thus, it is recommended is to complete a DOE with OLHS sampling and then check the error of the model with experiments sampled at the edges of the design space. If there is a large amount of error, experiments should be added at the minimum and maximum value of each input to capture the large changes at the extremes of each input variable.

The case that yields the highest fascia temperature (worst case) occurs at low vehicle speeds with the highest exhaust gas temperature and the highest exhaust gas velocity appropriate for that gas temperature. With this knowledge, the current experimental tests can be improved. The test engineer can now complete the experiment at the absolute worst case vehicle operating condition. The engineer can also confidently place thermocouples on the fascia to capture the maximum fascia temperature, as it was shown that the maximum fascia temperature will occur at the inboard corner of the fascia, since hotspot is likely to be radiation dominated. For other vehicle operating conditions and varying exhaust positions, the knowledge of the velocity ratio and the impact of the exhaust positioning can be used to place thermocouples in either the radiation dominated or convection dominated locations.

Based on this thesis, FCA can now assess worst case conditions at design times. Even though the surrogate model's predicted temperature may not be in perfect agreement CFD or experimental values, the qualitative results will be correct. For example, in the comparison of two configurations, the configuration predicted to have the lowest maximum fascia temperature will be correct, reducing design time.

5.3 Future Work

5.3.1 Location Analysis

An investigation can be made to see if the model could predict the hotspot location. The coordinates of all the hotspots for each case in the DOE would need to be recorded and used as a second output. To properly predict the location of the hotspot, the surrogate model should be forced to make its prediction on the surface of the fascia. In other words, since the model does not "know" that the fascia is a surface existing in three-dimensional space, the predictions should be constrained to the surface. This improved surrogate model can be used to analyze hotspot locations and better place thermocouples for experimental tests.

Using the simulation domain without a trailer, the cases used to complete this DOE could be run. The maximum fascia temperature values and their locations could be added as a third output. This would allow the model to predict the maximum fascia temperature as well as its location with and without a trailer as an output. By completing some experimental tests, the mapping from experimental tests to CFD simulations without a trailer can be determined and then compared with the CFD simulations with a trailer. This would help show the impact the trailer has on the location of maximum fascia temperatures and fully connect the maximum fascia temperatures and its locations from the experimental data to the CFD simulations with and without a trailer.

5.3.2 Exhaust Geometry

The exhaust tip diameter and the spacing of the exhaust tips remained constant throughout the thesis. By adding the diameter of the exhaust tips to the DOE, the inboard and outboard exhaust jet velocities could be varied. Smaller exhaust tip diameters will increase the velocity of the exhaust jets, potentially decreasing convec-

tive heat transfer. The spacing between the two exhaust tips could be added as well and will determine the interaction between the inboard and outboard exhaust jets. The greater the distance between the two, the more they will act as two separate jets and this will have an impact on maximum fascia temperatures. If the jets act separately, but have low strength, they will both easily be dispersed over the fascia surface, decreasing concentrated convective heat transfer. Increasing the space between the two exhaust tips will move them closer to the edges of the fascia, increasing the view factor, increasing radiation heat transfer. The combination of modifying the exhaust tip diameter, spacing of the exhaust tips and the positioning of the exhaust tips has potential to decrease fascia temperatures even greater than what was found in this thesis.

5.3.3 Velocity Measurements for Reynolds Number Calculations

For the case in Section 4.3.3.4 with an R value of 1.2, the velocity contours are revisited in Figure 5-1. At its maximum, the under-body velocity is larger than the exhaust jet inlet. However, just below the exhaust tips, the under-body velocity is lower than both the exhaust jet at its inlet, as well as the outboard exhaust jet. This brings attention to the measurement of exhaust velocity. Due to the 90 degree bend in the tailpipe, the velocities of the exhaust jets exiting the exhaust tips are unequal and not equivalent to their prescribed boundary condition at their inlet. Averaging the exhaust velocity at the exhaust tips, or analyzing the velocity of each individual exhaust jet will result in a more accurate representation of Reynolds number and velocity ratio.

Although the under-body velocity is lower than the vehicle speed, Re_V values still remain turbulent and the velocity measurement of the external flow is not a significant issue. For a more accurate representation of Re_V as well as R, the velocity

measurement of the external flow could be measured in at a location slightly below the exhaust tips, or by averaging the velocity in the area below the exhaust tips.

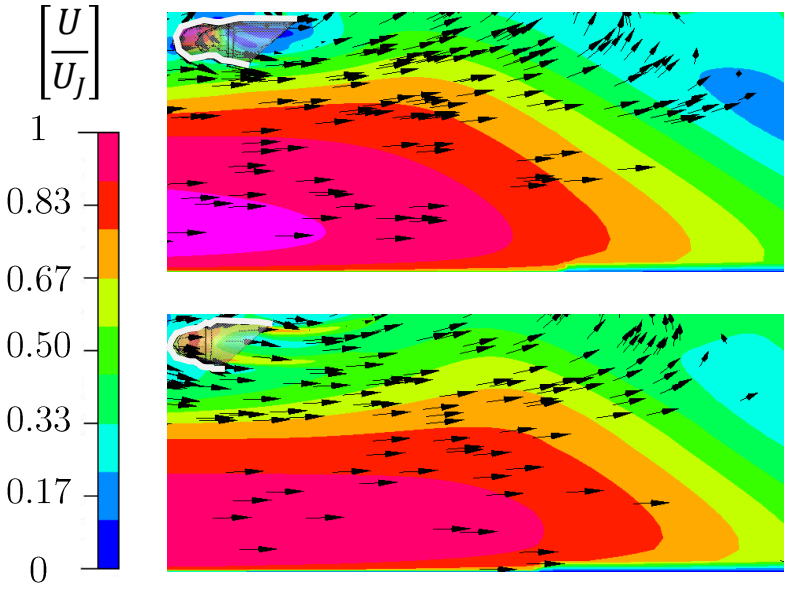

Figure 5-1: Exhaust jet and fascia velocity contours for $R = 1.2$. Exhaust outlined in white. View towards inboard exhaust tip. Top: velocity plane cut at centre of inboard exhaust tip; bottom: plane cut at centre of outboard exhaust tip.

5.3.4 Improvements to CFD Modelling

By modelling conduction in the fascia, more accurate heat transfer through the fascia will be captured and provide more reliable CFD results. The use of varying parameters will also better capture the convective heat transfer between the exhaust jets and rear fascia. Modelling the exhaust flow through exhaust system would be ideal; however, there are many mechanisms to consider:

1. convection heat transfer from the exhaust gas to the walls of the exhaust system,
2. conduction heat transfer through the exhaust parts, and
3. heat generation by the exothermic reaction in the catalytic converter and flow through the catalytic converter.

Modelling the convective heat transfer from the exhaust gas to the walls of the system and then the conduction through the exhaust parts captures the exhaust part temperatures as well as the temperature drop in the exhaust gas. Simulating the catalytic converter would be difficult due to the monolith and the exothermic reaction occurring inside. By using a one-dimensional model of the exhaust system, the exhaust temperature and flow rate could be captured at the exit of the catalytic converter, where a CFD boundary condition could be implemented. The flow through the exhaust parts could then be modelled, and thus the exhaust jets exiting the exhaust tips would be more accurately represented. Work could be completed to experimentally validate the CFD simulations, defining the methodology to properly model exhaust flow in and exiting of the system. Lastly, transient simulations could be completed to acquire maximum fascia temperatures that will occur during an average drive-cycle and the time could become a new input parameter as well.

Bibliography

[1] Srinivasan, K., Woronowycz, G., Zabat, M., Widdecke, N., and Tripp, J. An Efficient Procedure for Vehicle Thermal Protection Development. *SAE Technical Paper*, 2005-01-1904, 2005.

[2] Eller, J., Binner, T., Reister, H., Widdecke, N., and Wiedemann, J. Challenges and Opportunities of Numerically Simulating the Idle Load Case for Vehicle Thermal Management. *SAE Technical Paper*, 2015-01-0340, 2015.

[3] Xiao, G., Yang, Z., Wang, D. and Zhang, W. Investigation of Radiation and Conjugate Heat Transfers for Vehicle Underbody. *SAE Technical Paper*, 2008-01-1819, 2008.

[4] Spring, S., Weigand, B., Krebs, W., and Hase, M. CFD Heat Transfer Predictions of a Single Circular Jet Impinging with Crossflow. *Presented at 9th AIAA/ASME Joint Thermophysics and Heat Transfer Conference*, AIAA Paper 2006-3589, 2006.

[5] Queipo, N., Haftka, R., Shyy, W., Goel, T., Vaidyanathan, R., and Tucker, K. Surrogate-Based Analysis and Optimization. *Progress in Aerospace Sciences*, Vol. 41(1), 1-28, 2005.

[6] Jendoubi, S. and Strykowski, P. Absolute and Convective Instability of Axisymmetric Jets With External Flow. *Physics of Fluids*, Vol. 6, 3000-3009, 1994.

[7] Michalke, A. On the Influence of a Wake on the Inviscid Instability of a Circular Jet With External Flow. *Physics of Fluids*, Vol. 10, 637-644, 1993.

[8] Chan, C.H.C. and Lam, K.M. Centerline Velocity Decay of a Circular Jet in a Counterflowing Stream. *Physics of Fluids*, Vol. 10, 637-644, 1998.

[9] Zhang, X. and Romzek, M. Computational Fluid Dynamics (CFD) Applications in Vehicle Exhaust System. *SAE Technical Paper*, 2008-01-0612, 2008.

[10] Kandylas, I.P. and Stamatelos, A.M. Engine Exhaust System Design Based on Heat Transfer Computation. *Journal of Energy Conversion and Management*, Vol. 40(10), 1057-1072, 1999.

[11] Modest, M. *Radiative Heat Transfer.* 3rd edition, 2013.

[12] Forrester, A., Sobester, A., and Keane, A. *Engineering Design Via Surrogate Modelling: A Practical Guide.* 1st edition, 2008.

[13] Mckay, D., Beckman, R., and Conover, W. A Comparison of Three Methods for Selecting Vales of Input Variables in the Analysis of Output From a Computer Code. *Technometrics*, Vol. 21, 239-245, 1999.

[14] Srivastava, A., Hacker, K., Lewis, K., and Simpson, T. Development of a Kriging Based Surrogate Approximation Method for Large Scale Systems. *2000.*

[15] Simpson, T., Peplinski, J., Koch, P., and Allen, J. On the Use of Statistics in Design and the Implications for Deterministic Computer Experiments. *in Design Theory and Methodology*, DTMC 97, 1997.

[16] Koziel, Y., and Yang, X. *Computational Optimization, Methods and Algorithm.* 1st edition, 2011.

[17] Dassault Systemes, Velizy-Villacoublay, France. *Isight User Manual*, 2015 edition, 2015.

[18] Jin, R.C., Chen, W., and Sudjianto, A. An Efficient Algorithm for Constructing Optimal Design of Computer Experiments. *Journal of Statistical Planning and Inference*, Vol. 134, 268-287, 2005.

[19] Johnson, M.E., Moore, L.M., and Ylvisaker, D. Minimax and Maximin Distance Designs. *Journal of Statistical Planning and Inference*, Vol. 26(2), 131-148, 1990.

[20] Morris, M. and Mitchell, T. Exploratory Designs for Computational Experiments. *Journal of Statistical Planning and Inference*, Vol. 43(3), 381-402, 1995.

[21] Mak, M.W. and Li, C.K. Elliptical Basis Function Networks and Radial Basis Function Networks for Speak Verification: A Comparative Study. *IJCNN'99. International Joint Conference on Neural Networks. Proceedings*, Vol. 5, 3034-3039, 1999.

[22] ESI Group, Paris, France. *CFD Ace User Manual*, 2015 edition, 2015.

[23] Fluent Inc., Canonsburg, PA. *Fluent 6.3 User Guidel*, 2006 edition, 2006.

[24] Mikron Instrument Company. *Table of Emissivity of Various Surfaces For Infrared Thermometers.*

[25] Gamma Technologies. GT-power.

Appendix A

DOE Samples

Case	X_+	Y_+	Z_+	β_+	ETR^4	Re_V	Re_J	R
1	0.39	0.09	0.72	0	45.82	4.06×10^6	1.96×10^5	0.27
2	0.04	0.04	0.94	0.67	69.83	3.58×10^6	3.13×10^5	0.15
3	0.72	0.65	0.02	0.89	143.73	1.67×10^6	5.71×10^5	0.04
4	0.78	0.15	0.07	0.52	58.92	1.05×10^7	3.64×10^5	0.38
5	0.91	0.52	0.54	0.09	20.25	2.86×10^6	4.35×10^4	0.87
6	0.54	0.44	0.76	0.87	13.55	9.54×10^5	5.75×10^4	0.22
7	0.93	0.72	0.65	0.74	178.76	1.91×10^6	2.81×10^5	0.09
8	0.48	0.24	0.61	0.04	49.90	1.10×10^7	1.28×10^5	1.12
9	1	0.91	0.13	0.37	110.85	7.40×10^6	3.98×10^5	0.24
10	0.85	0.89	0.74	0.85	104.85	5.97×10^6	6.48×10^5	0.12
11	0.8	0.39	1	0.41	72.73	1.19×10^6	4.52×10^5	0.03
12	0.2	0.26	0.5	0.8	28.78	1.00×10^7	1.01×10^5	1.30
13	0.13	0.07	0.11	0.61	175.59	6.45×10^6	5.33×10^5	0.16
14	0.54	0.74	0.26	0.07	206.06	4.79×10^5	5.19×10^5	0.01
15	0.24	0.85	0.89	0.44	100.97	7.16×10^5	2.26×10^5	0.04
16	0.37	0.41	0.98	0.65	101.01	1.03×10^7	5.10×10^5	0.26
17	0.26	0.83	0.8	0.11	88.11	4.30×10^6	6.64×10^5	0.09
18	0.74	0.8	0.87	0.15	212.11	7.64×10^6	4.33×10^5	0.23
19	0.22	1	0.59	0.33	56.16	1.07×10^7	2.83×10^5	0.50
20	0.02	0.94	0.15	0.59	149.42	4.54×10^6	5.61×10^5	0.11
21	0.5	0.67	0.3	0.96	203.00	9.79×10^6	4.64×10^5	0.28
22	0.17	0.46	0.41	1	106.94	2.15×10^6	1.70×10^5	0.17
23	0.7	0.02	0.33	0.54	131.07	0	3.22×10^5	0.00
24	0.61	0.87	0.91	0.83	40.00	8.12×10^6	8.71×10^4	1.23

Table A.1: DOE Cases (At CFD boundary inlet).

Appendix B

Calculations

B.0.1 Mach Number Calculation

$$M_{max} = \frac{v_{max}}{c_{max}}$$

$$c_{max} = (k_{air} * R * T_{Max})^{0.5} = (1.336 \star 287.05 * 1241)^{0.5} = 689.87 \, \frac{\mathrm{m}}{\mathrm{s}}$$

$$v_{max} = 127 \, \frac{\mathrm{m}}{s}$$

$$M_{max} = \frac{127}{689.87} = 0.1841$$

B.0.2 Reynolds Number Calculation - Constant Properties - 311 K, U_J=83.68

$$\rho = 1.12 \, \mathrm{kg/m^3}, \mu = 1.91 \times 10^{-5} \, \mathrm{kg/m \cdot s},$$

$$Re_J = \frac{\rho U_J D_{Exh}}{\mu} = \frac{(1.12)(83.68)(0.0578)}{1.91 \times 10^{-5}} = 2.84 \times 10^5$$

B.0.3 Reynolds Number Calculation - Variable Properties - 1242 K, U_J=83.68

$$\rho = 0.028\,\mathrm{kg/m^3}, \mu = 4.98 \times 10^{-5}\,\mathrm{kg/m \cdot s},$$

$$Re_J = \frac{\rho U_J D_{Exh}}{\mu} = \frac{(0.028)(83.68)(0.0578)}{4.98 \times 10^{-5}} = 2.72 \times 10^4$$

$$\%\,\mathrm{Change\,in\,Re} = \left[\frac{2.84 \times 10^5 - 2.72 \times 10^4}{2.84 \times 10^5}\right] \times 100\% = -90.41\%$$

Appendix C

EBF Model Matrices

C.0.1 Initial Model - SM_1- Inputs: 7, Outputs: 1, Designs: 24

$$\begin{bmatrix} x1 \\ x2 \\ x3 \\ x4 \\ x5 \\ x6 \\ x7 \end{bmatrix} = \begin{bmatrix} Z_+ \\ Exhaust\,Temperature \\ Exhaust\,Velocity \\ Vehicle\,Speed \\ Y_+ \\ X_+ \\ \beta_+ \end{bmatrix}$$

$$y1 \;=\; Maximum\,Fascia\,Temperature$$

Model shape parameter: 1

Model imax parameter: 24

Model Scaling Array:

$$\begin{bmatrix} 0.02 & 590.00 & 121.25 & 28.22 & 0.02 & 0.16 & 10 & 233.62 \\ 0.01 & 596.59 & 8.50 & 0 & 0.02 & 0.03 & 0 & 342.48 \\ 0.03 & 1186.59 & 129.75 & 28.22 & 0.04 & 0.18 & 10 & 576.1 \end{bmatrix}$$

Covariance Matrix:

$$\begin{bmatrix} 6.53 & 0 & & \cdots & \cdots & & 0 \\ 0 & 4.95 & & & & & \\ & & 4.48 & \ddots & & & \vdots \\ \vdots & & \ddots & 7.25 & \ddots & & \vdots \\ \vdots & & & \ddots & 8.17 & & \\ & & & & & 8.98 & 0 \\ 0 & & \cdots & \cdots & & 0 & 0.28 \end{bmatrix}$$

Basis Center Array:

$$\begin{bmatrix} 31.75 \\ -43.75 \\ -24.62 \\ -84.12 \\ 17.73 \\ 22.20 \\ 0.34 \\ 16.52 \\ 11.00 \\ 34.29 \\ -0.79 \\ 24.81 \\ 28.99 \\ -9.61 \\ -31.07 \\ 11.75 \\ 4.69 \\ -15.06 \\ 4.73 \\ -10.79 \\ 30.00 \\ 15.40 \\ -16.43 \\ -17.98 \\ 465.15 \end{bmatrix}$$

C.0.2 Final Model - SM_2- Inputs: 7, Outputs: 1, Designs: 43

$$\begin{bmatrix} x1 \\ x2 \\ x3 \\ x4 \\ x5 \\ x6 \\ x7 \end{bmatrix} = \begin{bmatrix} Z_+ \\ Exhaust\,Temperature \\ Exhaust\,Velocity \\ Vehicle\,Speed \\ Y_+ \\ X_+ \\ \beta_+ \end{bmatrix}$$

$$y1 \;=\; Maximum\,Fascia\,Temperature$$

Model shape parameter: 1.0

Model imax parameter: 43

Model Scaling Array:

$$\begin{bmatrix} 0.02 & 590.00 & 121.25 & 28.22 & 0.02 & 0.16 & 10 & 233.62 \\ 0.01 & 596.59 & 8.50 & 0 & 0.02 & 0.03 & 0 & 342.48 \\ 0.03 & 1186.59 & 129.75 & 28.22 & 0.04 & 0.18 & 10 & 576.1 \end{bmatrix}$$

Covariance Matrix:

$$\begin{bmatrix} 8.02 & 0 & & \cdots & \cdots & & 0 \\ 0 & 2.49 & & & & & \\ & & 1.57 & \ddots & & & \vdots \\ \vdots & & \ddots & 5.65 & \ddots & & \vdots \\ \vdots & & & \ddots & 2.25 & & \\ & & & & & 5.86 & 0 \\ 0 & & \cdots & \cdots & & 0 & 2.56 \end{bmatrix}$$

Basis Center Array:

$$\begin{bmatrix} 43.20 \\ -47.66 \\ -23.13 \\ -85.04 \\ 55.78 \\ 33.46 \\ -0.20 \\ 35.00 \\ 79.49 \\ 41.49 \\ 5.75 \\ 31.47 \\ 41.08 \\ 6.82 \\ -40.47 \\ 15.12 \\ 19.40 \\ 8.14 \\ 5.14 \\ -13.88 \\ 31.63 \\ 14.17 \\ -12.60 \\ -31.52 \\ 24.24 \\ 11.78 \\ -42.63 \\ -9.37 \\ -29.71 \\ -200.11 \\ -116.54 \\ -34.03 \\ 36.04 \\ -30.97 \\ 6.61 \\ 37.65 \\ 5.93 \\ -14.49 \\ 140.68 \\ -0.08 \\ -27.09 \\ 81.48 \\ -52.03 \\ 473.15 \end{bmatrix}$$

Vita Auctoris

Name:	Tyler Doyle
Place of Birth:	London, Ontario
Year of Birth:	1994
Education:	M.A.Sc in Mechanical Engineering University of Windsor, 2016-2018
	B.A.Sc in Mechanical Engineering University of Windsor, 2012-2016